Study of a Large Deformable Mirror Concept

Heimsten, Rikard

2011

Study of a Large Deformable Mirror Concept

Rikard Heimsten

Lund Observatory
Department of Astronomy and Theoretical Physics
Lund University
Sweden

Thesis for degree of Doctor of Philosophy

Thesis advisors:
Torben Andersen, Professor
Mette Owner-Petersen, Assoc. Professor

Faculty Opponent

Babak Sedghi
European Southern Observatory
Garching, Germany

Evaluation Committee

Hans Henrik Niemann
Department of Electrical Engineering
Technical University of Denmark

Lennart Lindegren
Department of Astronomy and Theoretical Physics
Lund University

Sven-Göran Pettersson
Department of Physics
Lund University

Cover: Influence functions of an actuator poke, with and without the local controller.

LUNFD6/(NFAS-1041)/1-134/(2011)

ISBN 978-91-7473-167-5
Printed by Media-Tryck, Lund 2011

Study of a Large Deformable Mirror Concept

Rikard Heimsten

Lund Observatory
Department of Astronomy and Theoretical Physics
Lund University
Sweden

Thesis for degree of Doctor of Philosophy

Thesis advisors:
Torben Andersen, Professor
Mette Owner-Petersen, Assoc. Professor

LUND UNIVERSITY

Faculty Opponent is Dr. Babak Sedghi who is working at European Southern Observatory. The defence will be held in the Lundmark lecture hall at the Department for Astronomy and Theroetical Physics on the 25th of October, 2011 at 10.15.

Organization	Documentname
LUND UNIVERSITY Dept. of Astronomy & Theoretical Physics Lund Observatory Box 43 SE-221 00, Lund, Sweden	DOCTORAL DISSERTATION Date of issue September 20, 2011 Sponsoring organization

Author(s)
Rikard Heimsten

Title and subtitle

Study of a Large Deformable Mirror Concept

Abstract

It is attractive to integrate a large deformable mirror for adaptive optics into an astronomical telescope rather than using relay optics within an auxiliary instrument. However, the resulting large deformable mirror can be expensive, particularly for extremely large telescopes. We have pursued a low-cost approach using force actuators connected to the back of the deformable mirror through suction cups. This innovative concept for attachment of force actuators does not require high mechanical tolerances.

Use of inexpensive voice-coil actuators and a thin mirror leads to a poorly damped system with many structural eigenfrequencies within the desired bandwidth. A feedback signal (in addition to the one from the wavefront sensor) is introduced by electro-mechanical sensors placed at the back of the deformable mirror. Using these sensors, stiffness and damping are added to the mirror through feedback loops.

We introduce a local control concept with actuator families that have predetermined force patterns. Use of actuator families reduces crosstalk between adjacent actuators and prevents excitation of a number of low-order eigenmodes. This strategy can be seen as extending Saint-Venant`s principle beyond the static case. Thus, low-order eigenmodes are only weakly excited by actuation, leading to significant cost reduction for the sensors. The suggested sensors are of the electret microphone type.

We present an integrated model of our suggested deformable mirror concept, which we use to demonstrate the controllability of the proposed first experimental laboratory setup. The experimental setup encompasses a partially illuminated large deformable mirror, where some force actuators are replaced by dummy actuators. From the experiment, key features, such as local control performance, dynamic range, controllability and robustness of the deformable mirror can be evaluated.

Key words: Large deformable mirror - Adaptive optics - Distributed Control - Local control: actuator family - Faceplate: vibration modes - Faceplate: Dimensionless modal analysis

Classification system and or index / terms (if any):

Supplementary bibliographical information:		Language English
ISSN and key title:		ISBN 978-91-7473-167-5
Recipient'snotes	Number of pages 136	Price
	Securityclassification	

Turtles all the way down

This thesis is based on the following publications:

i **Distributed Force Control of Deformable Mirrors.**

D. G. MacMynowski, **R. Heimsten**, T. Andersen
European Journal of Control, Vol. 17, 2011

ii **Suppressing Low-Order Eigenmodes with Local Control for Deformable Mirrors.**

R. Heimsten, M. Owner-Petersen, T. Ruppel, D. G. MacMynowski, T. Andersen
Accepted for publication in Optical Engineering, 2011

iii **Concept, Modeling and Performance Prediction of a Low-Cost, Large Deformable Mirror.**

R. Heimsten, D. G. MacMynowski, T. Andersen, M. Owner-Petersen
Submitted to Applied Optics, 2011

iv **Integrated Modeling of a Laboratory Setup for a Large Deformable Mirror.**

R. Heimsten, T. Andersen, M Owner-Petersen, D. G. MacMynowski
Proc. SPIE IMC11, 2011

Publications and conference proceedings not included in this thesis:

i **Modeling Large Deformable Mirrors.**

R. Heimsten, T. Andersen, M. Owner-Petersen
Proc. SPIE, Vol. 7017, 2008

ii **Progress in Developing a Low-Cost Deformable Mirror.**

R. Heimsten, D.G. MacMynowski, T. Andersen
Proc. SPIE, Vol. 7736, 2010

Contents

Chapter 1

Introduction

The improvements of the imaging quality of optical ground-based telescopes over the last three decades are strongly related to development of adaptive optics (AO) technology. Prior to the use of AO systems for telescopes, the incentive for building larger telescopes was to collect more photons. The amount of collected photons is proportional to the square of the diameter of the primary mirror, D_{PM}. However, the wavefront aberrations introduced by the atmosphere set the resolution limit independently of the size of the primary mirror. With a perfect AO system, it is possible to overcome the resolution limit imposed by the atmosphere, and the area of the diffraction spots scales as $1/D_{\mathrm{PM}}^2$. With AO, the sensitivity of a telescope therefor scales with D_{PM}^4, which is a major motivation for building even larger optical telescopes than existing today.

Adaptive optics was originally envisioned by Babcock in 1953 [1] to compensate for optical phase differences introduced by the atmosphere. An AO system includes three basic components; a wavefront sensor, a control system, and one or more corrective elements (often implemented as deformable mirrors). Limitations in computational power prevented realization of AO systems until the 1970s, when correction was achieved with RTAC (Real Time Atmospheric Compensation) [2]. Today most large optical telescopes utilize AO systems to achieve better optical performance.

Design of Extremely Large Telescopes (ELTs) today form a major research topic within the ground-based telescope field. The Telescope Group in Lund has made a significant contribution to the field, through the Euro50 concept [3]. Three ELT projects are today in their design phases; European Extremely Large Telescope[1], Giant Magellan Telescope[2],

[1] http://www.eso.org/public/teles-instr/e-elt.html
[2] http://www.gmto.org

and Thirty Meter Telescope[3]. To fully utilize the capabilities of the future ELTs, research in, and development of, AO are needed. A possible solution is to replace an existing stiff telescope mirror, for instance the secondary mirror, with a deformable mirror (DM). This approach can be exploited only if the construction cost of large DMs is reasonable.

Current large deformable mirrors generally either have piezo-electrical (position) or voice-coil (force) actuators. Most often, voice-coil actuators are superior in stroke and voltage-to-displacement power consumption. In addition, a malfunctioning voice-coil actuator does not leave an imprinted displacement pattern on the mirror, which is the case for piezo-electrical actuators. The main drawback of voice-coil actuators is the more complex control system required to manage the dynamical behavior. For construction of 911 mm deformable secondary mirrors for the AO system of the Large Binocular Telescope[4], a concept encompassing force actuators has been formulated by an Italian group based at Arcetri Astrophysical Observatory [4, 5, 6]. The concept is a further development of the DM integrated in the Multi Mirror Telescope[5] [7]. First light on the Large Binocular Telescope using a deformable secondary mirror was captured in 2010 [8]. Another concept pursued by the company CILAS in partnership (among others) with Observatoire de Paris Meudon is foreseen for the M4 adaptive unit of the European-ELT design. A laboratory prototype of the DM using piezo-electrical actuators embedded among dummy actuators was implemented in 2010 [9, 10].

1.1 Proposed Deformable Mirror Concept

In order to potentially reduce the cost of large deformable mirrors, a low-cos concept is presented here. It is based upon inexpensive force actuators and back sensors, which were conceptually designed in 2006 [11]. The actuator concept with a commercially available voice-coil and a linear variable differential transformer (LVDT) is shown in Fig. 1.1. Easy attachment to the back of the mirror is realized by an evacuated suction cup, which enables convenient manufacturing tolerances and easy exchange of malfunctioning actuators. The suction cup introduces undesirable resilience between the faceplate and the voice coil, adding a low-frequency eigenmode. To circumvent this drawback, the LVDT supplies a feedback signal for an internal position loop that controls the position of the moving rod. The material and form of the suction cup should be chosen such that the displacement of the rod is a magnitude larger than the faceplate deflection. Thus, the precision requirement for the LVDT is not as strict as for the sensors measuring faceplate deflection.

The combination of force actuators and a thin mirror results in a soft structure with many

[3] http://www.tmt.org
[4] http://www.lbto.org
[5] http://www.mmto.org

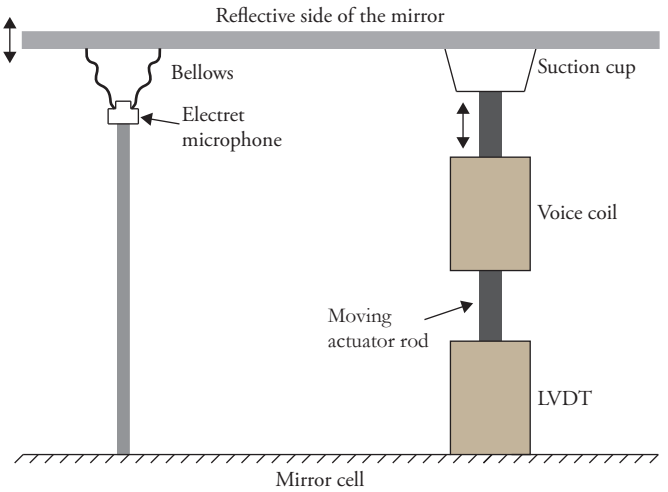

Figure 1.1: The components used for the actuators and sensors. A linear variable differential transformer is used in an internal control system to increase the bandwidth of the actuators by suppressing the influence of resilience in the suction cup. The microphone inside the bellows is a pressure sensor used in the faceplate control system to increase bandwidth.

lightly damped structural resonances and anti-resonances within the desired bandwidth of the AO system. To control the structure, additional sensors placed at the back of the mirror are used. Electret microphones can be used as pressure sensors to detect faceplate deflection, and if placed in bellows, their sensitivity is increased and they are also protected against outside acoustic noise. The pressure change is largely proportional to the displacement of the mirror, thus an electret microphone in bellows is essentially a position sensor. The concept is shown in Fig. 1.1. Inclusion of the sensors in the actuator would effectively make the force actuators appear as position actuators. However, it is mechanically difficult and instead a non-collocated scheme is used.

1.1.1 Case Study

The case study used in [Paper I and III] is concerned with a 1 m diameter faceplate made of borosilicate. The force actuators, in total 372 with an actuator pitch of 45 mm, are placed in a Cartesian topology, with the non-collocated sensors placed between the actuators. The layout is shown in Fig. 1.2, where the actuators are marked with x:s and the sensors with o:s. The feedback signal for control of an actuator is taken as the average of the four adjacent sensors. The 2 mm thick mirror is constrained at the inner rim, which has a diameter of 5 mm. This type of boundary condition allows the faceplate, through proper

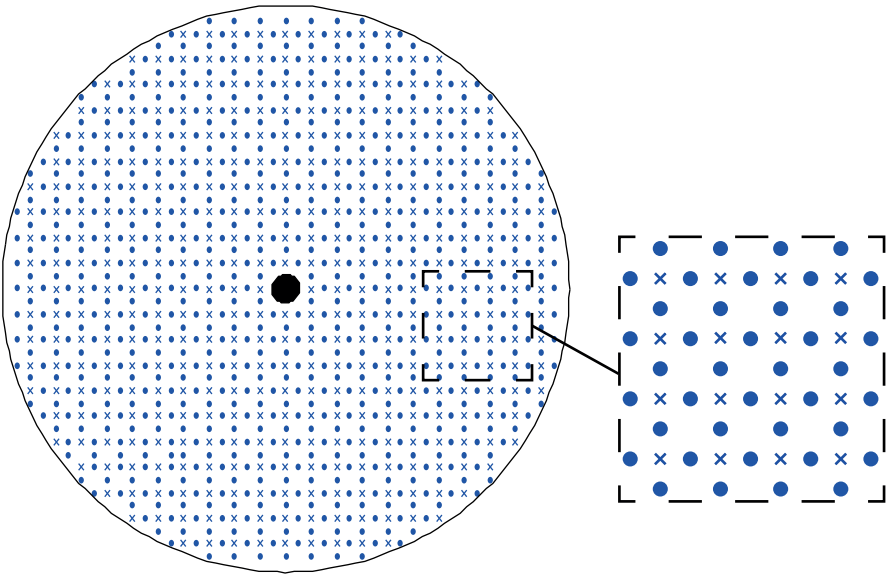

Figure 1.2: The topology of the actuators (marked with x:s) and the sensors (marked with o:s) for a case study. The mirror has a diameter of 1 m and it is supported at the inner rim. The actuator pitch is 45 mm with non-collocated sensors placed between actuators.

actuation, to be closely controlled in tip/tilt.

A finite element model of the faceplate was derived using the software COMSOL Multiphysics[6] and a modal analysis was performed in MATLAB[7]. In addition, the time-domain simulation in [Paper III] was done using Python[8].

1.2 Objective

The objective of this thesis is, through appropriate research, to show feasibility of the low-cost design for a large DM (described in Sec. 1.1) for AO in optical telescopes. For this, in-depth knowledge of structural dynamics, adaptive optics, control systems with a large number of actuators and sensors, and integrated modeling is needed. With the modeling work we wish to show feasibility of the concept and to investigate the possibility of building a laboratory experimental setup. Furthermore, the knowledge gained can be

[6]COMSOL Multiphysics is a trademark of COMSOL, Inc.
[7]MATLAB is a trademark of The MathWorks, Inc.
[8]Open source programming language, ©2001–2010 Python Software Foundation.

used for design of large DMs based on other operating concepts.

The next chapter presents a theoretical study of issues covered in this thesis. Both an analytical and a numerical approach for describing the dynamical behavior of a faceplate are presented. Furthermore, a short introduction is given to state-space models.

The internal control system for the deformable mirror is presented in Chapter 3. The controller encompasses rate and position feedback. Small sets of actuators are combined into actuator families to reduce cross-talk between adjacent actuators. This local control approach is based upon the method of least squares and the key features of the approach are presented.

In Chapter 4, the size of DMs is discussed. A dimensionless modal analysis is used to evaluate how different design parameters, among others the diameter, affect the dynamical behavior of a faceplate. Also, a discussion of the size of the actuator families relative to the size of the DM is presented.

The optical setup for a laboratory experiment is presented in Chapter 5. The setup comprises a Celestron C14 telescope and the SciMeasure LJ CCD39 detector, which are components available at the department. These components limit the imaging capability, thus a partially illuminated 1 m diameter aluminum faceplate with a small number of active actuators is suggested for a first experiment.

Chapter 2

Faceplate Dynamics

This thesis is concerned with modeling of AO systems encompassing large thin-plate deformable mirrors. Given that, a sound theoretical background for deflection of faceplates is presented. Some of the theory and knowledge was developed during the 18th and 19th century, and constitutes with computers of today a powerful tool. The dynamics of faceplates can be modeled mathematically either by partial differential equations based on the principle of virtual work (Sec. 2.1) or by linear differential equations based on Newton's laws using the method of finite elements (Sec. 2.2). A modal analysis is presented for both approaches. In addition, a modal participation factor derivation is performed in Sec. 2.1.1.

2.1 Analytical Modeling

The partial differential equation governing the time varying deflections perpendicular to the surface in polar coordinates, for isotropic, homogeneous and undamped plates for which the in-plane deformations can be neglected (Kirchhoff-Love theory of plates [12, 13]), is given by [14]

$$D\nabla_r^2\nabla_r^2 w(r,\phi,t) + \rho h \frac{\mathrm{d}^2 w(r,\phi,t)}{\mathrm{d}t^2} = l(r,\phi,t). \tag{2.1}$$

Here, D is the flexural rigidity, $w(r,\phi,t)$ deflection with respect to the undeformed reference plate, r and ϕ polar coordinates, t time, ρ material density, h thickness of the plate and $l(r,\phi,t)$ the load per unit area. The terms on the left hand side of the equation can be seen as the contribution from the stiffness and acceleration, respectively. The biharmonic

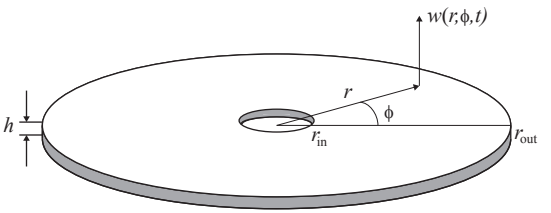

Figure 2.1: Principle layout of the faceplate modeled as a Kirchhoff plate. The radius of the inner hole r_{in} and the radius of the faceplate r_{out} are shown.

operator, ∇_r^2, is defined as

$$\nabla_r^2 \equiv \frac{\mathrm{d}^2}{\mathrm{d}r^2} + \frac{1}{r}\frac{\mathrm{d}}{\mathrm{d}r} + \frac{1}{r^2}\frac{\mathrm{d}^2}{\mathrm{d}\phi^2}. \tag{2.2}$$

The boundary conditions for a free edge, where the radial moment and the radial shear forces are zero, at the outer edge of a faceplate (see Fig. 2.1) are given by [15]

$$D\left(\frac{\mathrm{d}^2 w}{\mathrm{d}r^2} + \frac{\nu}{r}\frac{\mathrm{d}w}{\mathrm{d}r} + \frac{\nu}{r^2}\frac{\mathrm{d}^2 w}{\mathrm{d}\phi^2}\right)\bigg|_{r=r_{\text{out}}} = 0 \tag{2.3}$$

$$D\left(\frac{\mathrm{d}}{\mathrm{d}r}\nabla_r^2 w - (1-\nu)\frac{\mathrm{d}^2}{\mathrm{d}\phi^2}\left(\frac{1}{r^2}\frac{\mathrm{d}w}{\mathrm{d}r} - \frac{w}{r^3}\right)\right)\bigg|_{r=r_{\text{out}}} = 0 \tag{2.4}$$

where ν is Poisson's ratio. For the clamped inner rim, the boundary conditions are given by

$$w(r_{\text{in}}, \phi, t) = 0 \tag{2.5}$$

$$\frac{\mathrm{d}w}{\mathrm{d}r}\bigg|_{r=r_{\text{in}}} = 0 \tag{2.6}$$

because the lateral displacement and the slope are zero.

With Eq. 2.1 and the boundary conditions (given by Eq. 2.3-2.6), the dynamic behavior of a free homogeneous faceplate can be studied. Solutions can be found by separation of variables with $w(r,\phi,t) = W(r,\phi)e^{-i\omega t}$, where ω is the angular frequency. It is then possible to transform Eq. 2.1 into

$$(\nabla_r^2 - \beta^2)W(r,\phi) = 0 \tag{2.7}$$

where the lateral forces are zero and $\beta^4 = \frac{\rho h \omega^2}{D}$. The general harmonic solution to the homogenous equation (Eq. 2.7) can be written as the sum of two independent spatial parts

[16]

$$W_k(r,\phi) = W_{1,k}(r,\phi) + W_{2,k}(r,\phi) \tag{2.8}$$

$$W_{1,k}(r,\phi) = [A_{1,k}J_k(\beta_k r) + A_{3,k}Y_k(\beta_k r)]\sin(k\phi) + [A_{2,k}J_k(\beta_k r) + A_{4,k}Y_k(\beta_k r)]\cos(k\phi) \tag{2.9}$$

$$W_{2,k}(r,\phi) = [B_{1,k}I_k(\beta_k r) + B_{3,k}K_k(\beta_k r)]\sin(k\phi) + [B_{2,k}I_k(\beta_k r) + B_{4,k}K_k(\beta_k r)]\cos(k\phi) \tag{2.10}$$

where J_k and Y_k are Bessel functions of order $k \in \mathbb{N}$ and of the first and second kind, respectively. The second term of Eq. 2.8 involves the modified Bessel functions I_k and K_k of the order k and of the first and second kind.

The modal analysis, determining $W_k(r,\phi)$:s and ω_k:s, is made from Eq. 2.8–2.10 and the boundary conditions. Each eigenmode is given by eight coefficients $A_{i,k}$ and $B_{i,k}$ for $i = 1...4$. These coefficients can be determined by the eight equations obtained from the the boundary conditions (both the sine and cosine parts of Eq. 2.8–2.10 must fulfill the boundary conditions). The resulting equations can be written in matrix form as

$$\mathbf{\Lambda}(\beta_k)_{\sin}\begin{Bmatrix} A_{1,k} \\ A_{3,k} \\ B_{1,k} \\ B_{3,k} \end{Bmatrix} = 0 \qquad \mathbf{\Lambda}(\beta_k)_{\cos}\begin{Bmatrix} A_{2,k} \\ A_{4,k} \\ B_{2,k} \\ B_{4,k} \end{Bmatrix} = 0 \tag{2.11}$$

where $\mathbf{\Lambda}(\beta_k)_{\sin}$ and $\mathbf{\Lambda}(\beta_k)_{\cos}$ are 4-by-4 matrices with elements determined by the boundary conditions. The eigenfrequencies for the eigenmodes are found by

$$\det(\mathbf{\Lambda}(\beta_k)) = 0 \tag{2.12}$$

which must hold for all non-trivial solutions of Eq. 2.11. In [Paper II], the eigenfrequencies were determined by the Ritz method [17] (other numerical methods can be used as well).

2.1.1 Modal Participation Factors

The analytical model (described above) can be used to derive the *modal participation factors*, which measure the coupling between an exciting harmonic point force and a given mode shape. The deflection of the mirror can be written using a superposition of the eigenmodes as

$$w(r,\phi,t) = \sum_{k=1}^{\infty} c_k W_k(r,\phi) e^{-i\omega t} \tag{2.13}$$

where $W_k(r,\phi)$ again is the kth eigenmode and c_k the modal participation factor, with the dimension of length, for that normal mode.

Here, the steps are presented which are needed to derive values of the modal participation factors. $W_k(r,\phi)$ is defined as the dimensionless eigenmode satisfying the orthonormality relations

$$\frac{1}{A}\int_{r_i}^{r_o}\int_0^{2\pi} W_k(r,\phi)W_l(r,\phi)r\mathrm{d}r\mathrm{d}\phi = \delta_{k,l} \tag{2.14}$$

where $\delta_{k,l}$ is the Kronecker delta and A is the total area of the faceplate. The external load reads

$$l(r,\phi,t) = u\frac{1}{r}\delta(r-R)\delta(\phi-\Phi)e^{-i\omega t} \tag{2.15}$$

for a point force u at the position (R,Φ), where $\delta(x)$ is Dirac's delta function, which then gives [18]

$$\int_0^{\infty}\int_0^{2\pi}\frac{1}{r}\delta(r-R)\delta(\phi-\Phi)r\mathrm{d}\phi\mathrm{d}r = 1. \tag{2.16}$$

Using Eq. 2.13 to describe the deflection of the faceplate and Eq. 2.15 to describe the external forces, use of the faceplate dynamics Eq. 2.1 gives

$$D\nabla_r^4\sum_{k=1}^{\infty}c_kW_k(r,\phi) - \rho h\omega^2\sum_{k=1}^{\infty}c_kW_k(r,\phi) = u\frac{1}{r}\delta(r-R)\delta(\phi-\Phi) \tag{2.17}$$

where $e^{-i\omega t}$ has been eliminated from the equation. Using the identity of the eigenfunctions, given by Eq. 2.7, this equation can be simplified to

$$\rho h\sum_{k=1}^{\infty}(\omega_k^2-\omega^2)c_kW_k(r,\phi) = u\frac{1}{r}\delta(r-R)\delta(\phi-\Phi) \tag{2.18}$$

Multiplying with one specific eigenmode $W_l(r,\phi)$ and integrating over the full faceplate gives

$$\int_{r_i}^{r_o}\int_0^{2\pi}W_l(r,\phi)\rho h\sum_{k=1}^{\infty}(\omega_k^2-\omega^2)c_kW_k(r,\phi)r\mathrm{d}r\mathrm{d}\phi \tag{2.19}$$

$$= \int_{r_i}^{r_o}\int_0^{2\pi}W_l(r,\phi)u\frac{1}{r}\delta(r-R)\delta(\phi-\Phi)r\mathrm{d}r\mathrm{d}\phi \tag{2.20}$$

The left hand side can be reduced by using the orthonormality condition of the eigenmodes and the right hand side is reduced, since the Dirac delta function is zero outside (R,Φ). Thus, the participation factor can be expressed as

$$A\rho h(\omega_l^2-\omega^2)c_l = uW_l(R,\Phi) \tag{2.21}$$

$$c_l = \frac{uW_l(R,\Phi)}{M(\omega_l^2-\omega^2)} \tag{2.22}$$

where M is the total mass of the faceplate. The unrealistic behavior of $c_l \rightarrow \infty$ when $\omega \rightarrow \pm\omega_l$ occurs, since the damping of the system has yet not been considered. By comparing with a second-order system (with and without damping), an analogy can be made to the formula for the modal participation factor as

$$c_l = \frac{uW_l(R,\Phi)}{M(\omega_l^2 - \omega^2 + 2\mathrm{i}\zeta_l\omega\omega_l)} \tag{2.23}$$

where ζ is the modal damping ratio. This way of describing the modal participation factors is used in [Paper II] to compute frequency responses for a faceplate.

2.2 Finite Element Modeling

The dynamic equations for a finite element model (FEM), the most common discretization technique in structural mechanics, are formed by setting the inertial forces minus the forces related to friction and elasticity equal to the external forces for the nodes [19, 20]

$$\mathbf{M}\ddot{\boldsymbol{\xi}} + \mathbf{E}\dot{\boldsymbol{\xi}} + \mathbf{K}\boldsymbol{\xi} = \mathbf{f} \tag{2.24}$$

where $\mathbf{M}$ is the mass matrix, $\mathbf{E}$ the damping matrix, $\mathbf{K}$ the stiffness matrix, $\mathbf{f}$ a time-dependent force vector for the external forces, and $\boldsymbol{\xi}$ a vector holding node and angular displacements. For modal analysis, the structural damping is initially neglected, so that Eq. 2.24 becomes

$$\mathbf{M}\ddot{\boldsymbol{\xi}} + \mathbf{K}\boldsymbol{\xi} = \mathbf{f}. \tag{2.25}$$

Each vibration mode can be represented by $\boldsymbol{\psi}\sin\omega t$, where $\boldsymbol{\psi}$ is a column vector holding nodal deflections describing the eigenmode. To obtain the mode shapes, the vibration modes are inserted into Eq. 2.25 and the external forces are set to zero

$$(\mathbf{K} - \omega^2\mathbf{M})\boldsymbol{\psi} = 0. \tag{2.26}$$

Hence, $(\mathbf{K}-\omega^2\mathbf{M})$ must be singular to fulfill the equation, since the trivial solution $\boldsymbol{\psi} = 0$ is of no interest. Assuming there are n degrees of freedom, then the eigenvectors, $\boldsymbol{\psi}$, can be combined into an eigenvector matrix

$$\boldsymbol{\Psi} = [\boldsymbol{\psi}_1, \boldsymbol{\psi}_2 ... \boldsymbol{\psi}_n]. \tag{2.27}$$

The associated eigenfrequencies can be arranged as a diagonal matrix

$$\boldsymbol{\Omega} = \mathrm{diag}(\omega_1, \omega_2 ... \omega_n). \tag{2.28}$$

The modal displacement vector, $\mathbf{q}$, is defined by, $\boldsymbol{\xi} = \boldsymbol{\Psi}\mathbf{q}$, i.e. a transformation from modal to nodal coordinates. Inserting the coordinate transformation and premultiplying Eq. 2.25 with $\boldsymbol{\Psi}^{\mathrm{T}}$ gives

$$\boldsymbol{\Psi}^{\mathrm{T}}\mathbf{M}\boldsymbol{\Psi}\ddot{\mathbf{q}} + \boldsymbol{\Psi}^{\mathrm{T}}\mathbf{K}\boldsymbol{\Psi}\mathbf{q} = \boldsymbol{\Psi}^{\mathrm{T}}\mathbf{f}. \tag{2.29}$$

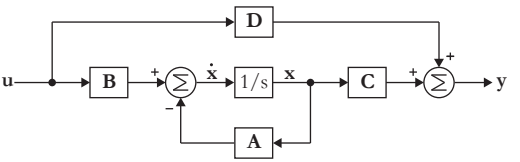

Figure 2.2: Block diagram representation of the state-space equations, where the states of the system, **x**, are shown.

Mass normalizing the eigenvectors so that $\boldsymbol{\Psi}_{\mathrm{m}}^{\mathrm{T}}\mathbf{M}\boldsymbol{\Psi}_{\mathrm{m}} = \mathbf{I}$, simplifies the expression to [21]

$$\ddot{\mathbf{q}} + \boldsymbol{\Omega}^2\mathbf{q} = \boldsymbol{\Psi}_{\mathrm{m}}^{\mathrm{T}}\mathbf{f}, \tag{2.30}$$

where $\boldsymbol{\Psi}_{\mathrm{m}}^{\mathrm{T}}\mathbf{K}\boldsymbol{\Psi}_{\mathrm{m}} = \boldsymbol{\Omega}^2$ follows from Eq. 2.26. The viscous damping is normally reintroduced at this stage [22]

$$\ddot{\mathbf{q}} + \mathbf{E}_{\mathrm{q}}\dot{\mathbf{q}} + \boldsymbol{\Omega}^2\mathbf{q} = \boldsymbol{\Psi}_{\mathrm{m}}^{\mathrm{T}}\mathbf{f}, \tag{2.31}$$

where $\mathbf{E}_{\mathrm{q}}$ is a diagonal matrix with real damping coefficients. Comparing Eq. 2.31 to that of a second-order system, a diagonal matrix can be introduced $\mathbf{Z} = \frac{1}{2}\mathbf{E}_{\mathrm{q}}\boldsymbol{\Omega}^{-1}$, which holds the modal damping ratios. Thus, the dynamics of the faceplate, for the modal case, is obtained from

$$\ddot{\mathbf{q}} + 2\mathbf{Z}\boldsymbol{\Omega}\dot{\mathbf{q}} + \boldsymbol{\Omega}^2\mathbf{q} = \boldsymbol{\Psi}_{\mathrm{m}}^{\mathrm{T}}\mathbf{f}. \tag{2.32}$$

2.3 State Space Representation

In a state space system [23, 24], the internal states of the system, **x**, are explicitly described by the state equation.The state variables are the smallest possible subset of system variables that can represent the entire state of the system at any given time. The system output, **y**, is given in terms of combination of the current system state, and the current system input, **u**, through the output equation. These two equations describe a system on *ABCD-form*:

$$\dot{\mathbf{x}} = \mathbf{A}\mathbf{x} + \mathbf{B}\mathbf{u} \tag{2.33}$$

$$\mathbf{y} = \mathbf{C}\mathbf{x} + \mathbf{D}\mathbf{u} \tag{2.34}$$

where **A** is the system matrix, **B** the input matrix, **C** the output matrix, and **D** the feedforward matrix. The block diagram of the state-space equations is shown in Fig. 2.2.

In this thesis, the feedforward matrix **D** is considered to be a null matrix (if nothing else is stated), thus the second term of Eq. 2.34 can be omitted. The state vector **x** for the state-space model of the faceplate, for the modal case given by Eq. 2.32, is defined as

$$\mathbf{x} = \left\{ \begin{array}{c} \mathbf{q} \\ \dot{\mathbf{q}} \end{array} \right\}. \tag{2.35}$$

The modal displacement vector, $\mathbf{q}$, is of length n, thus the state vector has length $2n$. Further, the $\mathbf{A}$,$\mathbf{B}$, and $\mathbf{C}$ matrices for Eq. 2.32 are given by

$$\mathbf{A} = \begin{bmatrix} \mathbf{0}_{n\times n} & \mathbf{I} \\ -\mathbf{\Omega}^2 & -2\mathbf{Z\Omega} \end{bmatrix} \tag{2.36}$$

$$\mathbf{B} = \begin{bmatrix} \mathbf{0}_{n\times n} \\ \mathbf{\Psi}_{\mathrm{m}}^{\mathrm{T}} \end{bmatrix} \tag{2.37}$$

$$\mathbf{C} = \begin{bmatrix} \mathbf{\Psi}_{\mathrm{m}} & \mathbf{0}_{n\times n} \end{bmatrix} \tag{2.38}$$

and the input vector is equal to $\mathbf{f}$.

The ABCD-form is advantageous in integrated modeling, because the dynamical behavior of different parts of a system can be modeled with similar equations. Also, through use of block diagram algebra, various submodels of optical and other systems may be included in ABCD models (a good example is found in [25] where an integrated model of adaptive optics in telescopes is presented). Results can be obtained either in the frequency domain as transfer functions

$$\frac{\mathrm{y}}{\mathrm{u}} = \mathbf{C}(i\omega\mathbf{I} - \mathbf{A})\mathbf{B}^{-1} \tag{2.39}$$

or in the time-domain as time-series, when the ordinary differential equations (the state-space equations) are solved.

Chapter 3

Control System

A schematic block diagram of a typical AO system is shown in Fig. 3.1 with a controller, which often encompasses a reconstructor and an integrator. The disturbance input is a combination of the atmospheric disturbance and imperfections in the optical elements of the telescope. The task is to develop a DM, i.e. a mirror with internal control, which responds similarly for different spatial frequencies over a sufficient dynamic range. The characteristics of the mirror of the case study given in Sec. 1.1.1 and used in [Papers I and III] are shown in Fig. 3.2. There is a global static response to an actuator poke, and the dynamic behavior is given in the Bode diagram.

It is convenient to conceptually divide the control problem of the mirror into two steps; adding electronic damping and adding electronic stiffness. There are two key requirements that must be fulfilled for control. First it must be demonstrated that damping can be added, preserving stability despite the need to eventually roll-off due to finite actuator/sensor response (i.e. compensating for the behavior in Fig. 3.2b). And second, a satisfactory local influence function for an actuator must be obtained without prior de-

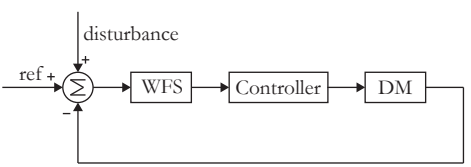

Figure 3.1: Schematic block diagram of a typical adaptive optics system, including a wavefront sensor, a controller, and a deformable mirror.

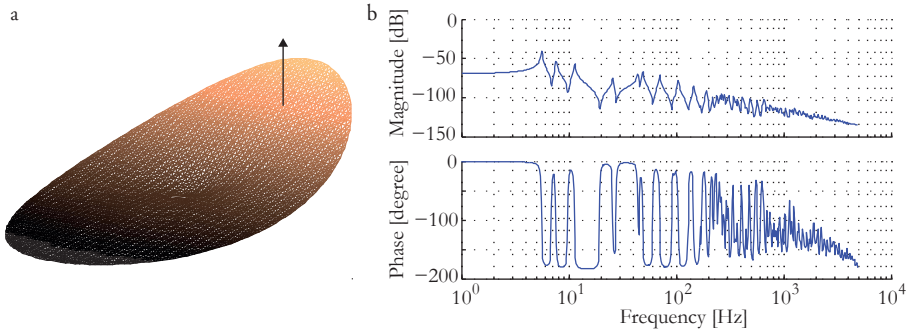

Figure 3.2: a) Static response for a single actuator poke; the influence function is similar to a tip/tilt mode. b) Representative transfer function for an actuator location from force perpendicular to the faceplate to position of the faceplate.

tailed knowledge of the faceplate structure (i.e. compensating for the behavior in Fig. 3.2a), since use of an accurate mirror model could limit robustness of the control system.

3.1 Velocity Control

The purpose of conceptually dividing the feedback into rate control ("electronic" or "active" damping) and position control is that the latter is more straightforward to design once the former loop is closed. Collocated rate feedback is guaranteed to be robustly stable [26]. This statement is also true for non-collocation provided that instability is not caused by the phase lag introduced by the actuator-sensor spacing. However, in reality, rate control has a finite bandwidth due to sensor and actuator dynamics. With a finite bandwidth, the phase criterion for stability will be violated for a structure with no natural damping. In contrast, with non-zero damping, it is possible to roll-off the rate feedback without violating the stability condition. This can be understood from Fig. 3.2b, showing that the transfer function changes from being dominated by resonances and anti-resonances to being relative smooth above a certain frequency, in both magnitude and phase. The transition frequency, here named the *acoustic frequency*, is located where different resonances and anti-resonances begin to overlap. The starting point of the acoustic behavior can be found for a free-free faceplate, without boundary conditions, by the following steps. The modal density for a faceplate can be written as [27]

$$N = \frac{\omega A}{2\pi c_g c_p} \tag{3.1}$$

where ω is the natural angular frequency, A the plate area, c_{g} the group velocity, and c_{p} the phase velocity. For bending vibrations in a thin plate, the phase velocity is [27]

$$c_{\mathrm{p}} = \sqrt{\omega}\left(\frac{D}{\rho h}\right)^{1/4}, \tag{3.2}$$

and the group velocity is twice the phase velocity [28]. Inserting Eq. 3.2 into Eq. 3.1 results in

$$N = \frac{A}{4\pi}\sqrt{\frac{\rho h}{D}} \tag{3.3}$$

Further, the average modal spacing is described by $\Delta\omega = 1/N$, and the half-power bandwidth of each mode is $2\zeta f_{\mathrm{ac}}$, where f_{ac} is the undamped frequency and ζ is the modal damping. The acoustic frequency is then given by

$$f_{\mathrm{ac}} = \frac{n_{\mathrm{f}}}{A\zeta}\sqrt{\frac{D}{\rho h}} \tag{3.4}$$

where n_{f} is a factor by which the half-power bandwidth needs to exceed the average modal spacing. Comparing this equation with Fig. 3.2b (even though the theory is not strictly valid for the figure case), $n_{\mathrm{f}} \approx 4$ matches the transition to the acoustic region, i.e. there should be a minimum of four eigenmodes participating at every frequency for the acoustic behavior to occur.

3.2 Local Position Control

The velocity loops referred to above establish necessary damping, effectively creating a well-damped mirror structure. The goal is to control the deflection, i.e. the position, at any given place. This is done using feedback signals from the sensors on the back of the mirror.

Position feedback control of the faceplate is in principle guaranteed stable, since an actuator controlled with position feedback can be seen as a passive component (spring/damper) dissipating energy from the faceplate. The closed-loop performance using a single actuator is indeed robust and gives a high-bandwidth control, but closing all of the actuator/sensor loops simultaneously is problematic. This is evident from the global response to an actuation in Fig. 3.2a. The loop gain for the faceplate is higher for low spatial frequency deflection patterns than for high, so the plant is ill-conditioned. Hence, for a non-zero error at one location, the controller would apply solely a command to a single actuator, giving a global response to a local error. An innovation of this thesis work is to use only local actuation in response to a displacement error providing a remarkably good compromise between performance and robustness.

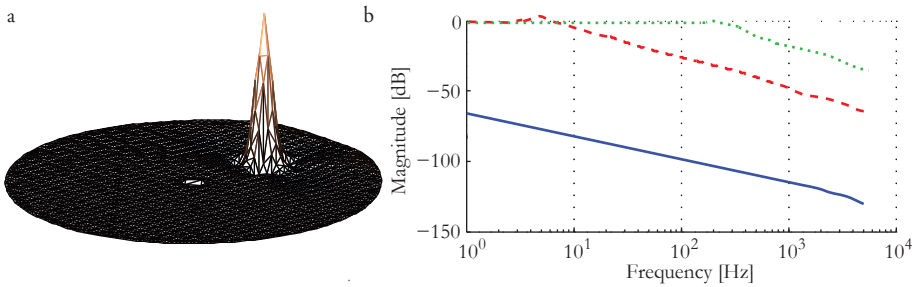

Figure 3.3: a) Static response for an actuator family; the influence function is local. b) Transfer function for commanded tilt mode to actual position on the faceplate. The full curve shows the system with the rate feedback closed, the dashed curve shows the case when **Q** is included, and the dotted curve shows the case when the position feedback is also included.

The static response of the faceplate to an actuator command is $\boldsymbol{\xi} = \mathbf{K}_{\mathrm{a}}^{-1}\mathbf{f}$, where $\mathbf{K}_{\mathrm{a}}$ is a stiffness matrix in which the uncontrollable rigid body modes have been projected out. Define the state vector $\boldsymbol{\xi}_{\mathrm{a},j}$ for a unit displacement of the jth actuator

$$\begin{aligned} \xi_{\mathrm{a},i} &= 0 \quad \text{for} \quad i \neq j \\ \xi_{\mathrm{a},i} &= 1 \quad \text{for} \quad i = j \end{aligned}$$

and choose the actuator force pattern $\mathbf{f}_{\mathrm{a},j}$ that minimizes the cost function

$$J = ||\mathbf{K}_{\mathrm{a}}^{-1}\mathbf{f}_{\mathrm{a},j} - \boldsymbol{\xi}_{\mathrm{a},j}||_2. \tag{3.5}$$

The force vector $\mathbf{f}_{\mathrm{a},j}$ is subjected to the following constraint

$$\begin{aligned} f_{\mathrm{a},i} &= 0 \quad \text{for} \quad i \notin \text{family} \\ f_{\mathrm{a},i} &\in \mathbb{R} \quad \text{for} \quad i \in \text{family}, \end{aligned}$$

i.e. the elements not belonging to the jth actuator family must be zero. That is, choose a local set of forces to minimize the error over the entire mirror, when matching the desired displacement pattern. The influence function of an actuator family is shown in Fig. 3.3a, which can be compared to the influence function of a single actuator in Fig. 3.2a. The computed force patterns for each actuator are assembled into columns in a family matrix **Q**, which then is an approximate inverse to the system at zero-frequency (see Fig. 3.4). Since **Q** is an approximate static inverse of the plant, the resulting system is decoupled and normalized to unit gain at zero frequency.

Performance features of the control system are shown in Fig. 3.3b. Here, the input is the average value of the commanded tilt mode at the actuator locations and the output is the average measured value of the tilt mode at the actuator locations. The full curve shows the

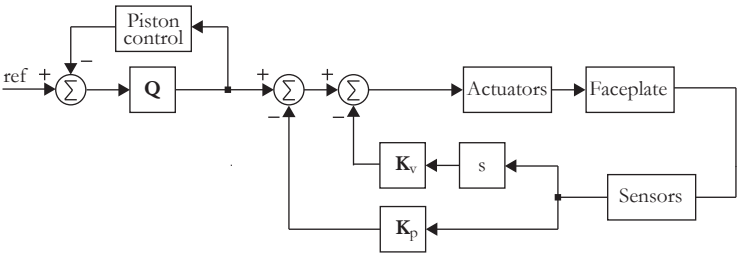

Figure 3.4: A schematic block diagram of the suggested control system for the deformable mirror, including rate, position and piston feedback. In addition, the **Q**-block (the family matrix) can be viewed as feedforward control. The piston control loop reduces unnecessary stress around the inner rim of the faceplate.

case when only the rate feedback loop is closed, the dashed curve shows the case when the family matrix is included, and the dotted curve shows the case, when the position feedback is closed. The added stiffness from the position feedback loops increases the bandwidth, i.e. the eigenfrequencies are shifted towards higher frequencies. Note, the Bode diagrams in Fig. 3.3b have been determined with the assumption that the position sensors placed at the back of the mirror are ideal.

A block diagram of the control system is shown in Fig. 3.4. The differentiator in the rate feedback is used to obtain a velocity signal. The piston loop is closed around the family matrix, and it is designed to alleviate unnecessary stress that can slowly build up at the fixed inner rim of the faceplate. A solution superior to driving the piston to zero is to subtract the mean force of the actuators closest to the rim from the force command at every location with a small gain. The piston loop is guaranteed stable as long as the piston mode is unobservable by the AO system.

3.3 Properties of Local Control

The least squares problem of Eq. 3.5 is equivalent to solving

$$\boldsymbol{\mathcal{C}}_{\mathrm{f},\boldsymbol{j}}\mathbf{f}_{\mathrm{f},\boldsymbol{j}} = \boldsymbol{\xi}_{\mathrm{a},j}, \tag{3.6}$$

where the elements in the force vector $\mathbf{f}_{\mathrm{f},\boldsymbol{j}}$ and the columns of the compliance matrix $\boldsymbol{\mathcal{C}}_{\mathrm{f},\boldsymbol{j}}$ for the actuators not belonging the jth family have been eliminated. The force vector which is a solution to the least squares problem is then given by

$$\mathbf{f}_{\mathrm{f},\boldsymbol{j}} = (\boldsymbol{\mathcal{C}}_{\mathrm{f},j}^T\boldsymbol{\mathcal{C}}_{\mathrm{f},j})^{-1}\boldsymbol{\mathcal{C}}_{\mathrm{f},j}^T\boldsymbol{\xi}_{\mathrm{a},j}. \tag{3.7}$$

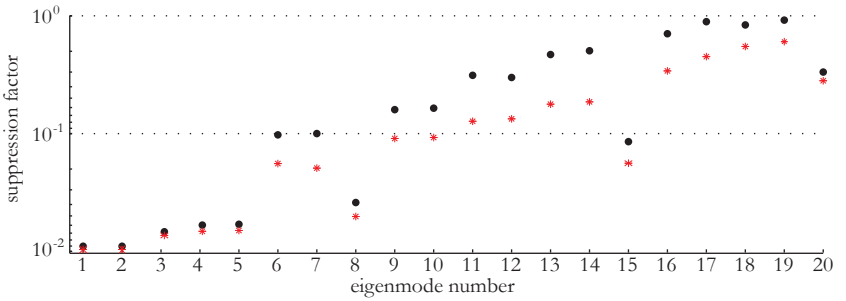

Figure 3.5: The suppression factors for two different family sizes are plotted for the first twenty eigenmodes. The circles are for $\mathcal{Q}_{21}$ and the stars are for $\mathcal{Q}_{59}$, i.e. families including 21 and 59 actuators. The rotationally symmetric eigenmodes 8, 15, and 20 are highly attenuated because their modal stiffness is much higher in the radial direction.

That is, compute $(\boldsymbol{\mathcal{C}}_{\mathrm{f},j}^T\boldsymbol{\mathcal{C}}_{\mathrm{f},j})^{-1}\boldsymbol{\mathcal{C}}_{\mathrm{f},j}^T$ and insert the results at the appropriate locations in the columns of $\mathbf{Q}$. The computational power needed to calculate the family force commands is low. Thus, it is easy to correct for unexpected behavior, such as malfunctioning actuators during operation.

The local family force patterns derived in Eq. 3.5, have properties not only related to the static case. Due to use of the family concept, a number of low-order eigenmodes are not excited, in addition to the tip/tilt-mode which otherwise dominates the global response with actuation by a single actuator, see Fig. 3.2a. Suppression of low-order eigenmodes can be studied by computing modal participation factors, derived in Sec. 2.1.1. In [Paper II], a method is formulated which compares the modal participation of the local control concept to actuation with a single actuator by defining a factor for the suppression of the eigenmodes using the actuator family compared to a single actuator. The modal suppression factors are defined as

$$\begin{aligned}\mathcal{Q}_{21} &= \frac{c_{k,21}}{c_{k,1}}\\ \mathcal{Q}_{59} &= \frac{c_{k,59}}{c_{k,1}}\end{aligned}$$

where for instance $c_{k,21}$ is the modal participation factor for the kth eigenmode of a family encompassing 21 actuators. The family size affects the number of modes which are suppressed as shown in Fig. 3.5. By inspection it can be seen that the number of eigenmodes suppressed roughly follows the Nyquist criterion. That is, an eigenmode needs about two degrees of freedom (two actuators) to be attenuated. The rotationally symmetric eigenmodes 8, 15 and 20 have deviating suppression factors due to eigenmodes with rotationally symmetry are locally (the area that an actuator family occupies) similar

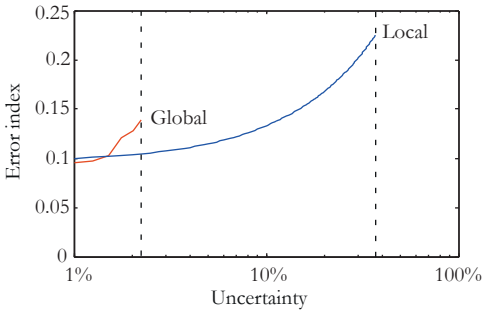

Figure 3.6: Performance robustness comparison for a local and a global approach for the feedforward control. Uncertainty is random errors in the mirror resonant frequencies, and the error index is the mean-square of the residuals between the commanded input and the measured output over temporal frequency region from 0 to 50 Hz. The error index is infinite (indicated by the dashed line) when the closed-loop system is not stable.

to the tip/tilt mods which are highly suppressed.

As mentioned in Sec. 3.2, use of the family matrix can be viewed as feedforward control. A more conventional way to derive a feedforward matrix is through a global strategy by inverting the static performance of the system. The drawback of that method compared to the actuator family approach is that a detailed and precise knowledge of the system is required to ensure robustness. This is illustrated in Fig. 3.6, where the robustnesses of the two different approaches are compared. The vertical dashed lines indicate the uncertainty level at which the approaches are not guaranteed stable. Here, uncertainty is random errors in the eigenfrequencies and the error index is the mean-square of the residuals between the commanded input and the measured output averaged over the temporal frequency region from 0 to 50 Hz. The local position control approach gives similar performance for small uncertainties as the global approach, and maintains stability up to an uncertainty level of 38%, more than 15 times what can be tolerated with the global approach.

The local control approach has one disadvantage, which is the reduced stroke to force ratio, defined as the mirror deflection at an actuator location divided by the maximum force in a family or the force in the actuator for the single actuator case. The force distribution of an actuator family constituted of 21 actuators is shown in Fig 3.7, for a Cartesian actuator topology. The forces are normalized against the force needed for an unit deflection with a single actuator. As can be seen, the stroke to force ratio is about twelve times less with a family than with a single actuation. The disadvantage is less with a larger number of actuators in the family. Further, it can be seen that the sum of forces in the family is close to zero, which is also the case for the moment. Thus, the family concept can be

	0.10	0.81	-0.01	
0.02	0.61	-4.78	0.92	-0.09
0.84	-4.55	12.1	-4.63	0.91
-0.11	0.99	-4.82	0.89	-0.10
	0.01	0.76	0.07	

Figure 3.7: The relative distribution of force in an actuator family. The forces are normalized against the force needed to achieve unit deflection with a single actuator.

viewed as an extension of the Saint-Venant's principle beyond the static case.

Chapter 4

Deformable Mirror Properties Implications

Adaptive optics systems have until now most often been implemented post-focus with relay optics and one or more small DMs. However, for reasons of efficiency, it is attractive to include the deformable mirror directly in the telescope and it must then be larger. This also makes it possible to include more actuators than what is possible for traditional DMs of a few tens of centimeters. This is required for the success of the Extremely Large Telescopes. It is therefore of interest to study the various implications of increasing the size of a mirror. A dimensionless modal analysis has been performed and will be described in Sec. 4.1. Further, the actuator family concept is evaluated for different sizes of mirrors in Sec. 4.2.

4.1 Dimensionless Modal Analysis

The analytical approach presented in Sec. 2.1 describes the dynamical behavior of faceplates by a partial differential equation based on the principle of virtual work. This theory is used in [Paper II] to describe how the dynamic properties of faceplates depend on their physical and material parameters. This is accomplished by deriving a dimensionless modal analysis, which is performed in a polar coordinate system. The normalized and dimensionless radius, ξ, is defined as

$$\xi = \frac{r}{r_{\text{out}}} \tag{4.1}$$

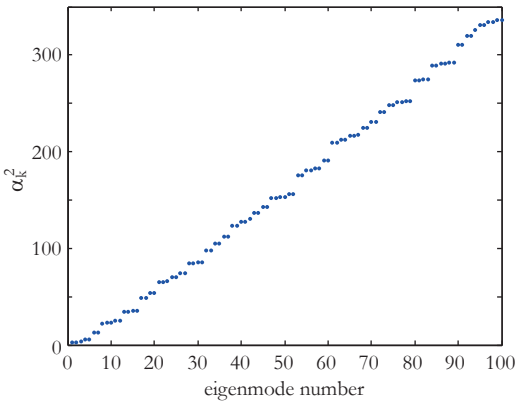

Figure 4.1: The first hundred α_k:s for the mirror model described in Sec. 2.1.1. The set of α_k:s is the same for a given structure when the material parameters are changed, as long as the boundary conditions are unaltered. Thus, the set can be used to evaluate the influence of different material properties.

where r_{out} is the outer radius of the circular faceplate. As before, the polar angle is called ϕ. The homogenous solution to Eq. 2.1 (the equivalent to Eq. 2.7), for the case when ξ, is used instead of r, is given by

$$\nabla_\xi^4 W(\xi, \phi) = \alpha W(\xi, \phi) \tag{4.2}$$

where ∇_ξ^4 is the biharmonic operator for the ξ - ϕ coordinate plane. It is related to ∇_r^4 defined in Eq. 2.2 as

$$\nabla_r^4 = \frac{1}{r_{\text{out}}^4} \nabla_\xi^4. \tag{4.3}$$

The parameter α in Eq. 4.2 is defined by

$$\alpha^4 = \frac{r_{\text{out}}^4 \omega^2 \rho h}{D} \tag{4.4}$$

where ρ is the density, h the thickness, ω the angular eigenfrequency, and D the flexural rigidity of the faceplate. That is, for a specific structural design, with the same boundary conditions, a set of α_k:s can be derived, which remain the same for any given material properties. This characteristic can be used to relate the angular eigenfrequencies, ω_k:s, for different choices of material to the α_k's

$$\frac{\omega_k}{\omega_0} = \alpha_k^2 \quad \text{for} \quad \omega_0 = \sqrt{\frac{Eh^2}{12 r_{\text{out}}^4 \rho (1 - \nu^2)}} \tag{4.5}$$

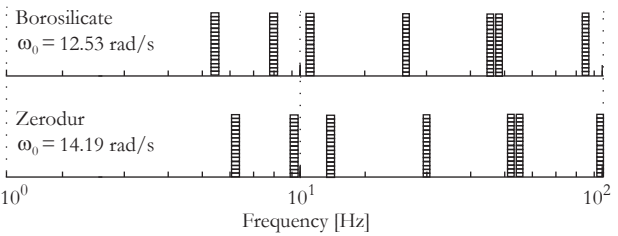

Figure 4.2: Low-order eigenmodes of a faceplate made of either Borosilicate or Zerodur showing the versatility by of the dimensionless modal analysis approach. Once the α_k:s are computed for the given structure, it is easy to compare materials choices from their ω_0:s.

where ω_0 depends only on the material properties and the size of the faceplate. The eigenfrequencies of a mirror are proportional to ω_0. The set of α_k:s for the case study described in Sec. 1.1.1 is plotted in Fig. 4.1, and are obtained by Eq. 2.8–2.10 for the coefficients with the boundary conditions given by Eq. 2.3–2.4. It is noticeable that for the first hundred eigenfrequencies there is nearly a linear relationship between the eigenmode number and α_k^2.

Useful analysis can be made once the α_k:s in Eq. 4.4 are computed. In Fig. 4.2, results from a study of the influence of material choice is shown for a given structure. The first few eigenmodes of a faceplate are computed for the materials Borosilicate and Zerodur®, with an ω_0 of 12.53 rad/s and 14.19 rad/s, respectively.

4.2 Deformable Mirror Size

The size of a faceplate affects its dynamical behavior, and the two main implications are given here:

1. The acoustic frequency, given by Eq. 3.4, scales with the square of the faceplate size. Thus, the start of the smooth part of the transfer function (from force to position) is shifted towards lower frequencies when the size of the faceplate is increased.

2. The eigenfrequencies of the low-order eigenmodes, given by Eg. 4.5, scale with the square of the faceplate diameter reducing the eigenfrequencies by a factor of four, when the faceplate size is doubled.

The two effects have the same origin, namely that the eigenfrequencies scale with r_{out}^{-2}. The first effect relaxes the requirements for the actuators from the faceplate controller, since a low limit frequency of the acoustic region decreases the required bandwidth of

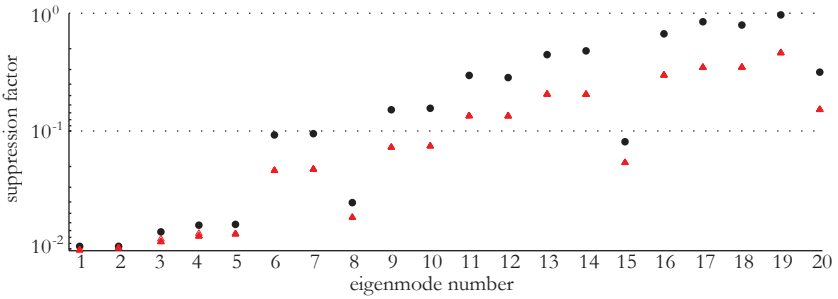

Figure 4.3: The plot shows the suppression factor $\mathcal{Q}_{21}$, defined in Sec. 3.3, for the 20 first eigenmodes. The circles correspond to a relative actuator pitch of 0.09 and the triangles to a relative actuator pitch of 0.045.

the rate feedback loop. Also, increasing the size of the faceplate, decreases the necessary actuator bandwidth, which is attractive from the point of view of actuator design. However the situation is different for the second effect. Shifting more eigenmodes into the bandwidth of the AO system, increases the complexity of the DM-controller.

An increasing number of eigenmodes within the AO bandwidth is a problem, especially when back sensors with roll-off below 20 Hz are used. Thus, the faceplate controller cannot rely on feedback information but instead feedforward control ensures that the eigenmodes are only weakly excited in that range. To evaluate how actuator family performance (the feedforward concept) is affected by the size of the faceplate, the suppression factor, $\mathcal{Q}_{21}$, (see Sec. 3.3) is calculated analytically using the modal participation factors defined in Eq. 2.23. As illustrated in Fig. 3.5, the number of eigenmodes suppressed are in principle approximately equal to half the number of degrees of freedom in the families. However, this statement is only partially true, because the area that the family occupies also affects the suppression. The family size effect is evaluated by defining the relative actuator pitch as a dimensionless parameter

$$d_{\text{pitch}}/r_{\text{out}} \tag{4.6}$$

where the actuator pitch is divided by the radius of the circular faceplate. The size effect is shown in Fig. 4.3, depicting the suppression factor as a function of the mode number. Both the circles and the triangles represent an actuator family encompassing 21 actuators. However, the relative actuator pitch is 0.09 for the circles and 0.045 for the triangles. The curves show that if the relative actuator pitch is decreased (for instance by increasing the size of the faceplate while the actuator pitch remains the same) more eigenmodes are attenuated.

The effect seen in Fig. 4.3 can be explained from a nodal perspective, by letting the relative actuator pitch go towards zero (for instance by increasing the size of the mirror), effec-

tively making the actuator family appear as a single point. This would make the family of force actuators appear as a position actuator.

Chapter 5

Future Work: A Laboratory Experiment

It is desirable to demonstrate experimentally that the developed control approach works as intended. Plans for an experiment based upon components available at the Department of Astronomy and Theoretical Physics have been set up and studied by modeling.. The optical setup presented in the next section, allows only an area of 0.1 m^2 or 13% of a 1 m faceplate to be illuminated and the corresponding reflected, collimated light to be imaged. Even so, it is planned to use a large faceplate with a diameter of 1 m. There are several reasons for choosing a faceplate that is larger than the collimated light-beam:

- A large continuous faceplate mirror places less constraints on the required actuator bandwidth. At sufficiently high frequencies, it is no longer possible to discern individual resonance or anti-resonance peaks because many different modes overlap above the acoustic frequency limit (see Eq. 3.4).
- A large continuous faceplate mirror has more eigenfrequencies below 20 Hz, where the sensitivity of the back sensors is low, than a small faceplate. It is of interest to demonstrate that these eigenmodes are only weakly excited when using the family concept.
- A large faceplate is more representative of a large deformable mirror adding credibility to the experimental validation.

In the experiment, the actuators and sensors will be located in a topology similar to the one shown in Fig. 1.2. The illuminated part of the faceplate has real force actuators and

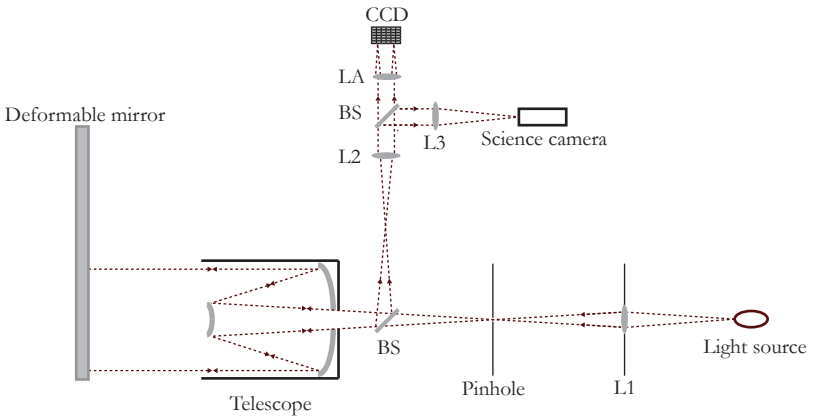

Figure 5.1: The optical setup of a laboratory experiment, which is based upon the Celestron C14 telescope and the SciMeasure's LJ CCD39 detector. The telescope both illuminates and images collimated light reflected from the active part of the deformable mirror. L1-L3 are lenses, BSs beam splitters, and LA a lenslet array.

the dark part has dummy actuators. The dummy actuators (aluminum rods) add the same stiffness as the force actuators to the faceplate near the cross-over frequency of the deformable mirror.

The optical setup of the planned experiment is presented in Sec. 5.1. In Sec. 5.2, results are shown to demonstrate that the partly illuminated faceplate is controllable.

5.1 Optical Setup

The layout of the proposed laboratory experiment is shown in Fig. 5.1. The setup has three optical arms; the light source arm, the science arm, and the wavefront sensor arm. Also, the setup has been made taking into account the available components; the Celestron C14 telescope, and the SciMeasure's LJ CCD39 detector. The first object in the optical train, after the light source, is a lens that converges the light onto the pinhole. The size of the pinhole should be chosen such that the secondary mirror of the telescope is fully illuminated. Since the pinhole is placed in the focal plane of the telescope, the exit beam from the telescope will be collimated and will illuminate part of the faceplate. It will then be reflected back to the telescope and will be taken to the science and wavefront sensor arms via a beam splitter. A collimating lens, marked as L2 in Fig. 5.1, is placed after the focus of the telescope. The distance between the focal plane of the telescope and the lens is chosen such that the collimated beam illuminates the desired number of lenslets of the

Shack-Hartmann wavefront sensor. The second beam splitter in the setup directs light into the wavefront sensor and the science arms. The full width at half maximum size of the spots in the focal plane of the lenslets should cover two pixels on the CCD to achieve good sensitivity.

5.1.1 Light Source Arm

The main component in the light source arm is the Celestron C14 Schmidt-Cassegrain telescope with specifications shown in Table 5.1. The secondary mirror of the telescope is illuminated by the diffracted light from the pinhole, and the size of the pinhole should be

$$D_{\mathrm{PH}} = 2.44\lambda \frac{f_{\mathrm{tel}}}{D_{\mathrm{tel}}} \tag{5.1}$$

so that the first minimum of the Airy's disc aligns with the edge of the secondary mirror of the telescope. That is, for a wavelength of 500 nm. the pinhole size should be 14 μm.

5.1.2 Wavefront Sensor and Science Arm

The format of the SciMeasure's LJ CCD39 detector is 80×80 pixels with a pixel size of $\Delta_{\mathrm{pix}} = 24\,\mu$m. The wavefront sensor is of Shack-Hartmann type with a lenslet array that should be chosen to match the desired number of actuators and the size of the detector. The actuator pitch should be 45–50 mm, corresponding to 7 actuators across the telescope diameter. This leaves 10×10 pixels per subimage. The diameter of each of the lenslets should then be

$$D_{\mathrm{LL}} = 10\Delta_{\mathrm{pix}} \tag{5.2}$$

which is 240 μm. The focal length of the lenslets should be chosen to provide adequate sensitivity for sensing small actuator pokes. To achieve this, the diffraction limited spot

Parameter	*Value*
Focal ratio	F/11.2
Aperture	356 mm
Diameter primary mirror	362 mm
Focal length, f_{tel}	3987 mm

Table 5.1: Optical specification for the Celestron C14.

should cover four pixels on the CCD, given by

$$f_{\mathrm{LL}} \approx 2\frac{\Delta_{\mathrm{pix}} D_{\mathrm{LL}}}{\lambda} \tag{5.3}$$

which gives a focal length of about 23 mm for the wavelength 500 nm. The focal length of the lenslets also defines the dynamic range, i.e. the maximum allowed stroke difference between two adjacent actuators. The maximum detectable gradient of the wavefront measured over a lenslet is

$$\alpha_{\mathrm{LL}} = 10\frac{\Delta_{\mathrm{pix}}}{f_{\mathrm{LL}}} \approx 0.01. \tag{5.4}$$

The scaling of the gradient magnitude from the lenslet array to the telescope is given by

$$\alpha_{\mathrm{tel}} = \alpha_{\mathrm{LL}}\frac{f_{\mathrm{L2}}}{f_{\mathrm{tel}}} \approx 5 \times 10^{-5} \approx 10'' \tag{5.5}$$

where f_{L2} is the focal length of the collimating lens L2. Thus, the maximum allowed stroke difference can be approximated as

$$\delta_{\mathrm{stroke}} = \frac{d_{\mathrm{pitch}}}{2}\frac{D_{\mathrm{LL}} f_{\mathrm{L2}}}{f_{\mathrm{LL}} f_{\mathrm{tel}}} \tag{5.6}$$

where d_{pitch} is the actuator pitch. With an actuator pitch of 50 mm, the maximum allowed stroke difference is 1.3 μm.

In Table 5.2, the lens components for the proposed experiment are listed. The nomenclature for the components is defined in the caption of Fig. 5.1.

5.2 Integrated Model

For reasons of cost, the planned experiment will have many passive dummy actuators. An integrated model, including adaptive optics, has been set up to study whether use of

Nomenclature	*Lens*
LA	Adaptive Optics Associates (250-18-s)
L1	Back to back achromatic lens
L2	Achromatic lens 2 mm diameter and 20 mm EFL
BS	50/50 Beam splitter

Table 5.2: Optical components for the planned experiment (see Fig. 5.1 for nomenclature).

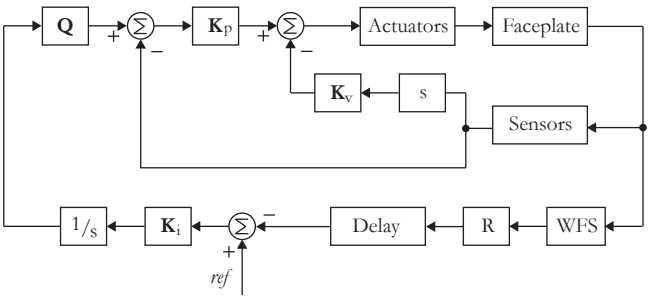

Figure 5.2: Block diagram of the integrated model used to evaluate the experiment setup. The blocks "Actuators", "Faceplate", "Sensors", and "Delay" refer to state-space models on ABC-form.

passive dummy actuators instead of active real actuators is admissible.The architecture of the full integrated model is shown in the block diagram in Fig. 5.2. Three feedback loops are applied; rate and position feedback loops, which control the faceplate, and the outer wavefront sensor feedback loop. The blocks marked with "Actuator", "Faceplate", "Sensors", and "Delay" correspond to state-space submodels on ABC-form describing dynamical behavior.

5.2.1 Adaptive Optics Modeling

The model of the AO loop has five blocks; wavefront sensor, reconstructor, delay, control gain, and integrator. The wavefront sensor, shown as the WFS-block in Fig. 5.2, is modeled by a matrix multiplication for determination of tip and tilt over each subaperture. Modeling of a Shack-Hartmann wavefront sensor can be made in numerous way with different degree of complexity [21]. Here, a simple approach is taken which ignores noise in the wavefront sensor. The principle of the Shack-Hartmann wavefront sensor is shown in Fig. 5.3. The x-displacement in the image plane of the light passing through a subaperture is $f_{\mathrm{LL}}\mathrm{d}W/\mathrm{d}x$, where f_{LL} is the focal length of the lenslet and W the continuous wavefront at the lenslet array. Thus, the center-of-gravity, x_{cog}, in the image plane

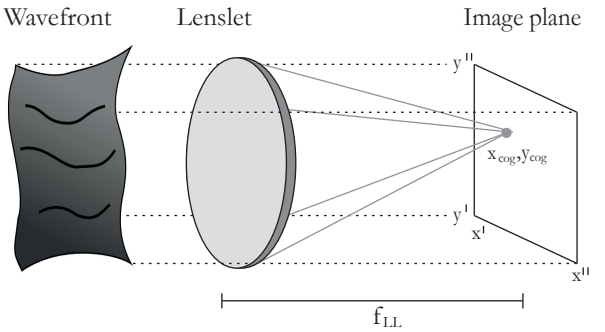

Figure 5.3: The part of the wavefront that covers the lenslet is focused as a point source image in the focal plane of the lenslet. The tip/tilt of each subaperture is computed from the location of the image relative to that of of a plane wavefront.

in the x-direction is determined by

$$\begin{aligned} x_{\text{cog}} &= \frac{1}{A_{\text{LL}}} \int_{y'}^{y''} \int_{x'}^{x''} f_{\text{LL}} \frac{\mathrm{d}W}{\mathrm{d}x} \mathrm{d}x\mathrm{d}y \\ &= \frac{1}{A_{\text{LL}}} \int_{y'}^{y''} \int_{W(y')}^{W(y'')} \mathrm{d}x\mathrm{d}y \\ &= \frac{1}{A_{\text{LL}}} \int_{y'}^{y''} \big(W(y'') - W(y')\big)\, \mathrm{d}y \\ &\approx \frac{1}{A_{\text{LL}}} \sum_{x=x'}^{x''} \left(w_x(y'') - w_x(y')\right) \end{aligned} \tag{5.7}$$

where A_{LL} is the area of the lenslet, and $w_x(y'')$ and $w_x(y')$ the sampled wavefront at the edge of the subaperture. Thus, it is sufficient to know the wavefront phase in the corners of the subapertures to compute the tip/tilt values over each lenslet. This results in a very sparse WFS-matrix.

The reconstructor matrix, **R**, is constructed by a singular value decomposition and inversion of the interaction matrix, i.e. the matrix which describes the tip and tilt over the subapertures when poking each actuator individually.

The time phase lag of the AO loop is represented by the delay-block. The time phase lag is caused by wavefront sensor sampling, data acquisition and computation time. The delay is modeled as a state-space model of a fifth order Padé approximation of $e^{-s\tau}$, where τ is the sampling time of the wavefront sensor.

5.2.2 Simulation Results

The optical setup presented in Fig. 5.1 has a faceplate which is illuminated over about 10% of its total area. It is the same part which the wavefront sensor covers. A faceplate with actuators with an actuator pitch of 50 mm and a Cartesian topology would encompass 353 actuators. However, the illuminated part covers only 45 actuator locations. Thus, the task is to create a concept where the 45 controlled actuators perceive their environment as if all actuators were in operation.

The stiffness constant, k, of each actuator is $5 \times 10^5\,\mathrm{Nm}^{-1}$ near the DM cut-off frequency. The same stiffness can be achieved by a thin rod of aluminum glued to the back of the mirror. From simple solid mechanics, the diameter, d_r and length, l_r, of the rod are related by

$$k = E\frac{\pi d_\mathrm{r}^2}{4l_\mathrm{r}} \tag{5.8}$$

$$\frac{l_\mathrm{r}}{d_\mathrm{r}^2} \approx 10^5\,\mathrm{m}^{-1} \tag{5.9}$$

An aluminum rod, with the dimensions determined by the above equation, can be viewed as a zero-seeking actuator in our setup. However, the aluminum rod cannot mimic the rate feedback loop.

Evaluation of the proposed partly illuminated faceplate experiment is done by comparing it to an experiment with a fully illuminated faceplate populated with only real actuators. The result is shown in Fig. 5.4, where five pairs of transfer functions from force to position for a representative actuator are plotted.

1. *Faceplate alone:* The dynamic behavior of the faceplate alone is shown, which obviously is the same for both experiments. A number of eigenmodes is seen within the desired bandwidth of the AO system.

2. *Rate feedback for one actuator:* The rate feedback loop is closed for the representative actuator. Resonances above 20 Hz are largely suppressed but anti-resonances are still present. In the region 0–20 Hz, where the sensitivity of the back sensors is low, limited damping is added.

3. *All rate loops closed:* The rate feedback loop is closed for all the "real" actuators, that is the 353 and 45 actuators, respectively. For the fully illuminated faceplate case, it can be seen that there is a large magnitude shift (note the change of the magnitude axis scale). There is an over-damping of about 60 dB when closing all rate feedback loops with the gain needed for a single rate feedback loop. This suggests that 353 actuators are not needed to suppress the anti-resonances, which is also apparent from the plot for the partly illuminated case. Over-damping is not present with 45 actuators, and almost all anti-resonances above 20 Hz are suppressed.

4. *Rate and position loops closed:* The position feedback loops are closed for all "real" actuators, and the dummy actuators add similar stiffness. The family matrix is also included for local feedforward control. With the family concept, low-order eigenmodes are not excited and are therefore not visible in the frequency responses, thus the resonances and anti-resonances still present with the rate feedback loops closed will not be excited by an actuation. The signals from the back sensors roll off with 20 dB/decade below 20 Hz.

5. *Rate, position and wavefront sensor loops closed:* The AO feedback loop is closed. The frequency response is similar for both cases, and the cut-off frequency is largely determined by the sampling frequency of the AO loop, represented by the delay-block in Fig. 5.2.

The results demonstrate that a faceplate that is partly illuminated and partly populated with actuators can be controlled with the scheme foreseen. The 45 active actuators perceive their environment as if all actuators were in operation. The planned experiment will therefore be adequate for validation of the control principles before a costly full prototype is built. In particular, the properties of the family concept can be validated. The experiment also provides a good test of the mechanical parts, the actuators and back sensors.

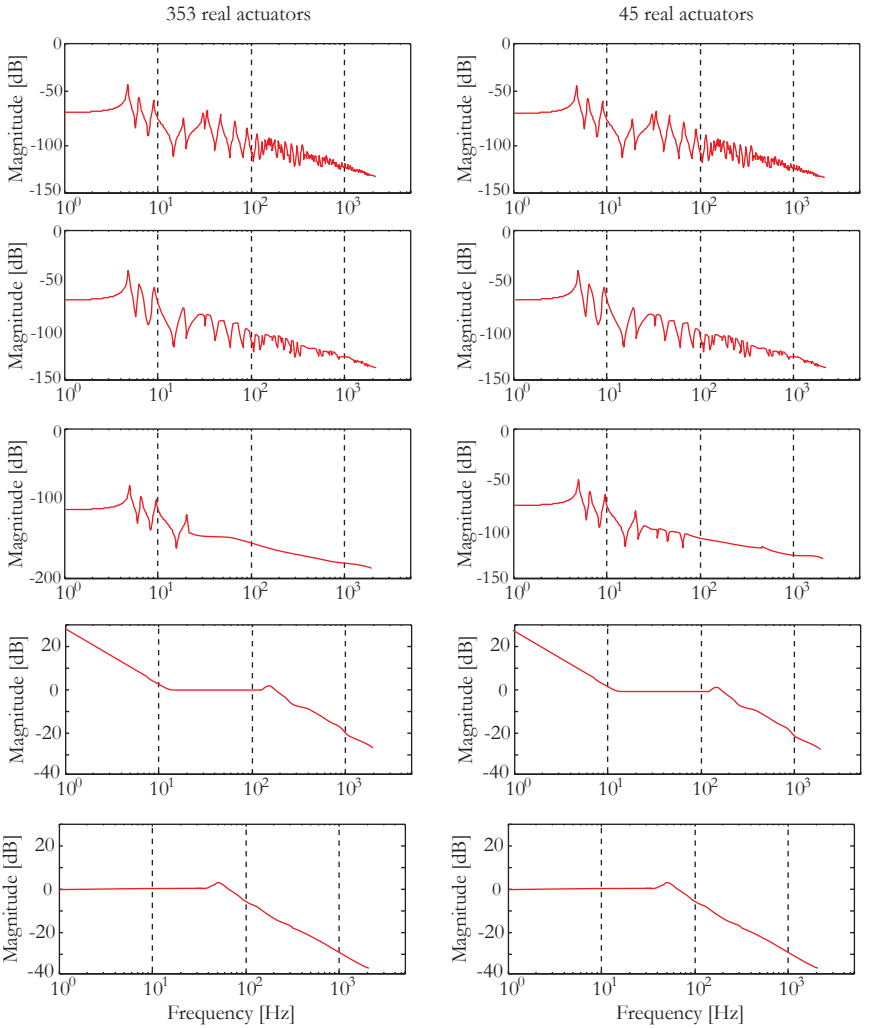

Figure 5.4: A comparison of transfer functions, from force to position at a representative actuator location, between experiments with a fully illuminated faceplate and a partly illuminated faceplate. The five couples of transfer functions describe the cases (from top to bottom): Faceplate dynamics, faceplate with the rate feedback loop closed for the representative actuator, faceplate with all the rate feedback loop closed, faceplate with rate and position feedback loops closed, and faceplate with rate, position and AO feedback loops closed.

Chapter 6

Summary

The overall objective of this project was to study feasibility of a low-cost, large deformable mirror concept. It has been demonstrated that inexpensive electro-mechanical components, such as force actuators and electret microphones can be used. In an adaptive optics system, the proposed deformable mirror will be perceived as an ideal deformable mirror up to a bandwidth of some 150 Hz.

During the project, some interesting results have been found. Among others, it is expected that the following results will be useful outside the research field of the thesis:

- An innovative robust local control concept that utilizes small families of actuators has been set up. The relative distribution between forces in a family of actuators can be computed from a least squares approach

  $$J = ||\mathbf{K}^{-1}\mathbf{f} - \boldsymbol{\xi}||_2.$$

  and can be viewed as extending the Saint-Venant's principle beyond the static case. It is believed that this concept for suppression of low-order eigenmodes and reduction of crosstalk between adjacent actuators can be used in other areas than deformable mirrors, when dealing with MIMO systems of high order (an example is given in [29] for segmented space telescopes). The least squares approximation can in principle be made at any frequency of interest.

- The analytical dimensionless modal analysis of a faceplate can be used to optimize the choice of physical and material parameters also for large deformable mirrors with other types of actuators. The fact that the α_k:s, defined as

  $$\alpha_k^4 = \frac{r_{\text{out}}^4 \omega_k^2 \rho h}{D}$$

remain the same for a given structure geometry is useful when investigating how eigenfrequencies depend on material parameters. This result also applies to other areas involving plate vibrations.

- A sound knowledge of the dynamical behavior of faceplates has been established. Transition between a frequency region which is dominated by resonances and anti-resonances and a smooth frequency region (the acoustic region) is well understood and documented. An understanding of the dynamics of thin-plates can be exploited to develop less expensive and better control systems, including actuators and sensors.

Plans for a laboratory demonstration have been set up and calculations with an integrated model have shown that the laboratory setup is satisfactory.

Chapter 7

The Papers

This chapter provides a brief description of the four papers on which this thesis is based. In addition to describing the paper content, I describe my contribution to each of the papers, both in doing the research, the analysis and in writing the papers.

Paper I: Distributed Force Control of Deformable Mirrors.

D. G. MacMynowski, **R. Heimsten**, T. Andersen
European Journal of Control, Vol. 17, 2011

In Paper I a low-cost, large deformable mirror concept was presented with inexpensive force actuators and electret microphones. It was studied using the finite element method to achieve a modal analysis of the faceplate. A control strategy was developed, which encompasses rate and position feedback. In addition, a local controller including actuator families was introduced to reduce the crosstalk between adjacent actuators. Bending wave theory was used to understand the dynamic behavior of a faceplate. The required bandwidth for a stable rate feedback loop was computed for force actuators. Also, we demonstrated that the phase lag for non-collocated sensors is not a obstacle.

The plate model, control model, and most of the analysis work, was performed by me. Douglas MacMynowski did the main work on the "Wave and impedance considerations" and the "Robustness" sections of the paper. However, I modeled the data used to perform the robustness analysis. The text was written in collaboration between the three authors. Douglas MacMynowski mainly wrote Chapter 3 and 4, while I was focusing on the other Chapters with support from Torben Andersen.

Paper II: Suppressing Low-Order Eigenmodes with Local Control for Deformable Mirrors.

R. Heimsten, M. Owner-Petersen, T. Ruppel, D. G. MacMynowski, T. Andersen
Accepted for publication in Optical Engineering, 2011

In Paper II we presented an analytical theory for the dynamic behavior of faceplates. The analytical model is a valuable tool, which for instance can be used to perform an actuator pitch study. Also, the theory was used to evaluate the characteristics of the actuator family concept by computing modal participation factors. The attenuation of low-order eigenmodes are evaluated against the size of the faceplate. Further, a dimensionless modal analysis was performed to determine how the eigenfrequencies of a faceplate are affected by the physical parameters.

The majority of the work was carried out by me. Input from Thomas Ruppel at the early stage of the project was very helpful for the development of the analytical model. Mette Owner-Petersen contributed to the dimensionless modal analysis, and overall for equations for the modal participation factor. The final analysis was carried out by me, Torben Andersen and Mette Owner-Petersen. All of the text was written by me with the co-authors as advisors.

Paper III: Concept, Modeling and Performance Prediction of a Low-Cost, Large Deformable Mirror.

R. Heimsten, D. G. MacMynowski, T. Andersen, M. Owner-Petersen
Submitted to Applied Optics, 2011

A full model of the low-cost, large deformable mirror concept was presented, including the dynamics of the force actuators and the back sensors. We demonstrated that all the eigenmodes of the deformable mirror are controllable up to a certain bandwidth. We also compared our deformable mirror concept to an idealized deformable mirror. The performance analysis showed that the two deformable mirrors are comparable inside an adaptive optics system up to a bandwidth of some 150 Hz. We analyzed the predicted Strehl ratio in both the temporal and the frequency domains, showing that the low-cost mirror strategy is feasible.

The bulk of the control system work was carried out by me, Douglas MacMynowski, and Torben Andersen. The full integrated model was done by me, with helpful inputs from Torben Andersen and Mette Owner-Petersen. The analysis of the deformable mirror subjected to atmospherical turbulence within an adaptive optics system was performed by me and Mette Owner-Petersen. The text was written by me with the co-authors as advisors.

Paper IV: Integrated Modeling of a Laboratory Setup for a Large Deformable Mirror.

R. Heimsten, T. Andersen, M Owner-Petersen, D. G. MacMynowski
Proc. SPIE IMC11, 2011

In Paper IV we continued the work of the deformable mirror concept. We proposed a first laboratory experiment, which encompasses a partly illuminated large aluminum faceplate. The experimental laboratory setup with a limited amount of force actuators embedded with dummy actuators was modeled to identify the possibilities of the setup. The experiment can be used to evaluate features, such as local control performance, dynamic range, and controllability and robustness of the deformable mirror.

The proposed laboratory experimental setup was developed by me, with advise from Mette Owner-Petersen and Torben Andersen. The model work was carried out by me with inputs from Douglas MacMynowski. The text was written by me with the co-authors as advisors.

Popular Summary in Swedish

För drygt två år sedan, 2009, firades minnet av att Galileo Galilei för 400 år sedan riktat ett telskop mot objekt på himmeln. Allt sedan dess har teleskopet varit det det viktigaste instrumentet för astronomer och med dess hjälp har vår kunskap om universum revolutionerats. I takt med att teleskopet utvecklats har ljussvagare objekt kunnat studeras i högre detalj. Möjligheten att studera ljussvagare objekt möjliggörs av att en fördubbling av den ljusinsamlande spegeln/linsen samlar in fyra gånger så mycket ljus. Att studera objekt i större detalj möjliggörs (idealt) av att upplösningsförmågan är proportionell mot diametern på den ljusinsamlande spegeln/linsen, d.v.s. om spegeln fördubblas kan detaljer som är hälften så stora urskiljas.

8.1 Extremt stora teleskop

Teleskop kan ses som instrument för att hjälpa astronomer att studera universum. En rad olika teleskop finns dels på jorden och dels i rymden, de flesta med unika egenskaper. Ett teleskop kan t.ex. byggas för ett specifikt uppdrag eller ett speciellt våglängdsområde. I det synliga och nära infraröda våglängsområdet finns idag ett antal teleskop med huvudspegelar med en diameter på omkring 8-10 m. Keck och Gran Telescopio Canarias är exempel på teleskop som har segmenterade huvudspeglar, medan VLT, Subaru och Gemini är teleskop som har en stor huvudspegel.

Framtidens landbaserade teleskop för det synliga och nära infraröda området, med huvudspeglar som är tre till fyra gånger större än existerande, planeras idag och går under namnet "Extremely Large Telescopes" eller Extremt stora teleskop. Det finns tre projekt som ligger långt fram i sina planeringsstadium: European Extremely Large Telescope (E-ELT), Giant Magellan Telescope (GMT) och Thirty Meter Telescope (TMT). E-ELT och TMT har en liknande segmenterad huvudspegeldesign, med ett stort antal spegelsegment med en diameter på omkring 1.5 m. Den stora skillnaden mellan dessa två projekt är att TMT har en 3-spegel design medan E-ELT har en 5-spegel design.

8.2 Adaptiv optik

År 1704 påpekade Newton i verket Opticks att det "... finns begränsningar, bortom vilket ett teleskop inte kan verka" vilket beror på att "... luften genom vilken vi skådar stjärnorna, är i evig skakning". Newtons påpekande är korrekt, atmosfärens ständiga rörelse begränsar detaljrikedomen. Turbulensen i atmosfären genererar luftbubblor med olika temperatur och täthet. Effekten från dessa små bubblor kan liknas vid att ljuset passerar svaga men många olika linser. Att en stjärna blinkar, vilket kan ses med blotta ögat, är en effekt av atmosfärens turbulens. Från ett teleskopperspektiv kan atmosfärens påverkan liknas vid ett fotografi där objektet varit i rörelse, en suddig bild som det är svårt att urskilja detaljer i.

Fram till slutet av förra århundradet var atmosfärens turbulens en begränsning gällande detaljrikedom. Större teleskop byggdes och samlade in mer ljus, men upplösningsförmågan förblev den samma som de teleskop som användes under Newtons tid. På 1990-talet började en teknik kallad adaptiv optik att integreras i teleskop. Dessa system inkluderar en vågfrontsensor, en eller flera deformerbara speglar och ett kontrollsystem. Vågfrontsensorn är den del som observerar hur ljuset från en stjärna har ändrats på sin färd genom atmosfären. Informationen om felet skickas till kontrollsystemet som skickar kommandon till den deformerbara spegeln, vilken böjer sig därefter. Slutresultatet blir att ljuset som reflekteras av den deformerbara spegeln inte längre innehåller effekterna från den turbulenta atmosfären. Det adaptiva optiska systemet måste köras i realtid och uppdateras flera hundra gånger per sekund för att följa utveckligen av atmosfärens rörelse.

8.3 Stora deformerbara speglar

Deformerbara speglar som används i teleskop är förhållandevis små med en diameter på 10-30 cm, med undantag av ett fåtal. Den största deformerbara spegeln som är integrerad i ett teleskop idag, har en diameter på 911 mm och återfinns i Large Binocular Telescope. I designen för E-ELT har en deformerbar spegel med en diameter på dryga 2 m inkluderats och GMT har ett antal stora deformerbara speglar som den sekundära spegeln i sin design. Behovet av forskning inom detta område är därav uppenbart.

Den drivande kraften bakom stora deformerbara speglar är framförallt möjligheten att integrera spegeln i teleskopsdesignen och inte behöva använda extra optiska element. Detta argument är viktigt eftersom en del av det insamlade ljuset försvinner vid varje spegelreflektion. Effekten av att använda en stor deformerbar spegel, integrerad i teleskopsdesignen, blir alltså att mer av det insamlade ljuset når fram till forskningsinstrumenten.

I denna avhandling presenteras arbetet med att ta fram ett koncept för en stor deformerbar spegel, vilket designmässigt är en sann teknisk utmaning. Fokus ligger inte enbart på att

demonstrera ett fungerade spegelkoncept, utan också visa ett kostnadseffektivt alternativ. Det relativt billiga spegelkonceptet möjliggörs av att de mekaniska komponenterna är "okonventionella". Kraftaktuatorerna, som används för att deformera spegeln, sätts fast på baksidan av den deformerbara spegeln genom att vakuumtryck skapas i sugkoppar. Användningen av sugkoppar gör att extra komponenter på baksidan, t.ex. magneter, inte behövs. Detta reducerar kravet på den mekaniska toleransen, vilken är kostsam.

En tunn spegel som styrs av kraftaktuatorer har en mjuk struktur, d.v.s. spegeln vibrerar lätt och vibrationer blir långvariga. Dessutom är olika spegelformer svåra att uppnå, eftersom ett fåtal former är kraftigt dominerande. En jämförelse kan göras med ett papper; om ett pappersark hålls i mitten med ena handen medan den andra handen trycker på ett ställe, blir följden att hela pappersarket viker sig. För att motverka detta beteende hos strukturen har ett kontrollsystem tagits fram för att styra den deformerbara spegeln.

Att designa ett kontrollsystem är en utmaning eftersom en deformerbar spegel har en stor mängd aktuatorer och sensorer, kan vara flera tusen. En lokal styrning har föreslagits, vilken gör systemet hanterbart. Istället för att styra varje aktuator individuellt, styrs små familjer av närliggande aktuatorer tillsammans. Energin som tillförs spegeln genom en aktuator sprids inte utanför familjen. Aktuatorfamiljen har bra egenskaper som utnyttjas i kontrollsystemet och konceptet ger också god stabilitet och robusthet.

För att kunna designa en deformerbar spegel, är det viktigt att förstå de dynamiska egenskaperna hos en tunn spegel. Två olika betraktelsesätt har presenterats. Ett alternativ är att betrakta en spegels rörelse som vågor på vatten. Vågor kan reflekteras av kanterna och bilda stående vågor, vilket definerar vibrationsmoderna i en spegel. Alltså kan vågteori användas för att beskriva en spegels dynamiska beteende. Ett alternativt sätt är att betrakta en spegels rörelse utifån de ekvationer som beskriver dess utböjning. Dessa ekvationer är komplexa att lösa men det är dock möjligt. Det underlättar att betrakta en spegels utböjning som en kombination av vibrationsmoder. Ett verktyg för att lösa ekvationerna har presenterats, vilket även är användbart inom andra områden.

Det är värt att nämna att det deformerbara spegelkonceptet som presenteras i denna avhandlig uppfattas som en "konventionell" deformerbar spegel i ett adaptivt optiskt system. De simuleringar av modellen som gjorts, visar att det framtagna spegelkonceptet fungerar lika bra som en idealiserad deformerbar spegel i de driftområden som adaptiva optiska system vanligtvis har.

Slutligen, har planer för ett första experiment beskrivits och en integrerad model har används för att bekräfta experimentets möjligheter att demonstrera det framtagna konceptet för en deformerbar spegel.

Appendix A: Notation

A	Faceplate area
$\mathbf{A}$	System matrix
$\mathbf{B}$	Input matrix
c	Modal participation factor
c_g	Group velocity for bending waves
c_p	Phase velocity for bending waves
$\mathbf{C}$	Output matrix
$\boldsymbol{\mathcal{C}}$	Compliance matrix
d_{pitch}	Actuator pitch
D	Flexural rigidity
D_{LL}	Diameter of the lenslets
D_{PM}	Diameter of the primary mirror
$\mathbf{D}$	Feedforward matrix
E	Young's modulus
$\mathbf{E}$	Damping matrix
f_{ac}	Acoustic frequency
f_{LL}	Focal length of the lenslets
$\mathbf{f}$	Force vector
h	Thickness of the faceplate

l	Lateral load per unit area
k	Stiffness
$\mathbf{K}$	Stiffness matrix
$\mathbf{K}_a$	Stiffness matrix, which encompasses the actuator nodes
$\mathbf{M}$	Mass matrix
N	Modal density
$\mathbf{q}$	Modal displacement vector
$\mathbf{Q}$	Family matrix
$\mathcal{Q}$	Suppression factor
r_{in}	Radius of the inner rim of the faceplate
r_{out}	Radius of the outer rim of the faceplate
$\mathbf{x}$	Internal state vector
$\mathbf{y}$	System output vector
$\mathbf{u}$	System input vector
w	Deflection with respect to the undeformed reference
W	Eigenmode
α	A dimensionless parameter which remains the same for a given structure
Δ_{pix}	Pixel size
$\Delta\omega$	Average modal spacing
ζ	Modal damping
λ	Wavelength of light
ν	Poisson's ratio
ξ	Dimensionless parameter
$\boldsymbol{\xi}$	A vector holding the displacements
ρ	Density of the faceplate material
$\boldsymbol{\psi}$	Eigenvector
$\boldsymbol{\Psi}$	Eigenvector matrix

$\boldsymbol{\Psi}_m$ Mass normalized eigenvector matrix

ω Angular eigenfrequency

ω_0 A material specific parameter which is used to determine eigenfrequencies

$\boldsymbol{\Omega}$ Diagonal matrix with the angular frequencies as elements

References

[1] H. W. Babcock, "The Possibilty of Compensating Astronomical Seeing," Publ. Astr. Soc. Pac **765** (1953)

[2] J. W. Hardy, J. E. Lefebvre and C. L. Koliopoulos, "Real-time atmospheric compensation," J. Opt. Soc. Am **67** (1977)

[3] T. Andersen, A. Ardeberg and M. Owner-Petersen, *Euro50 - A 50m Adaptive Optics Telescope* Lund Observatory (2003)

[4] A. Riccardi, G. Brusa, P. Salinari, D. Gallieni, R. Biasi, M. Andrighettoni, and H. M. Martin, "Adaptive secondary mirrors for the Large Binocular Telescope," Proc. SPIE **4839** (2002)

[5] S. Esposito, A. Tozzi, A. Puglisi, L. Fini, P. Stefanini, and A. Riccardi, "Development of first light AO system for the Large Binocular Telescope," Proc. SPIE **5169** (2003)

[6] A. Riccardi, M. Xompero, D. Zanotti, L. Busoni, C. Del Vecchio, P. Salinari, P. Ranfagni, G. Brusa Zappellini, R. Biasi, M. Andrighettoni, D. Gallieni, E. Anaclerio, H. M. Martin and M.S. Miller, "The adaptive secondary mirror for Large Binocular Telescope: results of acceptance laboratory test," Proc. SPIE **5169** (2008)

[7] F. Wildi, G. Brusa, M. Lloyd-Hart, L. Close and A. Riccardi, "First light of the 6.5-m MMT adaptive optics system," Proc. SPIE **5169** (2003)

[8] F. Quiros-Pacheco, L. Busoni, G. Aqapito, S. Esposito, E. Pinna, A. Puqlisis and A. Riccardi, "First Light AO (FLAO) system for LBT: performance analysis and optimization," Proc. SPIE **7736** (2010)

[9] B. Crepy, S. Chaillot, J. M. Conan, R. Cousty, C. Delrez, M. Dimmler, J. L. Dournaux, S. De Zotti, E. Gabriel, R. Gasmi, R. Grasser, N. Hubin, P. Jagourel, L. Jochum, F. Locre, P-Y. Madec, P. Morin, M. Mueller, G. Petit, D. Petitgas, M. Pierard, J. J. Roland, J. C. Sinquin and E. Vernet, "Last progress concerning the design of the piezo-stack M4 adaptive unit of the E-ELT," Proc. SPIE **7736** (2010)

[10] B. Crepy, S. Chaillot, M. Cola, J. M. Conan, R. Cousty, M. Dimmler, J. L. Dournaux, S. De Zotti, E. Gabriel, R. Gasmi, R. Grasser, N. Hubin, P. Jagourel, L. Jochum, F. Locre, P-Y. Madec, P. Morin, M. Mueller, G. Petit, D. Petitga, J. J. Roland, J. C. Sinquin and E Vernet, "Demonstration prototype and breadboards of the piezo stack M4 adaptive unit of the E-ELT," Proc. SPIE **7736** (2010)

[11] T. Andersen, O. Garpinger, M. Owner-Petersen, F. Bjoorn, R. Svahn and A. Ardeberg, "Novel concept for large deformable mirrors," Optical Engineering **45** (2006)

[12] A. E. H. Love, "The Small Free Vibrations and Deformation of a Thin Elastic Shell," Phil. Trans. R. Soc. London **179** (1888)

[13] J. N. Reddy, *Theory and Analysis of Elastic Plates and Shells*, Taylor & Francis (2007)

[14] S. P. Timoshenko and S. Woinowsky-Krieger, *Theory of Plates and Shells*, McGraw-Hill International Editions (1959)

[15] E. Ventsel and T. Krauthammer *Thin plates and shells: theory, analysis, and applications*, Marcel Dekker (2001)

[16] T. Ruppel, W. Osten and O. Sawodny, "Model-based feedforward control of large deformable mirrors", European Journal of Control **17** (2011)

[17] W. E. Press, S. A. Teukolsky, W. T. Vetterling and B. P. Flannery, *Numerical Recipes: The art of scientific computation*, Cambridge University Press (2007)

[18] S. Hassani *Mathematical Physics*, Springer-Verlag, New York, (1999)

[19] J. N. Reddy, *An Introduction to the Finite Element Method*, McGraw-Hill (2006)

[20] J. L. Humar, *Dynamics of structures*, Balkema Publishers (2001)

[21] T. Andersen and A. Enmark *Integrated Modeling of Telescopes* Springer-Verlag, New York (2011)

[22] S. H. Chrandall, "The Role of Damping in Vibration Theory", J. of Sound and Vibrations **11** (1970)

[23] B. Friedland, *Control System Design: An Introduction to State-Space Methods*, Dover Publications (2005)

[24] J. Durbin and S J. Koopman, *Time Series Analysis by State Space Methods*, Oxford Univ Press (2001)

[25] A. Enmark, *Adaptive Optics in Integrated Modeling of Telescopes*, Doctoral Thesis, Media-Tryck (2009)

[26] A. Preumont, *Vibration Control of Active Structures: An Introduction*, Kluwer Academic Publishers (2002)

[27] R. H. Lyon and R. G. DeJong, *Theory and application of statistical energy analysis*, Newnes (1995)

[28] R. H. Lyon, *Machinery Noise and Diagnostics*, Butterworth-Heinemann (1987)

[29] D. G. MacMynowski, "Control of a "hyper-segmented" space telescope", Submitted to AIAA J. Guidance, Control and Dynamics (2011)

Acknowledgements

I would like to express my sincere respect and deepest gratitude to my advisors Torben Andersen and Mette Owner-Petersen for all their support throughout the work. A special thanks to Torben Andersen for the time and effort spent on my education as well as scientific work. It has been a truly inspiring and fun time working with you. Thank you for believing in me and giving me the opportunity to work on this project. Last but not least, the Danish Christmas dinners have been joyful events.

I owe my deep gratitude to the coauthors of my manuscripts for their genuine interest, rapid response and skillful comments that greatly contributed to my manuscripts. A special thank goes to Douglas MacMynowski, who has actively participated in this work and kindly provided great help.

I would like the thank the fellow Ph.D. students and colleagues, who provided a special atmosphere at work. Especially thanks to Thomas Lennartsson, with whom I shared office, for all of the discussions about everything under the Sun. Also, you are now in sole control of the heat regulator.

A special thanks to the student priests in Lund who helped me with the journey to find myself and the way of life again in difficult times.

I devote my deepest gratitude to my parents for their unlimited love and support. They have encouraged and helped me in all possible ways throughout the years of my studies.

Paper I

European Journal of Control (2011)3:249–260

DOI:10.3166/EJC.17.249–260

European Journal of Control

Distributed Force Control of Deformable Mirrors

Douglas G. MacMynowski[1], Rikard Heimsten[2,*], Torben Andersen[2]

[1] Control and Dynamical Systems, California Institute of Technology, 1200 E. California Blvd., Pasadena, CA 91125, USA;
[2] Lund Observatory, Lund University, 221 00 Lund, Sweden

Large (>1 m) deformable mirrors are attractive for adaptive optics on ground-based telescopes; the mirrors typically have hundreds or thousands of actuators. The use of force actuators instead of position actuators has the potential to significantly reduce total system cost. However, the use of force actuators results in many lightly-damped structural resonances within the desired bandwidth of the control system. We present a robust control approach for this problem and demonstrate its performance in simulation. First, we demonstrate that high-bandwidth active damping using velocity feedback from mirror sensors that are not quite collocated with the actuators can be robustly implemented, because at sufficiently high frequencies the structural dynamics enter an "acoustic" limit, where the half power bandwidth of a mode exceeds the modal spacing. This is important, because the system can be made less expensive using sensors placed in between actuators rather than collocated with each actuator. Introduction of active damping leads to a much easier problem for subsequent position control. It is known that a position control system in which each of the actuators is controlled using feedback from a collocated sensor can be made robustly stable. However, the resulting performance at high spatial frequencies is poor because there is no shared information between neighbouring actuators. In contrast, global control gives excellent performance but lacks robustness to model uncertainty. We introduce an innovative local control approach, which significantly improves the high spatial frequency performance without the robustness challenges associated with a global control approach. The overall approach is demonstrated to provide excellent command response suitable for an adaptive optics outer loop.

Keywords: Adaptive optics, deformable mirror, distributed control, active damping, local control

1. Introduction

Most modern ground-based telescopes have adaptive optics (AO) for compensation of atmospheric blurring or telescope aberrations. Adaptive optics encompass one or more deformable mirrors (DMs), each with many actuators, to compensate for distortion of the wavefront of the incoming light. So far, most DMs have been small, typically with a diameter of tens of centimeters or less. However, large DMs with a size of 1–4 m are highly attractive for the new generation of Extremely Large Telescopes, because the DMs can then be integrated directly into the optical telescope, avoiding use of post-focus relay optics. The present paper outlines an approach for control of such a large DM.

DMs up to about 1 m exist and larger DMs are planned. Stiff "position" actuators of piezo-electric, electrostrictive or magnetostrictive type have so far successfully been used to deform a DM with a high temporal bandwidth. Because the DM is effectively constrained at the actuator locations, there are no significant problems related to dynamic performance. On the other hand, the use of such actuators is costly due to the tight fabrication tolerances involved. In

*Correspondence to: R. Heimsten, E-mail: rikard@astro.lu.se

Received 30 November 2009; Accepted 30 September 2010
Recommended by C. Kulcsár, H.-F. Raynaud, J.-M. Conan, D.W. Clarke

contrast, a DM with soft force actuators is more difficult to control because the dynamics of the mirror structure enter directly into the control loops. However, DMs with force actuators have the potential for being inexpensive because the mechanical tolerances can be more relaxed. Since the cost of DMs may be dramatic, we have studied approaches for use of low-cost force actuators.

An Italian group has played an important role in the development of large DMs with force actuators, and has set up a control strategy [3, 13] for their systems. Electronic damping is established by differentiating the position feedback from a collocated sensor at the location of the actuator. In addition, a combination of feedforward and position feedback is used to track commands from an external AO control loop. The mirror has a thickness of 1–2 mm and is made of polished Zerodur. A British group has studied an alternative design using composites [5] but has not published a detailed control strategy for force actuators.

For development of a low-cost DM, we have studied a system using force actuators attached to the back of the mirror through suction cups and non-collocated position sensors using electret microphones in rubber bellows touching the back of the mirror [1] much like stethoscopes. The DM itself can also be inexpensively constructed using slumping techniques [1]. Due to the use of inexpensive components and low tolerances, such a system has the potential for being much less expensive than corresponding systems built or proposed until now. However, the system is more complex from a controls point of view because the structural dynamics of the mirror are part of the control loops. Also, to provide sufficient space, the force actuators and position sensors are not collocated as will be shown later. The focus of this paper is on demonstrating a control approach for this problem that gives sufficient command-response bandwidth for use within an AO system.

The control approach in [3, 13] uses single-input-single-output (SISO) feedback from mirror deflection sensors that are collocated with the actuators ("collocated control"). While guaranteed to be robust, feedforward is required to obtain adequate performance at high spatial frequencies, requiring careful calibration. Miller and Grocott [11] present a global control approach for a similar flexible DM, combining several innovations, including the use of a full state-space controller and a circulant approach to reduce the resulting computations. While overcoming the limitations of collocated control, the challenges with this model-based approach are likely to come from robustness; any control that relies on some particular model information has the potential for insufficient robustness to uncertainty in that information. A distributed control approach has also been simulated for a large deformable mirror [6, 4]. This approach leads to a low-computation decentralized approximation to the global optimal control solution, but since it approximates the system as infinite in extent, it does not correctly deal with the boundaries, which can limit the achievable performance.

The approach taken here is to use the minimum information required about the structural dynamics to ensure robustness to modeling uncertainty, while incorporating sufficient information to provide performance, and without relying on accurate calibration. The approach can be divided into two steps. First, active damping using velocity feedback effectively compensates for the lightly-damped structural dynamics. Second, a position control system is added. Due to the active damping, the position control system can be based upon local controllers, in turn providing excellent command response suitable for an outer adaptive optics feedback loop based on wavefront information. Hence, in this paper we present two key innovations. First we show that active damping can be implemented using sensors that are not perfectly collocated, and we compute an explicit bound on the maximum spatial separation that can be tolerated between actuators and sensors, using an acoustic argument. This allows the use of realistic and inexpensive hardware. And second, we present a robust local position control strategy overcoming the high-spatial frequency limitations of collocated position control without introducing the robustness concerns of a model-dependent global feedback strategy; this is similar in spirit to the local estimation strategy in [10].

This control approach is also of potential interest for future space applications. For weight reasons, large spacecraft mirrors must necessarily be thin, calling for a control system to set the correct shape of the mirror during operation in the presence of significant structural dynamics within the control bandwidth.

The next section outlines the control problem in general and a simulation example used throughout to illustrate the approach. The velocity and position feedback concepts are discussed in Sections 3 and 4 respectively.

2. Control Problem

2.1. Problem Characteristics

The objective of the control strategy developed herein is to enable a low-cost concept for a large deformable mirror that uses force actuators attached to the back of the mirror with suction cups. Use of low-cost force actuators in combination with a thin mirror leads to a lightly damped system with structural resonance frequencies within the desired control bandwidth. Feedback from the wavefront sensor in the external adaptive optics loop will not be sufficient to confront the problem with structural resonances. Hence, an additional feedback loop using sensors on the back of the mirror is needed as shown in Fig. 1; the focus of this paper is the design strategy of this feedback loop.

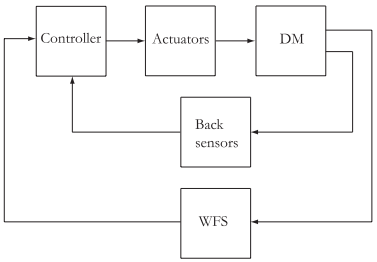

Fig. 1. Schematic of overall control architecture, including inner control loop of a flexible, deformable mirror, and outer adaptive optics control loop using wavefront sensor feedback.

We plan to use electret microphones in bellows at the back of the mirror to sense mirror deflection. For practical reasons, it is not attractive to have the actuators and back sensors precisely collocated. One of the contributions herein is to demonstrate that robust performance does not require this. The impact of finite actuator/sensor bandwidth and delays from discrete-time implementation can be understood in terms of their impact on phase margin. Other practical details regarding actuator/sensor design are discussed in [1]. The prototype actuator in [1] has sufficient force to give a low-spatial frequency amplitude of about 1 mm for the mirror parameters used in the simulations here, and a maximum difference in excursion between two adjacent actuators of about 1.5 μm; this is more than enough for AO.

The requirements on the control algorithm for the DM are determined by the characteristics of the AO system, and are discussed in [1]. The principal requirement is the temporal command bandwidth. In order to allow a typical closed-loop AO bandwidth of roughly 50 Hz, the DM must respond to actuator commands with relatively flat frequency response and at most have a 20–30° phase lag at that frequency. (Note that the AO bandwidth is typically limited by measurement (photon) noise, and not by phase lag.) This requires that the system bandwidth for the DM be higher than the desired AO bandwidth. Herein we evaluate command response accuracy by assuming all spatial frequencies correctable by the DM are equally weighted. The range of correctable spatial frequencies is determined by the number of actuators.

2.2. Simulation Example

The example used throughout this study is a 2 mm thick, 1 m diameter deformable mirror fixed in its center and made of the material borosilicate. Material properties are given in Table 1. The actuator and back sensor locations are shown in Fig. 2. A finite element model of the mirror has been set up using the software package "Comsol Multiphysics" approximating the mirror with a plane shell. The mesh includes about 5000 nodes, of which 1080 are placed at the actuator and back sensor locations. The remaining nodes were automatically generated with the constraint of a maximum node distance of 1.8 cm. Each node has six degrees of freedom (DoF), i.e. translation along three mutually perpendicular axes and rotation around the same axes. The dynamic behavior of the structure is described by the differential equation:

$$\mathbf{M}\frac{\mathrm{d}^2\delta}{\mathrm{d}t^2} + \mathbf{D}\frac{\mathrm{d}\delta}{\mathrm{d}t} + \mathbf{K}\delta = \mathbf{f}$$

where **M**, **D**, **K** are the mass, damping and stiffness matrices, **f** the force vector, and δ is the vector of angular and translation displacements. The lowest eigenfrequency of the structure is 5.6 Hz with another 658 eigenfrequencies almost evenly distributed up to 5000 Hz (consistent with

Table 1. Parameter definitions and values.

Parameter	Definition	Value
E	Young's modulus	63×10^9 Pa
ρ	Density	2.23×10^3 kg/m^3
ν	Poisson ratio	0.2
h	DM thickness	2 mm
I	Moment of inertia	$h^3/12$
D	Bending stiffness	$EI/(1-\nu^2)$
A	DM area	$\pi(0.5\,\mathrm{m})^2$
ζ	Damping ratio	1%

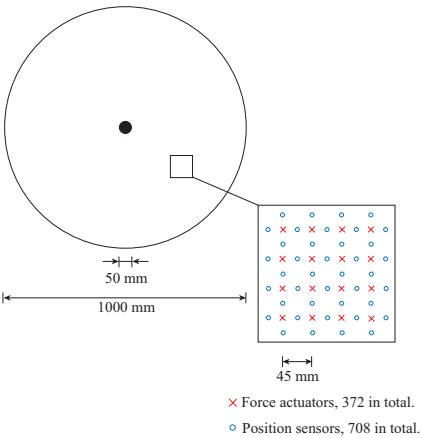

Fig. 2. Topology of distribution of force actuators and position sensors over the back of the 1 m diameter deformable mirror used in the examples.

Eq. (3)). In the general case, there will be four sensors located at the same distance from a given actuator, see Fig. 2. For the purpose of position feedback for the actuator, we apply an average value of the reading of the four sensors. In the following, we will refer to the average of the four sensors, y, as the "sensor" signal for the actuator. Use of this non-collocated sensor and actuator scheme leads to a phase lag between the actual movement of an actuator and the signal from a nearby sensor; this can be estimated from the wave speed.

The full model of the mirror with nearly 30000 DoFs is computationally impractical, so model reduction has been performed as follows:

- First, Guyan reduction was utilized to reduce the number of DoFs to three for each node, retaining out-of-plane translation and the two rotations about the in-plane axes. This reduction is applied to the structure matrices **K** and **M**.
- Next, a further model reduction was performed using modal truncation, removing modes with eigenfrequencies above 5000 Hz. Mode acceleration was applied to include the static contribution from the modes that were omitted by the truncation. The final model is formulated in a structural modal basis.

3. Velocity Control

The purpose of conceptually dividing the feedback into rate ("electronic" or "active" damping) and position control loops is that the latter is more straightforward to design once the former loops are closed. The goal of the rate feedback is to compensate for the lack of damping in the mirror structure. Active damping with collocated and ideal actuators and sensors is straightforward; we here demonstrate that active damping is also possible without perfect collocation, and we quantify the allowable separation. To do so, it is first useful to explore several characteristics of the flexible deformable mirror dynamics. Section 3.1 describes the characteristics of the structural dynamics that enable this velocity control approach and Section 3.2 outlines the rate feedback.

3.1. Wave and Impedance Considerations

For systems with relatively few modes, a modal description is useful. However, with many modes within the control bandwidth, useful intuition can also be obtained with a wave-based description of the structural dynamics. Resonances arise due to constructive interference of waves reflecting off system boundaries. At high frequencies, small variations in the material properties, interaction with actuators, or boundary details will result in significant uncertainty in the structural resonances, making any approach that is reliant on exact knowledge of the resonances non-robust. However, the relevant properties of the mirror near an actuator depend only on the local structure properties, and are much less sensitive to modeling errors.

For the purpose of understanding the dynamics, it is sufficient to model the deformable mirror by an ideal plate. The bending wave (group) speed in the plate at angular temporal frequency ω is

$$c = 2\sqrt[4]{\frac{D}{\rho h}\omega^2} \tag{1}$$

where parameter definitions are given in Table 1. For the properties used in the simulation example, $c = (3.6\,\mathrm{ms}^{-1/2})\sqrt{\omega}$.

The drive-point mobility, i.e. the transfer function from force to velocity at the same location of an infinite plate is [2]:

$$G = \frac{1}{8\sqrt{D\rho h}} \tag{2}$$

This is also the "average" or dereverberated transfer function of a finite plate [9] as evident in the representative transfer function shown in Fig. 3. If the structural damping is sufficiently high, then disturbances propagating towards the boundary of the mirror dissipate. There is no significant reflection, and therefore, except at very low frequencies, the structure response is the same as that of an infinite plate.

A critical feature also evident in Fig. 3 is that with any non-zero damping, then at sufficiently high frequency, the deviation between the response of the lightly damped system and that of the dereverberated or infinite system decreases. The response is no longer dominated by individual modes, but rather at any frequency, there are sufficiently many different modes participating that the transfer function is no longer characterized by sharp resonant and anti-resonant peaks in either the magnitude or phase. The half-power bandwidth of each mode is $2\zeta f_m$, where ζ is the modal damping and f_m the undamped eigenfrequency for the mode. The "acoustic" behavior occurs for frequencies where the half-power bandwidth of a mode exceeds the average modal spacing by a factor of two or three (i.e. 2–3 modes excited at any given frequency). For a plate with area A, the average modal spacing [8] is:

$$\Delta f = \frac{2}{A}\sqrt{\frac{D}{\rho h}} \tag{3}$$

which is roughly 8 Hz for the simulation parameters here. Thus the transition to acoustic behavior begins around

$$f_a \simeq 2\sqrt{\frac{D}{\rho h}}\frac{1}{A\zeta} \tag{4}$$

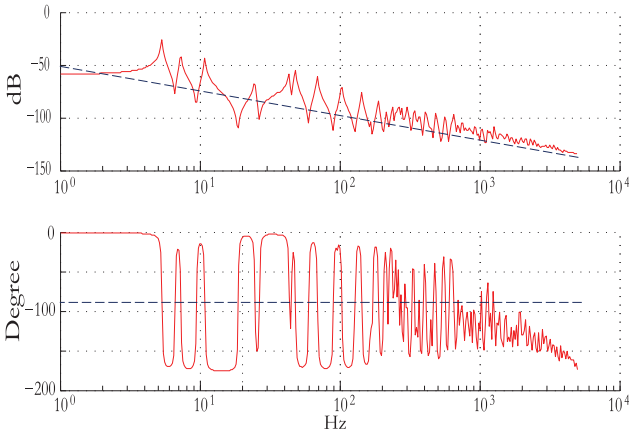

Fig. 3. Representative transfer function from force to position at one actuator for a 1 m mirror, compared to the theoretical infinite plate response (dashed line). See Section 2.2 and Table 1 for simulation parameters. The high frequency decrease in phase relative to the theoretical response is due to sensor non-collocation.

which for the parameters here is ∼800 Hz; above this frequency we should expect to see a smoother transfer function arise (c.f. Fig. 3).

3.2. Active Damping

It is well known that damping can be added using collocated rate feedback (e.g. [12]):

$$u_v = -K_v \dot{y}_a \tag{5}$$

where y_a is the deflection at a given location, K_v is a gain, and u_v is the command to a force actuator collocated with the deflection measurement. The optimal gain is given by the inverse of the dereverberated drive point mobility (the transfer function from force to velocity if the system were completely damped with all "reverberations" removed); this follows from impedance-matching arguments (e.g. [9]). The dereverberated mobility for a plate is the same as the mobility of an infinite plate (Eq. (2)). This feedback is thus positive real and hence stability is guaranteed. However, because both the dereverberated system dynamics and feedback are constant with frequency, the loop transfer function will be of order one at all frequencies. Phase lag due to actuator-sensor non-collocation, actuator/sensor dynamics, or delays from the electronic implementation will result in any real system not being positive real at some sufficiently high frequency. The system will still be stable if there is sufficient damping, see e.g. [12, Fig. 5.15]; for the DM here, the trade-off between damping and actuator-sensor spacing can be explicitly calculated.

Stability can still be guaranteed if the frequency at which positivity breaks down exceeds the acoustic limit described earlier, where the system transfer function is no longer dominated by lightly damped resonances, and the average phase of the force to velocity transfer function is 0°, rather than alternating between ±90°. The reduced phase variability allows roll-off to be introduced into the rate feedback without stability problems so that the feedback is gain-stable at high frequencies; the reduced gain variability also means that relatively little roll-off (and accompanying phase lag) is required for high-frequency gain-stability.

Stable rate feedback can thus be implemented provided there is minimal phase lag below this frequency. This requires a minimum rate feedback bandwidth of the order of the acoustic limit defined in Eq. (4). Note that this limit frequency decreases as the deformable mirror increases in size, hence making larger mirrors easier to control. Non-collocation will introduce phase lag of 45° at an actuator-sensor spacing of d at frequency $f = c/(8d)$, and thus the maximum actuator-sensor distance is of order $d \leq c/(8f_a)$ where c and f_a are from Eqs (1) and (4) respectively. With the parameters used here, this means that if the spacing between the actuators and sensors is no more than about 22 mm (this is the value chosen here; see Fig. 2), then the phase lost to non-collocation is tolerable at frequency f_a. Any additional phase lag due to actuator/sensor bandwidth and implementation delays need to be accounted

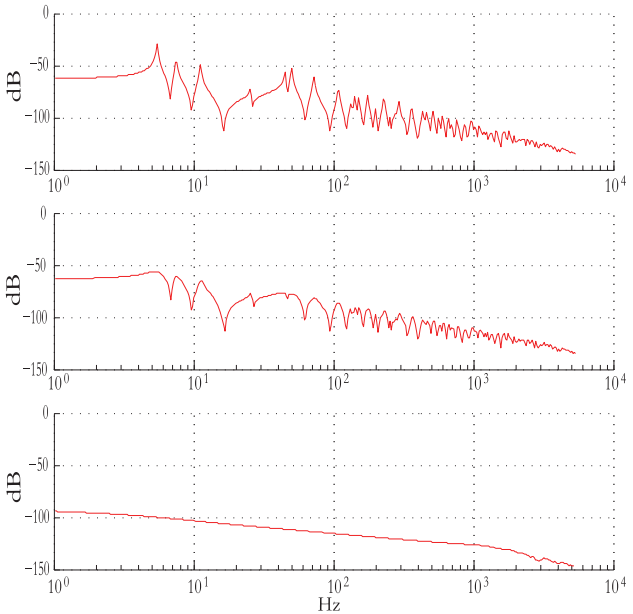

Fig. 4. Performance of rate feedback loop at a representative actuator location (transfer function magnitude from actuator force to sensor position) for (a) open loop, (b) only the collocated loop closed and (c) all loops closed.

for and will reduce the maximum tolerable spacing. Combined with the knowledge that the plant dynamics are relatively smooth above this frequency, which allows roll-off to be introduced, then this demonstrates that robust rate feedback can be used even with non-collocated (and hence inexpensive) sensing. This is a critical enabler for robust control of a distributed force actuated DM.

The performance of the rate feedback loop is shown in Fig. 4 for the simulation example described in Section 2.2. A rate feedback gain in Eq. (5) of 75 is used, slightly lower than the optimal value of $G^{-1} \simeq 100$ (for added robustness). For our simulation, a low-pass filter is included at 1.5 kHz. For a real implementation this might not be necessary because actuator or sensor dynamics will introduce filtering; this frequency would be the minimum actuator bandwidth for the simulation parameters used herein. The three diagrams in Fig. 4 plot the response from force at one actuator location to the corresponding sensor signal y derived from the average of four neighbor sensors. Figure 4(a) shows the open-loop transfer function (same as Fig. 3), which is highly resonant at low frequencies. Figure 4(b) is the transfer function when the rate feedback loop is closed only for the actuator observed. Modes with non-zero residuals at that location are damped, but of course there is no effect on the anti-resonances, where there is no displacement at that location. Figure 4(c) is a plot of the response when all rate feedback loops are closed. The resonant behavior has been suppressed by adding the active damping and the mirror behaves as if it were infinite: disturbances are dissipated before they propagate across the mirror and reflect back to constructively interfere. This provides a more straightforward system for the design of the position control loop.

4. Position Control

4.1. Collocated Feedback

The purpose of the position control loop is to provide a good command response for the outer adaptive optics loop. In particular, minimal phase lag and a relatively flat frequency response up to at least 50 Hz are essential. A block diagram describing the overall feedback control architecture is shown in Fig. 5. The open-loop plant dynamics are given by **G**; the other blocks will be described below.

The rate feedback, $\mathbf{K}_V$, described in Section 3 provides electronic damping using SISO feedback for each actuator. Similarly, the simplest position control is collocated SISO feedback. This can be interpreted as implementing electronic springs, and positivity can again be used to guarantee robust stability. This is the approach taken in [13], and corresponds to choosing $\mathbf{Q} = \mathbf{I}$ in Fig. 5. The performance with this approach is shown in Fig. 6, with $\mathbf{K}_P$ from Fig. 5 representing P-controllers with the highest possible gain while maintaining a stable system (a PI control could also be used). The command response at the representative actuator is -8 dB, with the response at the adjacent actuator only slightly smaller. There is substantial coupling in the plate, and while one actuator pushes up to achieve the desired response, the adjacent actuators are all counteracting this to achieve the different response desired at those locations. The net result is that at the maximum stable gain, the feedback control has very little effect on this high spatial frequency command response.

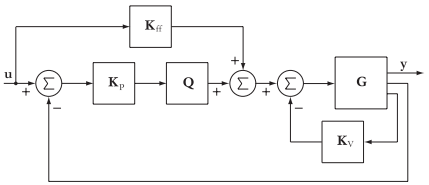

Fig. 5. Block diagram for overall control architecture. See text for definitions.

The response of the mirror to position commands could also have been plotted for commands at different spatial frequencies, rather than for a command at an individual actuator. The mirror compliance $\mathbf{C}$ is much higher at low spatial frequencies than at high; for our simulation example, the condition number of the static plant response ($\mathbf{G}(0) = \mathbf{C}$) is of the order of 10^5. This means that there is much higher loop gain for low spatial frequencies, and quite good command response, but low loop gain and hence poor command response at high spatial frequencies.

A possible solution to this is to implement feedforward control (as used in [13]). Based on open-loop calibration of the deformable mirror, the best estimate of the force distribution required to achieve the desired command response is fed to the actuators, and feedback is only required to compensate for errors in the feedforward matrix. The matrix $\mathbf{K}_{ff}$ in Fig. 5 is ideally the stiffness matrix evaluated at the actuator locations. While using a priori information about the system is always beneficial, the low feedback gain at high spatial frequencies means that the deformable mirror is effectively operating in open loop to high spatial frequency commands; this then requires accurate calibration to ensure adequate performance. Note that it is the inverse of the plant that is required for the feedforward control; higher accuracy is required for the plant model than will be obtained on the estimate of the inverse unless an approach is used to

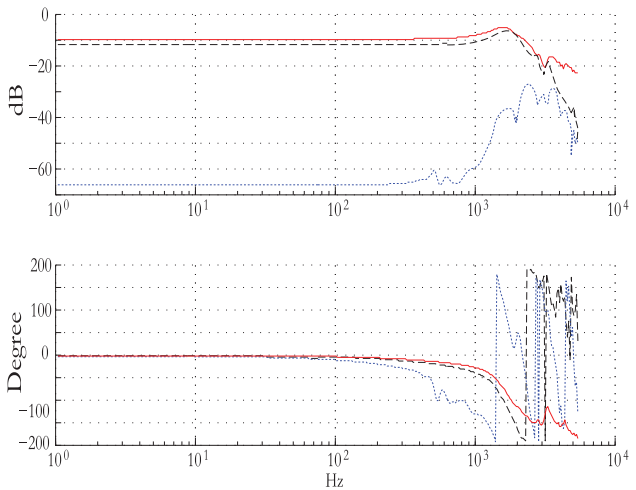

Fig. 6. Command response at representative actuator using collocated position control (solid line), and cross-talk to a neighbour actuator (dashed line) and a distant actuator (doted line).

measure the inverse directly. Section 4.3 compares the performance robustness of this algorithm with the approach developed below.

4.2. Local Feedback

Clearly if the matrix $\mathbf{Q}$ in Fig. 5 were selected equal to the inverse of the plant at least at zero frequency, the system would be much better conditioned. However, this not only requires the same information as the feedforward solution, but would now be within the control loop, leading to potential instability for small errors in the plant model. However, recall that the problem occurs due to each actuator counteracting the control at the adjacent actuators. The coupling can therefore be significantly reduced using only local information. This enhances robustness relative to using global model information in the feedback. If the control does not require knowledge of the global interaction effects, then it will automatically be robust to uncertainty in these effects; this is verified in Section 4.3.

The goal in choosing the matrix $\mathbf{Q}$ can be stated in one of two (equivalent) ways:

- Given a particular error pattern $\mathbf{e}$, say $e_k = 1$ at the k^{th} actuator and $e_j = 0, j \neq k$, then rather than only applying a force to the k'th actuator (which will produce non-zero response across the entire mirror, see Fig. 7(a)), we wish to apply a force distribution that yields a response pattern to counteract the error, see Fig. 7(c). However, we use only actuators close to actuator k, and will tolerate some error in replicating the error pattern.
- We would like to obtain a matrix $\mathbf{Q}$ that is an approximate inverse to the compliance $\mathbf{C}$ using only local information.

Mathematically, the above problem can be described as choosing the applied force pattern $\mathbf{f}_k$ to minimize the cost function

$$\mathbf{J} = \|\mathbf{C}\mathbf{f}_k - \mathbf{e}\|_2 \tag{6}$$

subject to the constraint that elements of the vector $\mathbf{f}_k$ not in some set Ω_k must be zero. The set Ω_k can be constructed by including all actuators within some specified distance of k. The constrained least-squares problem is equivalent to solving an unconstrained problem with a truncated matrix $\mathbf{C}_{:,\Omega_k}$, indicating that only the columns associated with actuators in Ω_k are retained. Then the optimal $\mathbf{Q}_{\Omega_k,k}$ (giving the appropriate local force distribution to compensate for an error at location k) is the k^{th} row of the pseudo-inverse of the truncated compliance. This is motivated by the local approach used in [10] to develop computationally efficient sparse reconstructor matrices for adaptive optics estimation. A hierarchic or multigrid approach could also be used as in [10, 7] to improve the approximate inverse at larger spatial scales, however, for this application, the larger spatial scales are already adequately controlled.

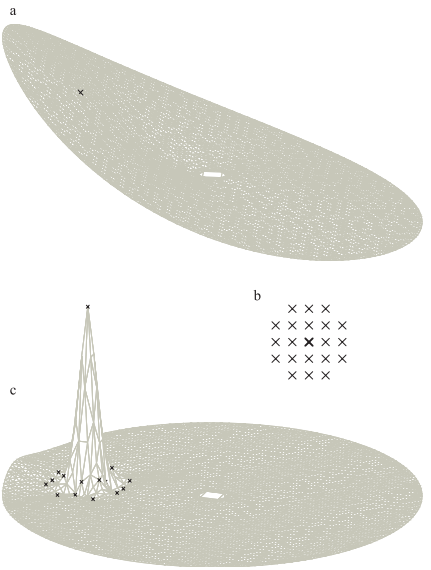

Fig. 7. Overview of the local feedback performance, (a) mirror shape due to a single actuator command, (b) local family group of 21 actuators, (c) mirror shape resulting from unit command to a local actuator family.

Recall that the challenge that motivated the need for $\mathbf{Q}$ was that if a single actuator is used to respond to an error, then there is a large global response. Solving a least squares problem where the minimization is over the entire mirror ensures that the response to an error at location k is mostly local. The purpose of the additional actuators within region Ω_k can be interpreted as minimizing the energy propagation away from the local region, as any such energy will dominate the least-squares performance metric.

To illustrate the effectiveness of this approach, we use the set Ω illustrated in Fig. 7(b). The first "ring" of actuators around the center will push in the opposite direction of the center actuator, to counteract the response that would otherwise occur. The second ring of actuators is useful to minimize energy propagation away from the local region. The closed-loop response pattern obtained using this local $\mathbf{Q}$ and the architecture in Fig. 5 is shown in Fig. 9, both for an actuator away from any boundary, and for an actuator location on the boundary. Note that because the additional actuators are required only to minimize energy propagation out of the local region,

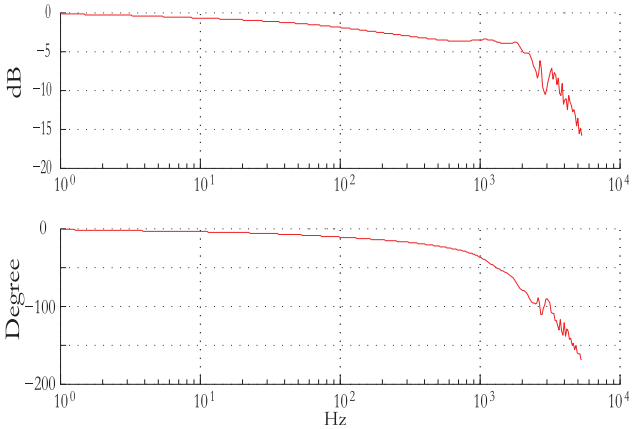

Fig. 8. Open-loop response for position-control loop (from an input to **Q** to position) at a representative actuator using local control approach. The **Q** matrix derived at DC-performance works reasonably well up to about 1000 Hz.

boundary regions where there are fewer actuators in Ω actually perform better.

There is clearly significant potential for exploring different possible sizes for the set Ω; better performance will occur with larger sets, at the expense of robustness due to the requirement for additional structural dynamics information. The appropriate trade-off for a given mirror and actuator/sensor layout can be obtained by looking at the residual least-squares performance metric from (6) as a function of the size and pattern Ω, and choosing the set beyond which there is diminishing benefit from using additional actuators. Simulations in the next section illustrate that the set chosen here is sufficient.

Referring back to Fig. 5, the alternate interpretation of the purpose of **Q** is to improve the conditioning of the position-control plant at zero frequency, **CQ**. Using the local set of actuators in Fig. 7(b), the condition number of **CQ** is reduced from $\sim 10^5$ with $\mathbf{Q} = \mathbf{I}$ to ~ 2, a remarkable improvement using at most 6% of the actuators to construct each column of the approximate inverse.

Using the local solution **Q**, the response from the input of the position-control plant **GQ** to the output is now much closer to the identity matrix; the output response distribution is similar to the input distribution. A representative open-loop transfer function for high spatial frequency for the plant is shown in Fig. 8; it is straightforward to design a stable SISO integral control loop for each degree of freedom. The final result, shown in Fig. 9, indicates a flat response up to 200 Hz for actuators at the edges and up to 100 Hz for the remaining actuators. The step response of the mirror at every actuator location to a unit command at a representative actuator is shown in Fig. 10. It is evident that there exists little cross-talk between a commanded actuator and the actuators outside the local family.

Increasing the integral gain leads to instability due to cross-talk between local families and local dynamics within each local region Ω. The command response and cross-talk are both excellent for use with an outer AO loop, with roughly 25° phase lag at the expected AO bandwidth of 50 Hz.

4.3. Robustness

The robustness of the control system depends on the accuracy of **Q**, or equivalently, on the uncertainty in the plant. The matrix **Q** can be determined either by modeling or experimentally through poking of actuators. Both options will lead to somewhat incorrect elements of **Q**.

For a lightly damped structure, small uncertainties in the resonant frequencies will lead to large uncertainty in the transfer function; this type of structured uncertainty in the system is poorly represented by unstructured uncertainty models. We instead evaluate stability- and performance-robustness for this system by explicitly evaluating the effect of multiplicative uncertainty in the resonant frequencies, while keeping the damping ratio constant.

The metric we use to compare the command-response performance of different algorithms in the presence of model uncertainty is to compute the mean-square error over all spatial degrees of freedom and within the 0–50 Hz expected bandwidth of the AO system. Fig. 11 compares

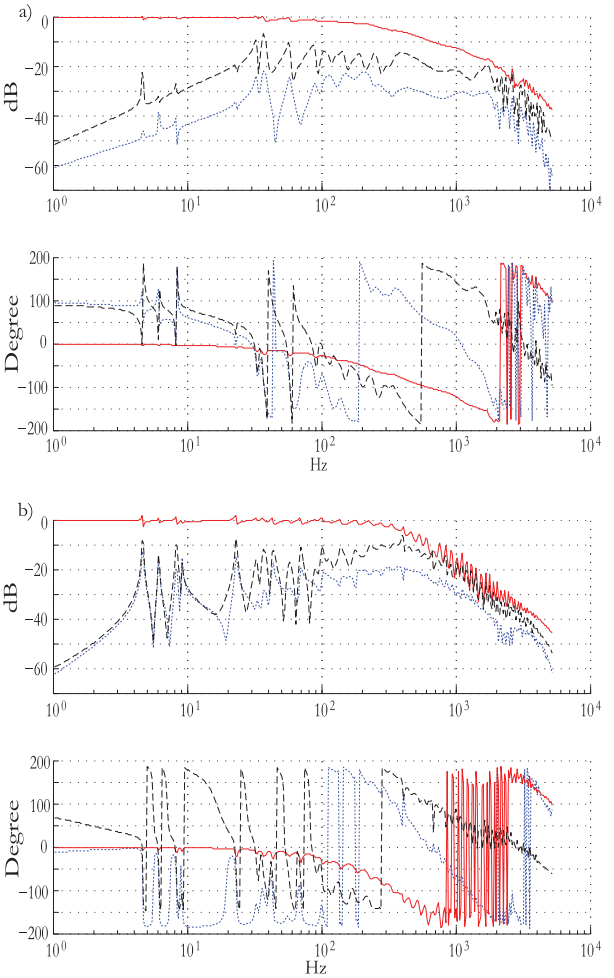

Fig. 9. Command response using local control approach at two different actuator locations away from (a) and at outer boundary (b), illustrating collocated response (solid line), and cross-talk to a neighbouring (dashed line) and a distant actuator (dotted line). The half-power bandwidth exceeds 100 Hz, and the phase lag at 50 Hz is less than 25°.

this error index in the presence of bounded uncertainty in the structural resonances for three different control approaches:

1. A guaranteed-stable collocated position control (the matrix **Q** is the identity matrix). Acceptable performance requires feedforward, and the fully-populated best model-based estimate of the required force distribution pattern is used, constructed from the nominal model without uncertainty; this is similar to the approach used in [3, 13].
2. The local control approach presented herein (the matrix **Q** is sparse and local). While not required for acceptable performance, the same feedforward is used

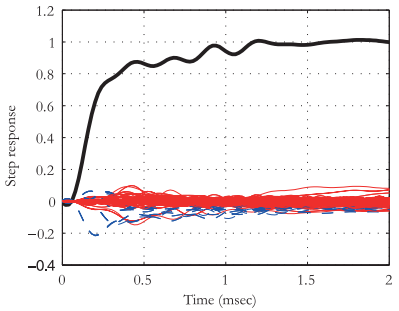

Fig. 10. Step response for the local approach suggested here, with feedforward. The response for a commanded actuator (thick line), the corresponding response of the local family (dashed lines) and the cross-talk to actuators outside the local family (thin lines).

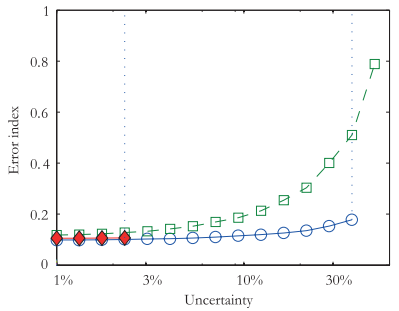

Fig. 11. Performance robustness comparison for three different controllers: the local approach suggested here ("○"), collocated control ("□", dashed), and with global feedback of all sensors to all actuators ("♦"). All are plotted assuming feedforward information is used. Uncertainty is bounded random errors in the mirror resonant frequencies, and the error index is the mean-square command-response error averaged over all controlled spatial degrees of freedom and temporal frequency from 0 to 50 Hz. The error index is infinite (indicated by the dashed line) if the closed-loop system is not stable, which occurs for both the local and global feedback.

as above in order to make a direct comparison between the approaches.

3. A global control approach, where **Q** is the best model-based estimate of the required force distribution, again for the nominal model. Again, feedforward information is also assumed.

The three approaches above are listed in order of how much information is needed in the feedback path about the system dynamics. Other model-based control algorithms are certainly possible that would be more robust than the global approach we compare to here. The vertical dashed lines in Fig. 11 indicate the uncertainty at which the local and global approaches are not guaranteed to be stable. The local position control approach proposed here gives nominal performance close to that of the global approach, and maintains stability for 40% uncertainty in resonant frequencies, more than 10 times what can be tolerated with this global approach. Because there is sufficient temporal feedback bandwidth on almost all of the spatial degrees of freedom controlled by the DM, the performance does not degrade as quickly with increasing model error as for the collocated approach, where performance on many high spatial-frequency degrees of freedom is essentially obtained in open-loop with only feedforward correction.

Note that increasing the size of the actuator set (number of actuators used in each local family) would improve performance at the expense of robustness (as it requires more model information). Since the performance with this local set is nearly the same as with full global information, there appears to be no advantage to increasing the set size.

5. Conclusions

Traditional actuators for large deformable mirrors call for tight construction tolerances, which imply high costs. We have here demonstrated a stable and robust control strategy that enables a low-cost scheme using force actuators and electret microphone sensors. There is a potential for dramatic cost savings, especially for large DMs beyond 1 m in diameter with thousands of actuators. Further, the suction cup attachment concept gives easy access for replacement of the actuators and microphones, which is important for maintenance.

The predicted DM performance using the SISO rate feedback and local position feedback approach described herein is promising and meets the requirement of an AO-system. The half power bandwidth of the transfer function between commanded actuator force and displacement of the faceplate for the simulation parameters used here is ∼110 Hz, with less than 25° phase lag at a plausible AO bandwidth of 50 Hz. The performance-robustness of the proposed local control approach to uncertainty in the mirror structural dynamics is good, and better than either a purely collocated approach or a simple global model-based approach.

We have above assumed force actuators and position sensors to be ideal. Actual force actuators perform as low-pass filters whereas the position sensors based upon electret microphones can be seen as band-pass filters. The effect of high-frequency actuator and sensor dynamics will be small provided that the cut-off frequencies are beyond ∼1.5 kHz where roll-off is intentionally introduced into the rate feedback in our model. The effect of actuator and sensor dynamics, together with implementation delays,

influences the phase margin for the rate feedback loop and thus will reduce the maximum tolerable separation between actuators and sensors in a quantifiable way. The influence of low-frequency microphone roll-off is also expected to be neglible, because the wavefront sensor for the outer AO loop provides sufficient information at low frequencies, where the microphones have low response.

Future work involves optimization of actuator and sensor design, new prototyping, including the modelled and measured dynamics of the force actuators and microphones in the model, and constructing a prototype mirror in the 1 m class.

The control architecture presented in this paper can also be used in other fields. For example, use of a very thin primary mirror in space telescopes is appealing for the weight budget; the controller developed here could be used to maintain the shape of the mirror.

References

1. Andersen T, Garpinger O, Owner-Petersen M, Bjoorn F, Svahn R, Ardeberg A. Novel concept for large deformable mirrors. *Opt Eng* 2006; 45(7): 073001113.
2. Benassi L, Elliott SJ. The equivalent impedance of power-minimising vibration controllers on plates. *J Sound Vib* 2005; 283: 47–67.
3. Biasi R, Andrighettoni M, Veronese D, *et al*. LBT adaptive secondary electronics. *Adap Opt Syst Technol II* 2003; 4839: 772–782.
4. D'Andrea R, Dullerud G. Distributed control design for spatially interconnected systems. *IEEE Trans Autom Control* 2003; 48(9): 1478–1495.
5. Kendrew S, Doel P. Finite element analysis of carbon fibre composite adaptive mirrors. *Adv Adap Opt* 2004; 5490: 1591–1599.
6. Kulkarni R, D'Andrea R, Brandl B. Application of distribution control techniques to the adaptive secondary mirror of Conrell's Large Atacama Telescope. *Proc SPIE* 2003; 4839.
7. Lessard L, West M, MacMynowski D, Lall S. Warm-started wavefront reconstruction for adaptive optics. *J Opt Soc Am A* 2008; 25(5): 1147–1155.
8. Lyon RH. *Machinery Noise and Diagnostics*. Butterworth Publishing 1987.
9. MacMartin DG, Hall SR. Control of uncertain structures using an H_∞ power flow approach. *AIAA J Guid Control Dyn* 1991; 14(3): 521–530.
10. MacMartin DG. Local, hierarchic, and iterative reconstructors for adaptive optics. *J Opt Soc Am* 2003; 20(6):1084–1093.
11. Miller DW, Grocott SCO. Robust control of the multiple mirror telescope adaptive secondary mirror. *Opt Eng* 1999; 38(8): 1276–1287.
12. Preumont A. Vibration control of active structures: an introduction. Academic Publishers, 2002.
13. Riccardi A, Brusa G, Salinari P, *et al.* Adaptive secondary mirrors for the large binocular telescope. *Astron Adap Opt Syst Appl* 2003; 5169: 159–168.

Paper II

Suppressing Low-Order Eigenmodes with Local Control for Deformable Mirrors

Rikard Heimsten[a], Mette Owner-Petersen[a], Thomas Ruppel[b]
Douglas G. MacMynowski[c], Torben Andersen[a]

[a] *Lund Observatory, Lund University, Box 43, SE-221 00 Lund, Sweden*
[b] *Institute for System Dynamics, University of Stuttgart, Postfach 80 11 40 D-70511 Stuttgart,Germany*
[c] *Control and Dynamical Systems, California Institute of Technology 1200 E. California Blvd., Pasadena, CA 91125, USA*

Abstract

To improve the mechanical characteristics of actively controlled continuous faceplate deformable mirrors in adaptive optics, a strategy for reducing crosstalk between adjacent actuators and for suppressing low-order eigenmodes is proposed. The strategy can be seen as extending Saint-Venant's principle beyond the static case, for small local families of actuators.

An analytic model is presented, from which we show the feasibility of the local control. Also, we demonstrate how eigenmodes and eigenfrequencies are affected by mirror parameters, such as thickness, diameter, Young's modulus, Poisson's ratio and density. This analysis is used to evaluate the design strategy for a large deformable mirror, and how many actuators are needed within a family.

Keywords: Distributed control, adaptive optics, large deformable mirror, dimensionless mode analysis.

1 Introduction

Most adaptive optics systems include a small deformable mirror, typically with a size of a few tens of millimeters, because it is much easier to achieve a high temporal bandwidth for a small mirror than a large one. Integrating the deformable mirror into the telescope design, thus going from tens of millimeters to a few meters in diameter, will avoid lossy relay optics and make the telescope more compact [1]. Large deformable mirrors have successfully been integrated into the Multi Mirror Telescope [2] and the Large Binocular Telescope [3].

Large deformable mirrors are generally implemented as thin shells of a glass ceramic with hundreds or thousands of actuators on the back. Often, there are also local

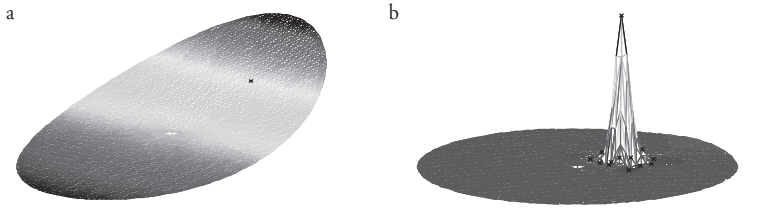

Figure 1: An overview of the local control concept of the deformable mirror. a): The influence function of a single actuator command. b): The influence function of 21 actuator commands optimized to provide a local deflection.

deflection sensors on the back of the mirror for closed-loop control in combination with a wavefront sensor monitoring overall optical system quality.

Several types of actuators exist. Piezoelectric actuators are simple to control but the strokes are small and the overall system cost becomes high due to tight manufacturing tolerances. Force actuators based upon the voice coil principle have the potential of large stroke and low cost but are more difficult to control because the control system must handle the structural dynamics of the deformable mirror. We here focus on voice coil actuators.

Studies of multiple-input-multiple-output optimal controllers for deformable mirrors have shown good closed-loop performance. [4, 5]. However, neither the computational load nor the robustness of a global controller may be suitable for large deformable mirrors. In earlier publications [6, 7], we have studied a deformable mirror concept with faceplate, and low-cost force actuators and sensors, by numerical methods. This system has been demonstrated to work using a control system, encompassing local control with position and velocity feedback. The local control concept was developed to suppress crosstalk between adjacent actuators as shown in Fig. 1. A command to a single actuator induces a tip/tilt to the whole mirror. If instead a local control scheme, encompassing a set of actuators, is used, the influence function of the controlled actuator can be made similar to a delta function. Hence, the local controllers only weakly excite low-order eigenmodes.

In this paper, we present an analytic model to study excitation of the various normal modes. An analysis is made to see how the control concept is affected by mirror dimensions. Further, we show how the eigenmodes and eigenfrequencies depend on mirror parameters. We validate our results by comparing the result obtained by the analytic model and a finite element model for a specific design.

2 Background

Design parameters of an actuator system for deformable mirrors involve optimal placement of the actuators and choice of control scheme. In practice, the actuator topology cannot be chosen arbitrarily due to space constraints. We have assumed a Cartesian

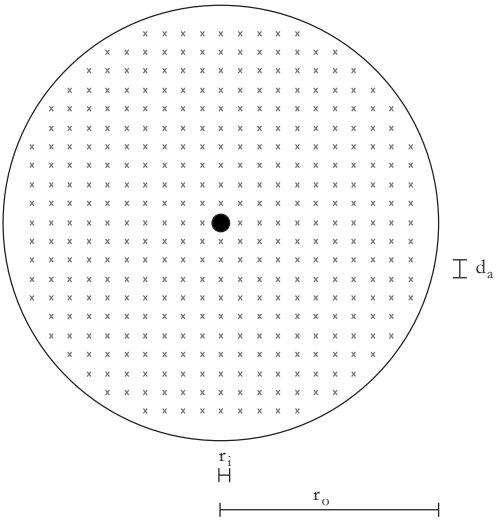

Figure 2: An overview of the deformable mirror, which is clamped at the inner edge and free at the outer edge. The crosses illustrate the actuator topology. The actuator pitch, d_a, inner hole radius, r_i, and plate radius, r_o, are marked.

actuator topology, as shown in Fig. 2 and below we concentrate on selection and evaluation of a control strategy.

For the case where the force actuators and the back position sensors are collocated and have a high bandwidth from DC to many kHz, it is possible to control each actuator independently with feedback from the collocated sensor only. By differentiating the position signal, a velocity signal can be obtained and an "electronic damper" can be implemented. Also, using the position signal, an "electronic spring" can be established at the location of an actuator and a sensor. Provided that the bandwidths of the actuator and sensor are sufficiently high, it can be readily seen that such a system can be made stable because no energy is injected into the system [6]. The solution has been used for medium-sized deformable mirrors [8].

However, it is cumbersome from a design point of view to use collocated actuators and back sensors, and it is much less expensive to use position sensors placed between the actuators. These sensors can be implemented with electret microphones and bellows much like stethoscopes [9]. The challenge is that they do not provide a DC response, i.e. they roll off with 20 dB/decade from about 20 Hz and downwards to lower frequencies. Also, they do not work well at high frequencies due to resonances in the bellows.

The same is true for the low-cost actuators referred to above. They are attached to the back of the mirror through suction cups having a certain compliance, leading to additional resonance effects. Although an internal loop in the actuator largely suppresses suction cup influence, the bandwidth of the actuators in practice is limited to some 2-3 kHz.

The task is therefore to develop a control system with a bandwidth of about 100 Hz for a thin mirror plate with bandwidth limited actuators and sensors placed in a Cartesian topology. Introduction of a local control concept with "families" of actuators has proven advantageous because low-order eigenmodes are then only weakly excited [7]. An actuator family consists of a central actuator with one or more rings of actuators around it. Any actuator therefore belongs to more than one family. The force distribution in a given family is predetermined and scaled by an input signal to that family. Hence all forces in a family are in phase. In reference [6] we present an approach for selection of a family force pattern, when a finite element model is available. Below, we give an analytical approach for determination of the pattern.

3 Mathematical model

The deformable mirror plate is modeled as a solid, circular plate, with constant thickness h and an outer radius of r_o, see Fig. 2. It is centered at the origin of the $r-\phi$ plane, where r, ϕ are polar coordinates.

The time varying deflection of the mirror perpendicular to its surface with respect to the undeformed reference plate is called $w(r,\phi,t)$, where t is the time. The partial differential equation governing an undamped plate is given by [10]

$$D\nabla_r^4 w(r,\phi,t) + \rho h \frac{\partial^2 w(r,\phi,t)}{\partial t^2} = q(r,\phi,t) \tag{1}$$

where ρ is material density, D is the flexural rigidity and $q(r,\phi,t)$ is the lateral load per unit area. The biharmonic operator ∇_r^4 is defined as

$$\nabla_r^4 \equiv \left(\frac{\partial^2}{\partial r^2} + \frac{1}{r}\frac{\partial}{\partial r} + \frac{1}{r^2}\frac{\partial^2}{\partial \phi^2} \right)^2$$

The deformable mirror plate is clamped at its inner rim with a radius of r_i, see Fig. 2, which gives the boundary conditions

$$w(r_i,\phi,t) = 0 \tag{2a}$$

$$\left.\frac{\partial w}{\partial r}\right|_{r=r_i} = 0 \tag{2b}$$

since the lateral displacement and slope are zero. The outer edge is free which gives the following boundary conditions

$$\left. D\left(\frac{\partial^2 w}{\partial r^2} + \frac{\nu}{r}\frac{\partial w}{\partial r} + \frac{\nu}{r^2}\frac{\partial^2 w}{\partial \phi^2} \right) \right|_{r=r_o} = 0 \tag{3a}$$

$$\left. D\left(\frac{\partial}{\partial r}\nabla^4 w + (1-\nu)\frac{\partial^2}{\partial r^2}\left(\frac{1}{r^2}\frac{\partial w}{\partial r} - \frac{w}{r^3} \right) \right) \right|_{r=r_o} = 0 \tag{3b}$$

where the radial moment and radial shear forces are zero [11]. The term ν is Possion's ratio.

3.1 Modal analysis

A parameterization by separation of variables as $w(r,\phi,t) = W(r,\phi)e^{-i\omega t}$ can be made [12], where ω is the vibration frequency. Using the parameterization, the homogeneous version of Eq. 1 reads

$$\nabla_r^4 W(r,\phi) = \beta^4 W(r,\phi) \tag{4}$$

where $\beta^4 = \frac{\omega^2 \rho h}{D}$. The general solution to Eq. 4 is given in [12] by

$$\begin{aligned}
W(r,\phi) &= W_{1,k}(r,\phi) + W_{2,k}(r,\phi) && \text{(5a)}\\
W_{1,k}(r,\phi) &= [A_{1,k}J_k(\beta r) + A_{3,k}Y_k(\beta r)]\sin(k\phi) \\
&\quad + [A_{2,k}J_k(\beta r) + A_{4,k}Y_k(\beta r)]\cos(k\phi) && \text{(5b)}\\
W_{2,k}(r,\phi) &= [B_{1,k}I_k(\beta r) + B_{3,k}K_k(\beta r)]\sin(k\phi) \\
&\quad + [B_{2,k}I_k(\beta r) + B_{4,k}K_k(\beta r)]\cos(k\phi) && \text{(5c)}
\end{aligned}$$

where J_k and Y_k are Bessel functions of order $k \in \mathbb{N}$ and of the first and second kind, respectively. The second term of Eq. 5a involves the modified Bessel functions I_k and K_k of the order k and of the first and second kind. Thereby, the following equivalent relations hold [13]

$$\begin{aligned}
I_k(x) &= \mathrm{i}^{-k} J_k(\mathrm{i}x) \\
Y_k(x) &= \frac{1}{\pi}\left(2(\gamma + \ln\frac{x}{2})J_k(x) - \sum_{n=0}^{k-1}\frac{(k-n-1)!x^{2n-k}}{2^{2n-k}n!}\right. \\
&\quad \left. - \sum_{n=0}^{\infty}\frac{(-1)^n\chi(k+n+\chi(n))x^{k+2n}}{2^{k+2n}n!(k+n)!}\right) \\
&\quad \text{with} \quad \chi(n) = \begin{cases} 0 & \text{if } n = 0 \\ \sum_{l=1}^{n}\frac{1}{l} & \text{if } n > 0 \end{cases} \\
K_k(x) &= \frac{\pi}{2}\mathrm{i}^{k+1}(J_k(\mathrm{i}x) + \mathrm{i}Y_k(\mathrm{i}x))
\end{aligned}$$

with $\mathrm{i} = \sqrt{-1}$ and γ being the Euler constant.

3.2 Participation factor

The modal participation factor measures the coupling between an exciting point force and a given mode shape. An analytic expression for the modal participation factor will now be determined.

The deflection of the mirror can be written using a superposition of the eigenmodes as

$$w(r,\phi,t) = \sum_{k=1}^{\infty} c_k W_k(r,\phi)e^{-i\omega t} \tag{6}$$

where $W_k(r,\phi)$ is the kth eigenmode and c_k the participation factor, with the dimension of length, of that normal mode. We define $W_k(r,\phi)$ as the dimensionless eigenmode

satisfying the orthonormality relations

$$\frac{1}{A}\int_{r_i}^{r_o}\int_0^{2\pi} W_k(r,\phi)W_l(r,\phi)r\mathrm{d}r\mathrm{d}\phi = \delta_{k,l}$$

where $\delta_{k,l}$ is the Kronecker delta and A is the total area of the plate. The external load reads

$$q(r,\phi,t) = u\frac{1}{r}\delta(r-R)\delta(\phi-\Phi)e^{-i\omega t} \tag{7}$$

for a point force u at the position (R,Φ) where $\delta(x)$ is Dirac's delta function, which then gives [14]

$$\int_0^{\infty}\int_0^{2\pi}\frac{1}{r}\delta(r-r')\delta(\phi-\phi')r\mathrm{d}\phi\mathrm{d}r = 1$$

Using Eq. 6 to describe the deflection of the plate and Eq. 7 to describe the external forces, use of the plate dynamics Eq. 1 gives

$$D\nabla_r^4\sum_{k=1}^{\infty}c_kW_k(r,\phi) - \rho h\omega^2\sum_{k=1}^{\infty}c_kW_k(r,\phi) = u\frac{1}{r}\delta(r-R)\delta(\phi-\Phi)$$

where $e^{-i\omega t}$ has been eliminated from the equation. Using the identity of the eigenfunctions, given by Eq. 4, this equation can be simplified to

$$\rho h\sum_{k=1}^{\infty}(\omega_k^2-\omega^2)c_kW_k(r,\phi) = u\frac{1}{r}\delta(r-R)\delta(\phi-\Phi) \tag{8}$$

Multiplying with one specific eigenmode $W_l(r,\phi)$ and integrating over the full plate gives

$$\begin{aligned}&\int_{r_i}^{r_o}\int_0^{2\pi}W_l(r,\phi)\rho h\sum_{k=1}^{\infty}(\omega_k^2-\omega^2)c_kW_k(r,\phi)r\mathrm{d}r\mathrm{d}\phi\\ =&\int_{r_i}^{r_o}\int_0^{2\pi}W_l(r,\phi)u\frac{1}{r}\delta(r-R)\delta(\phi-\Phi)r\mathrm{d}r\mathrm{d}\phi\end{aligned}$$

The left hand side can be reduced by using the orthonormality condition of the eigenmodes and the right hand side is reduced, since the Dirac delta function is zero outside (R,Φ). Thus, the participation factor can be expressed as

$$A\rho h(\omega_l^2-\omega^2)c_l = uW_l(R,\Phi) \tag{9a}$$

$$c_l = \frac{uW_l(R,\Phi)}{M(\omega_l^2-\omega^2)} \tag{9b}$$

where M is the total mass of the plate. The unrealistic behavior of $c_l\to\infty$ when $\omega\to\pm\omega_l$ occurs, since the damping of the system has yet not been considered.

4 Results

In Sec. 4.1 a dimensionless mode analysis is made for the mirror layout in Fig. 2. The example case used to derive the results presented in Sec. 4.2-4.4 is a mirror made of borosilicate. The parameters are given in Table 1.

Parameter	Definition	Value
E	Young's modulus	63×10^9 Pa
ρ	density	2.23×10^3 kg/m^3
ν	Poisson ratio	0.2
h	thickness	2 mm
D	bending stiffness	$Eh^3/12(1-\nu^2)$
r_o	radius of the mirror	0.5 m
r_i	radius of the inner hole	0.025 m
d_a	actuator pitch	0.045 m
ζ	damping ratio	1%

Table 1: Parameter values for a 1 m deformable mirror used for performance studies.

4.1 Dimensionless mode analysis

We perform a dimensionless modal analysis to establish the relationship between the normal modes and design parameters, such as thickness, Poisson's ratio, bending stiffness and mirror dimensions. The analysis is valid for any given plate with the same r_o/r_i ratio as shown in Fig. 2. The dimensionless quantity ξ is defined as

$$\xi = \frac{r}{r_o}$$

The biharmonic operator, ∇^4_ξ, for the coordinate plane $\xi-\phi$ is related to ∇^4_r as

$$\nabla^4_r = \left(\frac{1}{r_o}\right)^4 \nabla^4_\xi$$

Thus, the homogenous equation given in Eq. 4 is changed to

$$\nabla^4_\xi W(\xi,\phi) = \alpha^4 W(\xi,\phi)$$

where $\alpha^4 = \frac{r_o^4\omega^2\rho h}{D}$. To determine the eight coefficients of Eq. 5, the boundary conditions of the plate are used. The coefficients can be computed considering the sine and cosine parts of Eq. 5 independently [15]. Thus, two sets of four equations can be used to determine the corresponding coefficients $(A_{1,k},A_{3,k},B_{1,k},B_{3,k})$ and $(A_{2,k},A_{4,k},B_{2,k},B_{4,k})$. The resulting equations can be written in matrix form as

$$\mathbf{\Lambda}(\alpha_k)_{\sin}\begin{Bmatrix}A_{1,k}\\A_{3,k}\\B_{1,k}\\B_{3,k}\end{Bmatrix}=0 \qquad \mathbf{\Lambda}(\alpha_k)_{\cos}\begin{Bmatrix}A_{2,k}\\A_{4,k}\\B_{2,k}\\B_{4,k}\end{Bmatrix}=0 \tag{10}$$

where $\mathbf{\Lambda}(\alpha_k)_{\sin}$ and $\mathbf{\Lambda}(\alpha_k)_{\cos}$ are 4-by-4 matrices with elements determined by the boundary conditions. The equivalent boundary conditions in Eq. 2 and 3 for $w(\xi,\phi,t)$ depend only on the physical parameter ν. Thus, the normal modes depend on Poisson's

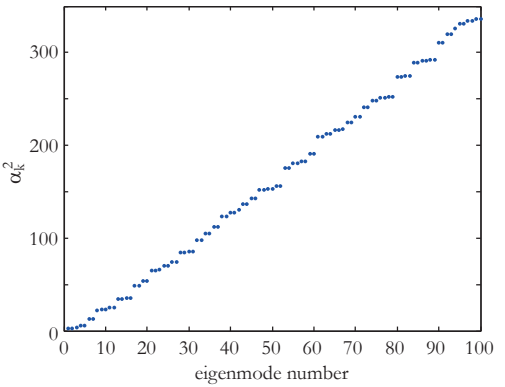

Figure 3: The first hundred α_k^2 values for a mirror with the layout of Fig. 2, where $r_o/r_i = 20$.

ratio, the r_o/r_i ratio and the α_k's. The eigenfrequencies for the eigenmodes are found by

$$\det(\mathbf{\Lambda}(\alpha_k)) = 0$$

which must hold for all non-trivial solutions of Eq. 10. The values of α_k are dimensionless and they are the same for any given mirror with the same r_o/r_i ratio and the same Poisson's ratio. The eigenfrequencies, ω_k, are given by

$$\frac{\omega_k}{\omega_0} = \alpha_k^2 \quad \text{for} \quad \omega_0 = \sqrt{\left(\frac{1}{r_o}\right)^4 \frac{Eh^2}{12\rho(1-\nu^2)}} \tag{11}$$

where ω_0 is unique for the mirror. Note, as $r_o \to \infty$, all eigenfrequencies go to zero. Thus, only a plate of finite size will have eigenmodes, formed by reflection of bending waves by the boundaries. Also the ratio between two specific eigenfrequencies will remain the same regardless of the specific value of ω_0. The first hundred α_k values for a mirror with a a ratio of 20 between the outer and inner radius are shown in Fig. 3. When ω_0 and the α_k's are given, the number of normal modes that must be controlled within a given bandwidth will also be given. The example case in Table 1 gives a value of ω_0 equal to 12.53 rad/s. Thus, there are eighteen normal modes within the bandwidth of the adaptive optics system, i.e. below 100 Hz, and five normal modes below the cutoff frequency (20 Hz) for the back sensors.

4.2 Force patterns analysis

The influence function for one actuator resembles a tip/tilt mode, because this mode is most compliant, see Fig. 1. Thus, the actuator families should be designed to suppress the low-order eigenmodes to reduce crosstalk between adjacent actuators. We now derive an analytic expression to determine the optimal force patterns for a given actuator family. A cost function is formed for the deviation between the static deflection of the

mirror and the desired deflection. The force patterns are found by minimizing the cost function, using a least-squares approach.

An actuator family has a "master" actuator (most often located in the center of the family) at which the desired deflection is one. Elsewhere on the mirror, the deflection should be close to zero. The desired deflection for the mirror then is

$$\frac{1}{r}\delta(r-R_j)\delta(\phi-\Phi_j) \tag{12}$$

when the j'th actuator is controlled, i.e. the desired influence function for a family is a Dirac function. The deflection of the mirror is given through superposition of the individual normal modes as defined by Eq. 6 and the participation factors are given by Eq. 9. For the static case, ω is equal to zero, thus for a single force u at (R,Φ), the deflection invoking m normal modes is

$$w(r,\phi)=\frac{1}{M}\sum_{k=1}^{m}\frac{W_k(r,\phi)}{\omega_k^2}uW_k(R,\Phi)$$

When multiple forces u_i are applied to the plate at different locations (R_i,Φ_i), the equation becomes

$$w(r,\phi)=\frac{1}{M}\sum_{k=1}^{m}\left[\frac{W_k(r,\phi)}{\omega_k^2}\sum_{i=1}^{n}u_iW_k(R_i,\Phi_i)\right] \tag{13}$$

The squared error over the whole mirror, i.e. the cost function, is

$$J=\int_0^{2\pi}\int_{r_i}^{r_o}f(r,\phi,u_i)^2 r\mathrm{d}r\mathrm{d}\phi \qquad \text{where}$$

$$f(r,\phi,u_i)=\frac{1}{M}\sum_{k=1}^{m}\left[\frac{W_k(r,\phi)}{\omega_k^2}\sum_{i=1}^{n}u_iW_k(R_i,\Phi_i)\right]-\frac{1}{r}\delta(r-R_j)\delta(\phi-\Phi_j)$$

Minimizing J with respect to u_l gives

$$\frac{\partial J}{\partial u_l}=\int_0^{2\pi}\int_{r_i}^{r_o}2f(r,\phi,u_i)\frac{\partial f(r,\phi,u_i)}{\partial u_l}r\mathrm{d}r\mathrm{d}\phi=0$$

The above equation results in

$$\sum_{k=1}^{m}\left[\frac{W_k(R_l,\Phi_l)}{\omega_k^4}\sum_{i=1}^{n}u_iW_k(R_i,\Phi_i)\right]=M\sum_{k=1}^{m}\frac{W_k(R_l,\Phi_l)}{\omega_k^2}W_k(R_j,\Phi_j)$$

The equation system to determine the force u_i can be written in matrix form as

$$\mathbf{Au}=\mathbf{b} \tag{14}$$

where the elements in the matrix $\mathbf{A}$ and the vector $\mathbf{b}$ are given by

$$a_{il}=\sum_{k=1}^{m}\frac{W_k(R_l,\Phi_l)}{\omega_k^4}W_k(R_i,\Phi_i)$$

$$b_l=M\sum_{k=1}^{m}\frac{W_k(R_l,\Phi_l)}{\omega_k^2}W_k(R_j,\Phi_j)$$

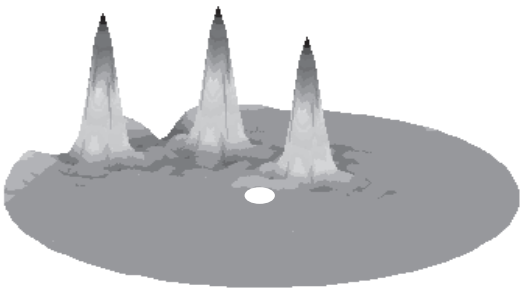

Figure 4: The plate deflection of the mirror is shown for three different actuator family commands, when using 21 actuators in a family.

To summarize the notations, we note that k is the number of the normal mode, m the number of normal modes considered, i the column number of the matrix $\mathbf{A}$, l the row number of the matrix $\mathbf{A}$ and the vector $\mathbf{b}$, and j the actuator being controlled. $\mathbf{A}$ is a square matrix, since both i and l are running from 1 to the number n of actuators in the family. The solution for $\mathbf{u}$ includes the modal stiffness $M\omega_k^2$ and describes the relative distribution of forces within a family with a given location. The corresponding deflection is found from Eq. 13.

For our example, we have studied a family with a center actuator and two rings of actuators around it. Finding the force pattern as described above, we have determined the mirror deflection shown in Fig. 4 for a unity command to each of three families located at different places on the mirror. The influence functions of the families are almost identical over the mirror. At the outer edge, a waffle pattern exists around the family. However, the total root mean square value of the differences between the mirror deflection and the commanded shape over the mirror remains small.

In order to compute the force commands within a given family with sufficient accuracy, it is important to consider a large number of normal modes. This is illustrated in Fig. 5, showing the deflection of the mirror for three cases using the same force excitation. A different number of normal modes, m, have been included, when computing the deflection. The correct force pattern can only be found if the eigenmodes can reproduce the desired influence function within sufficient accuracy. This also implies that the number of normal modes needed depends on the relative actuator pitch, i.e. the total number of actuators. For a given actuator pitch, there is a maximum number of normal modes that can be controlled and this will also roughly be the number of normal modes needed to determine the correct force pattern.

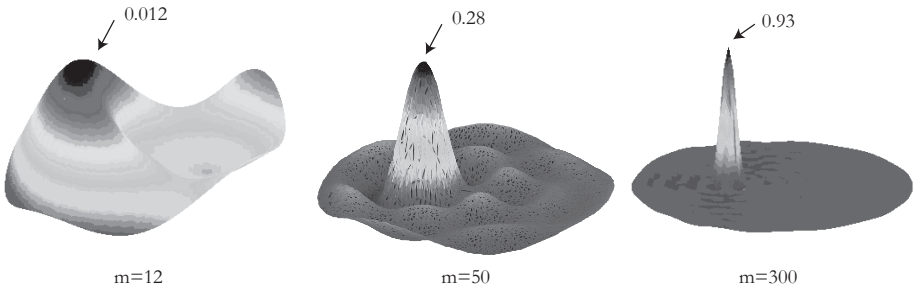

Figure 5: Mirror deflection for the plate example. The same family force input was applied in all three cases but a different number of modes, m, was used in computing the responses.

4.3 Frequency response analysis

We now derive expressions for frequency responses from forces to mirror deflection. Referring to Eq. 9b, the participation factor is

$$c_l = \frac{uW_l(R,\Phi)}{M(\omega_l^2 - \omega^2)}\,, \tag{15}$$

The transfer function from a force to displacement at the same location is determined by inserting Eq. 15 into Eq. 6 which gives

$$\frac{w(R,\Phi)}{u} = \sum_{k=1}^{m} W_k(r,\phi)W_k(R,\Phi)\frac{1}{M(\omega_k^2 - \omega^2)} \tag{16}$$

Due to lack of damping in our model, the term $(\omega_k^2 - \omega^2)$ converges toward zero for $\omega \to \omega_k$. To include the effect of damping, we take analogy in the frequency response of a conventional second-order system

$$\frac{x(\omega)}{f(\omega)} = \frac{1}{M_o\left(\omega_k^2 - \omega^2 + 2\mathrm{i}\zeta_k\omega_k\omega\right)}$$

where M_o is the generalized mass, ζ_k the damping ratio, x the displacement and f the force. By analogy, we can therefore as an approximation introduce damping in Eq. 16 by replacing $(\omega_k^2 - \omega^2)$ with $\left(\omega_k^2 - \omega^2 + 2\mathrm{i}\zeta_k\omega_k\omega\right)$ whereby we get

$$c_l = \frac{uW_l(R,\Phi)}{M(\omega_l^2 - \omega^2 + 2\mathrm{i}\zeta_l\omega\omega_l)} \tag{17}$$

which now encompasses an imaginary term. Inserting Eq. 17 into Eq. 6 and considering that multiple force are applied, the transfer function from force to position reads

$$\frac{w(R,\Phi)}{u} = \sum_{k=1}^{m}\left[\frac{W_k(R,\Phi)}{M(\omega_k^2 - \omega^2 + 2\mathrm{i}\zeta_k\omega\omega_k)}\sum_{i=1}^{n} u_i W_k(R_i,\Phi_i)\right] \tag{18}$$

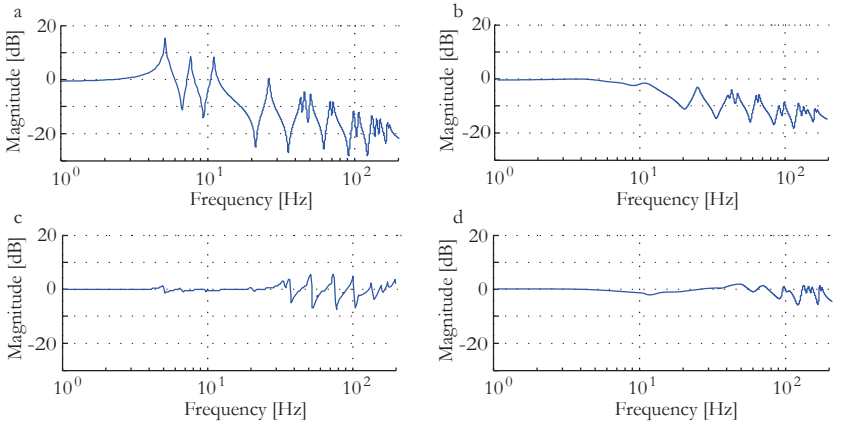

Figure 6: The frequency response for a representative actuator located 0.25 m from the center, from force to position for: a) the plate, b) the plate with families of 9 actuators, c) the plate with families of 21 actuators and d) the plate with families of 59 actuators. The frequency responses are determined with 35 eigenmodes.

The transfer function is evaluated at the point (R,Φ) where the force u is applied and u_i is the relative magnitude between the force applied at the location (R_i,Φ_i) and u. For our example, four frequency responses for a representative actuator location are shown in Fig. 6. The curves are the transfer functions determined from Eq. 18 (for $m = 35$), where the output is the plate deflection at the center of the family and the input is the force command for the single actuator case and for three different family patterns. Using a family, the resonance and antiresonance peaks are attenuated up to a frequency dependent on the number of actuators in the family. If a control system needs a flat frequency response up to a certain frequency, the number of actuators in the family should be chosen accordingly.

4.4 Local control analysis

Three patterns of the local family, including 9, 21 and 59 actuators, are evaluated against the single-input-single-output case, as shown in Fig. 7. A modified version of Eq. 9 is used to compute the participation factor, which then is, neglecting damping

$$c_{l,n} = \frac{1}{M(\omega_l^2 - \omega^2)} \sum_{i=1}^{n} u_i W_l(R_i,\Phi_i) \tag{19}$$

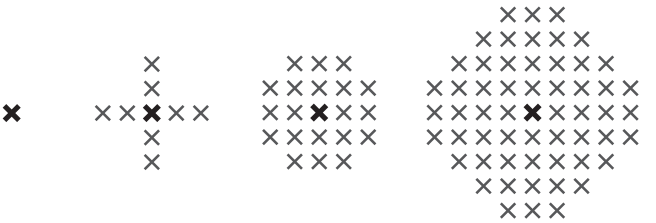

Figure 7: The four family patterns used to evaluate the participation factor.

where n is the number of actuators in the family, and u_i the force computed from Eq. 14. The evaluation of the family concept is done by computing the modal quality factors

$$\mathcal{Q}_9 = \frac{c_{l,9}}{c_{l,1}}$$
$$\mathcal{Q}_{21} = \frac{c_{l,21}}{c_{l,1}}$$
$$\mathcal{Q}_{59} = \frac{c_{l,51}}{c_{l,1}}$$

These quality factors are independent of ω, ω_l and M, and are valid for any plate with the same number of actuators and the same topology. They define the mode-suppression a given family can provide.

For the first twenty normal modes, we present in Fig. 8 the quality factor averages $\bar{\mathcal{Q}}$ for all families on a logarithmic scale. The families encompassing more actuators have more degrees of freedom, which means they should be able to attenuate more eigenmodes. This effect is seen in Fig. 8, where the performance differences between the families increase with the order of the normal mode. The improvement of the quality factor for the eighth, fifteenth and twentieth eigenmodes has the same origin. These three eigenmodes have rotational symmetry, which gives low curvature and low modal stiffness in the radial direction within the families. Because it is sufficient to block excitation in either radial or azimuthal direction, these eigenmodes stand out in Fig. 8.

The number of eigenmodes attenuated are close to half the number of degrees of freedoms in the families. This statement is only partially true for 59 actuators, because the area that the family occupies also increases. This effect is shown in Fig. 9, where the average quality factor is evaluated against the mode number with the relative actuator pitch d_a/r_o as parameter. Thus, doubling the mirror diameter or halving the actuator pitch has the same effect on the quality factors. Conclusively, more actuators on a given plate suppress more eigenmodes for a given number of actuators in the family, or a family with the same actuator pitch and the same number of actuators will suppress more eigenmodes on a 3 m mirror than on a 1 m mirror.

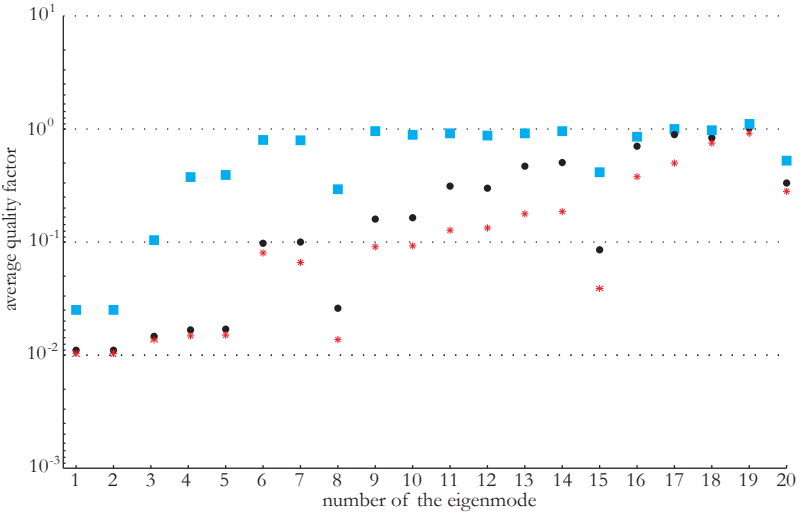

Figure 8: The plot shows the average quality factors $\bar{\mathcal{Q}}_{59}$, $\bar{\mathcal{Q}}_{21}$ and $\bar{\mathcal{Q}}_{9}$ for the 20 first eigenmodes. The squares are for $\bar{\mathcal{Q}}_{9}$, the circles are for $\bar{\mathcal{Q}}_{21}$ and the stars are for $\bar{\mathcal{Q}}_{59}$.

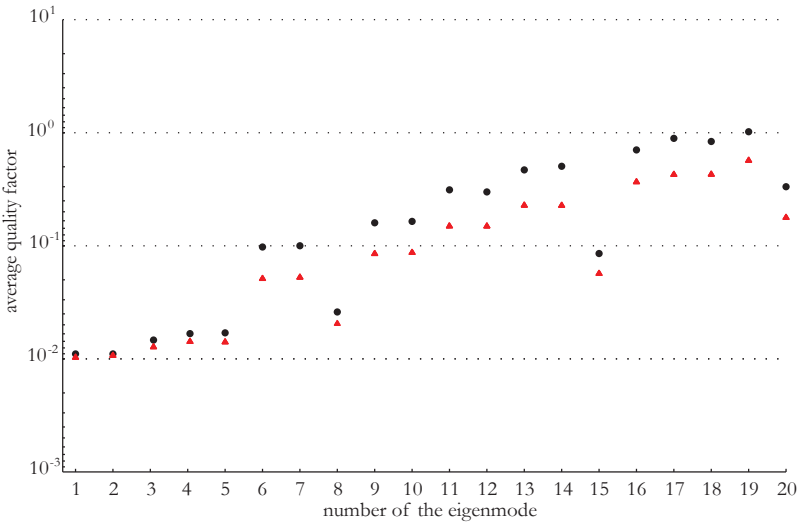

Figure 9: The plot shows the average quality factor $\bar{\mathcal{Q}}_{21}$ for the 20 first eigenmodes. The circles correspond to a relative actuator pitch of 0.09 and the triangles are correspond to relative actuator pitch of 0.045.

	Analytic model	Finite element model	Deviation
ω_1	32.7 rad/s	35.2 rad/s	2.5 rad/s
ω_2	32.7 rad/s	35.2 rad/s	2.5 rad/s
ω_3	48.4 rad/s	48.4 rad/s	0 rad/s
ω_4	69.7 rad/s	70.2 rad/s	0.5 rad/s
ω_5	69.7 rad/s	70.2 rad/s	0.5 rad/s
ω_6	164.6 rad/s	163.3 rad/s	1.3 rad/s
ω_7	164.6 rad/s	163.3 rad/s	1.3 rad/s
ω_8	280.4 rad/s	280.1 rad/s	0.3 rad/s
ω_9	286.1 rad/s	284.7 rad/s	1.4 rad/s
ω_{10}	287.1 rad/s	284.7 rad/s	2.4 rad/s
ω_{11}	312.1 rad/s	310.1 rad/s	2.0 rad/s
ω_{12}	312.1 rad/s	310.1 rad/s	2.0 rad/s

Table 2: A comparison of the twelve first eigenfrequencies as determined by the analytical and the finite element model. Note that ω_0 here is equal to 12.53 Hz.

4.5 Comparison between the analytical and the finite element model

We have performed a comparison between the results of the analytical model presented above and a finite element model [6]. The forms of the eigenmodes agree well with those of the finite element model. The differences in the corresponding eigenfrequencies are shown in Table 2. The deviation between the values from the two models is rather small, about 5%. For the same example, the frequency responses from force to position of the two models for the same representative actuator location are seen in Fig. 10. The full lines represent the single actuator case, where the input is the force of a single actuator and the output is the mirror deflection at the same location. The dashed line is a frequency response for which the input is the command to an actuator family of 21 actuators and the output is the mirror deflection at the location of the center actuator of the family. There is good agreement between the plots of the analytical and finite element models. The minor shifts in the location of the resonance and anti-resonance peaks is due to the eigenfrequency deviation.

For our example, the family force patterns found using the expressions of Sec. 4.2 match well with those derived using the finite element model [6]. The two force patterns agree within 5% and the deviation decreases with an increased number of modes considered in Eq. 14.

5 Conclusion

We have set up an analytical model of a deformable mirror and derived expressions for local control using families of actuators. Eq. 14, based on the least squares method, can be used to optimize the influence function of a master actuator. The influence function will be similar for any size and type of mirror, i.e. the size of the peak only

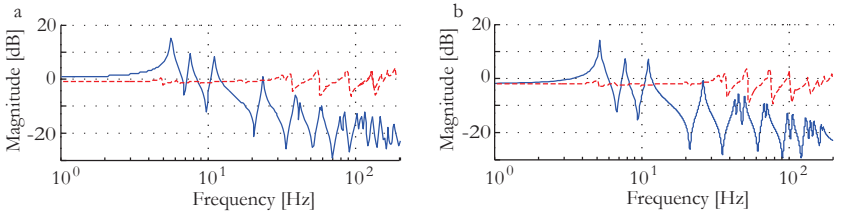

Figure 10: Frequency responses from force to position for an actuator placed 0.25 m from the center. The full curve is the response for which the input is the force at one actuator and the output is the mirror deflection at the same location. The dashed line is the frequency response, where the input is the force command to a family of 21 actuators and the output is mirror deflection at the center actuator. The curves of a) are determined with the finite element model b) with the analytical model including 35 normal modes.

depends on the relative actuator pitch and the number of actuators in the family. The concept ensures that the actuators only excite low-order modes of the plate weakly, which is particulary important, when using back sensors based upon low-cost electret microphones. The sum of the forces and moments for one family is close to zero, so the concept can be seen as an extension of Saint-Venant's principle to the dynamical case.

The analytical model can be applied for system design without use of a finite element model. In particular, the model is useful for studies of the influence of parameter variations and for determination of usable parameter space. We have shown how the parameters of mirrors with the same ratio between the outer and inner edge, affect the eigenmodes and eigenfrequencies. Mirrors with the same Poisson's ratio will have the same relative eigenmodes for the same boundary conditions. We have introduced a parameter α_k, which is the same for all such mirrors. The use of α_k makes it possible to predict how eigenfrequencies are influenced by changes of physical parameters. For instance, the effects of doubling the diameter of a deformable mirror are:

1. Eq. 11 shows that ω_0 scales with $1/r_o^2$ and Fig. 3 shows that the α_k's are close to linearly distributed for the first hundred normal modes. Thus, doubling r_o will roughly quadruple the number of of normal modes within a given bandwidth.

2. The relative actuator pitch d_a/r_o will be halved if the actuator pitch is kept the same. For a given family pattern, this will improve the quality factors, see Fig. 9.

The first effect is the dominant one, thus resulting in a more difficult system to control when increasing the diameter of the deformable mirror. The remedy, if needed, is either to increase the number of actuators within the families or to change the other physical parameters to counteract the effect from doubling r_o, according to Eq. 11.

For specific types of actuator families and using an example, we have compared results from the analytical model with those from a finite element model and found good agreement, both for eigenfrequencies, eigenmodes, frequency responses, and family

force patterns. The combined modal participation factor for an actuator family can be up to 60 times lower than the modal participation factor for a single actuator in our example. The effect is also seen in the frequency response from force to position for our example, where resonance peaks below 40 Hz have been attenuated even with a conservative 1% modal damping used in our model. This is well above the cutoff frequency for the back sensors.

References

[1] J. Beckers *NOAO proposal to NSF for 8 m telescopes* **Appendix N, Tech. Rep., NOAO** 1989

[2] F. P. Wildi, G. Brusa, M. Lloyd-Hart, L. M. Close and A. Riccardi *First light of the 6.5 m MMT adaptive optics system* **J. Proceedings of the SPIE Vol. 5169** 2003

[3] F. Quiros-Pacheco, L. Busoni, G. Aqapito, S. Esposito, E. Pinna, A. Puqlisi and A. Riccardi *First light AO (FLAO) system for LBT: performance analysis and optimization* **J. Proceedings of the SPIE Vol. 7736** 2010

[4] L. Baudouin, C. Prieur, F. Cuignard and D. Arzelier *Robust control of a bimorph mirror for adaptive optics* **Appl. Optics Vol. 47** 2008

[5] D.W. Miller and S.C. Grocott *Robust control of the Multiple Mirror Telescope adaptive secondary mirror* **Opt. Eng. Vol. 38** (1999)

[6] D. MacMynowski, R. Heimsten, T. Andersen *Distributed Force Control of Deformable Mirrors* **European Journal of Control Vol. 17** 2011

[7] R. Heimsten, D. MacMynowski and T. Andersen *Progress in Developing a Low-Cost Large Deformable Mirror* **J. Proceedings of the SPIE Vol. 7736** 2010

[8] H. M. Martin, G. Brusa Zappellini, B. Cuerden, S. M. Miller, A. Riccardi and B. K. Smith *Deformable secondary mirror for the LBT adaptive optics system* **J. Proceedings of the SPIE Vol. 6272** 2006

[9] T. Andersen, O. Garpinger, M. Owner-Petersen, F. Bjoorn, R. Svahn and A. Ardeberg *Novel concept for large deformable mirrors* **Opt. Eng. 45** 2006

[10] S.P. Timoshenko and S. Woinowsky-Krieger *Theory of Plates and Shells (2nd Ed.)* McGraw-Hill International Edititions, New York, 1959

[11] E. Ventsel and T. Krauthammer *Thin plates and shells: theory, analysis, and applications* Marcel Dekker, 2001

[12] L. Meirovitch *Analytic methods in vibrations* The Mcmillan Company, New York, 1967

[13] M. Abramowitz and I. Stegun *Handbook of Mathematical Functions with Formulas, Graphs, and Mathematical Tables* Dover Publications, New York, 1965

[14] S. Hassani *Mathematical Physics* Springer-Verlag, New York, 1999

[15] T. Ruppel, W. Osten and O. Sawodny *Model-based feedforward control of large deformable mirrors* **European Journal of Control Vol. 17** 2011

Rikard Heimsten worked on constructing and testing a picosecond LIDAR system at the Combustion Physics department at Lund University, from 2004 until 2005. He graduated in 2005 at the Faculty of Engineering at Lund University with a MSc in engineering physics. Since 2006, he has been holding a PhD research position at the Institute in Astronomy and Theoretical Physics at the Lund University. His research interests include large deformable mirrors, control systems for adaptive optics and integrated modeling.

Mette Owner-Petersen graduated in electro-physics engineering from the Technical University of Denmark (DTU) in 1967. In 1970 she received her PhD degree for the work Cyclotron resonance in Si with special regard to quantum effects in the valence band from the same university. From 1970 to 2000 she was a lecturer at the Physics Institute at DTU, teaching elementary-particle and nuclear physics, laser techniques, holography, and optics, and doing research in laser construction, Stark spectroscopy, and digital speckle interferometry. From 1991 to 1995 she worked for Nordic Telescope Group, concentrating on optical design of extremely large telescopes (ELTs) and instrumentation for the planned solar telescope LEST. Since 2000 she has held a position as lecturer at Lund Observatory, continuing her work with ELTs, and has participated in the European collaboration for a 50-m adaptive optics telescope, Euro50. The main area of her work is related to multiconjugate adaptive optics.

Thomas Ruppel worked on the Multi-Mirror-Telescope deformable mirror control systems as a DAAD scholar at the Optical Science Center in Tucson, Arizona, USA from 2006 until 2007. He received the Dipl.Ing. degree in Engineering Cybernetics from the University of Stuttgart, Germany in 2007. Since 2007, he has been holding a PhD research position at the Institute for System Dynamics at the University of Stuttgart, Germany. Currently, his main research interests include control of adaptive optics systems, control of distributed parameter systems, trajectory generation methods, and flatness based control of linear and non-linear systems.

Douglas MacMynowski is a Senior Research Associate in Control and Dynamical systems at the California Institute of Technology, where he has been involved in the design of the Thirty Meter Telescope since 2000. In addition to telescope control, his research interests span climate dynamics, flow control, and active noise control. Prior to joining Caltech, he was the Active Control Theme Leader at United Technologies Research Center. He received his PhD from M.I.T. in 1992.

Torben Andersen has a PhD in control engineering. From 1974 to 1979 he was in charge of the design of the Coud Auxiliary Telescope at European Southern Observatory in Geneva. Subsequently he worked with steerable shipborne antennas for a few years. From 1984 to 1994 he was head of engineering for the Nordic Optical Telescope Scientific Association that built the Nordic Optical Telescope on La Palma and designed the 32-m EISCAT antenna on Spitsbergen. From 1994 to 1997 he was

first head of systems engineering and later also head of telescope engineering for the VLT division of the European Southern Observatory. In 1997 he became a professor of optomechanical design at the Institute of Astronomy, Lund University, Sweden, and he is one of the architects behind Euro50, a proposed 50-m optical telescope with adaptive optics.

Paper III

Concept, Modeling and Performance Prediction of a Low-Cost, Large Deformable Mirror

Rikard Heimsten[1], Douglas G MacMynowski[2], Torben Andersen[1], Mette Owner-Petersen[1]

[1] *Lund Observatory, Lund University Box 43, SE-221 00 Lund, Sweden*

[2] *Control and Dynamical Systems, California Institute of Technology 1200 E. California Blvd., Pasadena, CA 91125*

While it is attractive to integrate a deformable mirror (DM) for adaptive optics (AO) into the telescope itself rather than using relay optics within an instrument, the resulting large DM can be expensive, particularly for extremely large telescopes. A low-cost approach for building a large DM is to use voice-coil actuators connected to the back of the deformable mirror through suction cups. Use of such inexpensive voice-coil actuators leads to a poorly damped system with many structural modes within the desired bandwidth. Control of the mirror dynamics using mechanical sensors is thus required for integration within an AO system. We introduce a distributed control approach and we show that the "inner" back sensor control loop does not need to function at low frequencies, leading to significant cost reduction for the sensors. Incorporating realistic models of low-cost actuators and sensors together with an atmospheric seeing model, we demonstrate that the low-cost mirror strategy is feasible within a closed-loop AO system.

Keywords: Adaptive optics, deformable mirror, voice-coil actuators, electret microphones, distributed local control, integrated modeling

1. Introduction

Most modern ground-based optical telescopes use adaptive optics (AO) with one or more deformable mirrors for correction of atmospheric disturbances. It is useful to include large deformable mirrors in a telescope system to avoid lossy relay optics and to make the telescope more compact [1]. Large deformable mirrors typically have either piezo-electrical (displacement) or voice-coil (force) actuators. For example, a concept including piezo-electrical actuators has been proposed for the E-ELT [2] and the 911 mm-diameter deformable secondary mirrors for the Large Binocular Telescope AO system use a concept encompassing force actuators, applied by an Italian group based at the Arcetri Astrophysical Observatory. The project team first demonstrated correct function of the deformable mirror in a laboratory environment [3], and first light on the telescope was made in 2010 [4].

Potential low-cost voice-coil actuators and position sensors have been described in [5] and are shown in Fig.1. The actuators encompass a moving rod, which is driven by a voice coil and has a linear variable differential transformer (LVDT) measuring the relative position of the rod. The rod is connected to the deformable mirror through a suction cup. Internal feedback loops in the actuators increase the bandwidth of the actuators. A system with such actuators can be inexpensive because tight tolerances are not needed. Low-cost back sensors to measure mirror deflection can be made using electret microphones in rubber bellows. However, these sensors do not respond statically, nor is it straightforward to collocate them with the actuators.

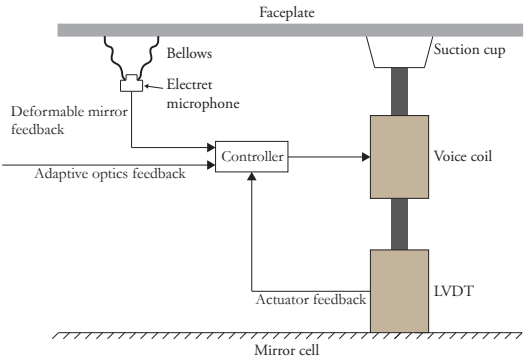

Fig. 1. Conceptual design of force actuators and position sensors. The controller is dependent on information from the three sensor feedback loops.

A distributed control approach for a thin mirror using force actuators was introduced in [6]. The control system includes rate feedback (adding damping) and position feedback (adding stiffness), similarly to [7]. However, [6] introduces two key elements: the theory needed to understand rate feedback design constraints associated with finite bandwidth, allowing sensors that are not exactly collocated with the actuators, and a robust local control scheme involving actuator families that suppresses coupling between adjacent actuators to reduce excitation of low-order eigenmodes [8]. This local approach is more robust than a global approach, because it does not rely on an accurate model.

We introduce in this paper a low-cost deformable mirror using the actuator and sensor concepts mentioned above, and demonstrate that it is feasible within an AO system. Mechanical feedback from sensors is used to compensate for the mirror dynamics using distributed control as in [6]. We show that performance within an AO system does not require sensor static information, nor actuator/sensor collocation. We use a finite element model of a test mirror as an example, and real actuator and sensor characteristics, and incorporate such a deformable mirror into a simulation of an adaptive optics system on a practical telescope. Working both in the temporal and frequency domains, we demonstrate that the mirror will fulfill the requirements for an adaptive optics system.

2. Deformable Mirror

The deformable mirror concept is shown in Fig. 1. There are voice coil actuators in a regular pattern on the back of the mirror to deform the mirror into the correct form. The back sensors are located between the actuators and operate in a frequency range of 20–5000 Hz. In a closed-loop adaptive optics system, there is also a wavefront sensor measuring the form of the mirror from DC up to a frequency determined by the sampling frequency of the wavefront sensor (typically 500 Hz).

The combination of force actuators and a thin mirror leads to a poorly damped system with many structural resonances within the desired bandwidth of the AO system. The main challenge of such a system is to establish a stable control strategy with a high bandwidth. In control terminology, the deformable mirror is the “plant” for the adaptive optics control system.

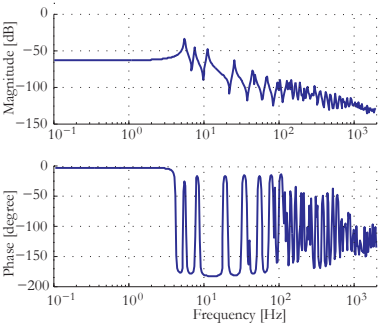

Fig. 2. Transfer function of the deformable mirror from force to position (average of four neighboring sensors) at the same location.

A typical closed-loop adaptive optics bandwidth is roughly 50 Hz, so the deformable mirror must respond to actuator commands with a relatively flat response and a small phase lag up to that frequency. However, as shown in Fig. 2, the faceplate transfer function has many resonances and anti-resonances within that frequency range. The control strategy includes rate and position feedback adding damping and stiffness, further discussed in Sec. 2.3.

2.A. Faceplate

For a case study, we use a 2 mm thick, 1 m diameter flat faceplate fixed in its center. It is made of borosilicate with the material data given in Table 1. A finite element model of the faceplate was set up with the software package "Comsol Multiphysics". The 372 actuator nodes are placed in a square topology with an actuator pitch of 45 mm as shown in Fig. 3. The 702 back sensor nodes are each located between two adjacent actuators, i.e. each actuator in general has four neighboring sensors. In addition to the actuator and sensor nodes, another 4000 nodes are used in the finite element model. The dynamic behavior of the faceplate is described by the differential equation

$$\mathbf{M}\frac{\mathrm{d}^2\boldsymbol{\xi}}{\mathrm{d}t^2} + \mathbf{E}\frac{\mathrm{d}\boldsymbol{\xi}}{\mathrm{d}t} + \mathbf{K}\boldsymbol{\xi} = \mathbf{f}$$

where $\mathbf{M}$, $\mathbf{E}$, $\mathbf{K}$ are respectively the mass, damping and stiffness matrices, $\mathbf{f}$ is a force vector and $\boldsymbol{\xi}$ is a vector of angular and translational displacements. The first eigenfrequency is at 5.6 Hz and there are another 12 eigenfrequencies below 50 Hz, i.e. within the expected bandwidth for an adaptive optics system.

Guyan reduction and modal truncation were used to obtain a more computationally practical model. Guyan reduction reduced the number degrees of freedom for each node to three, retaining out-of plane translation and the two rotations around the in-plane axes. Modal truncation removed the modes with eigenfrequencies above 10 kHz. Mode acceleration was applied to include the static contribution from the modes omitted by the truncation.

Structural performance of the faceplate, represented by the transfer function from force to position at one location as shown in Fig. 2, can be understood from a wave-based description. Resonances arise due to constructive interference of the bending waves reflecting off the faceplate boundaries. Above a certain frequency, the response is no longer dominated by sharp resonance and anti-resonance peaks, because many

Parameter	Definition	Value
E	Young's modulus	$63{\times}10^9$ Pa
ρ	density	2.23×10^3 kg/m^3
ν	Poisson ratio	0.2
h	DM thickness	2 mm
D	bending stiffness	$Eh^3/12(1-\nu^2)$
r	radius of the mirror	0.5 m
A	DM area	πr^2
ζ	damping ratio	1%

Table 1. Nomenclature and parameter values for a 1 m deformable mirror used for performance studies.

different modes overlap. The transition to this "acoustic" region begins where the half-power bandwidth of a mode exceeds the average modal spacing by a factor of two or three, at a frequency [6] of

$$f_{\mathrm{ac}} = 2\sqrt{\frac{D}{\rho h}}\frac{1}{A\zeta} \tag{1}$$

where the nomenclature is defined in Table 1. For example, for a deformable mirror of borosilicate with a diameter of 1 m and a thickness of 2 mm, the transition frequency is about 1300 Hz.

Use of a non-collocated sensor and actuator scheme gives rise to phase lag, which is tolerable as long as the distance between the actuators and sensors is no more than [6]

$$d < \frac{c_{\mathrm{B}}}{8 f_{\mathrm{ac}}}$$

where c_{B} is the bending wave speed in the plate and f_{ac} is given by Eq. 1.

2.B. Actuators and Sensors

The dynamical behavior of the actuators and the sensors can be represented by state-space models. The equation of motion for an actuator in the Laplace domain is given by

$$F = (ms^2 + es + k)\delta_{\mathrm{r}}$$

where m is the mass and δ_{r} the position of the moving rod, and F is the electromagnetic force developed by the voice coil, which is the product of its *force constant* and the current in the winding. The suction cup can be viewed as a spring with stiffness k and damping coefficient e. A local current loop can be added to suppress the influence of the inductance and back electromotive force of the voice coil. Thus, we can assume that the current is proportional to an input voltage, U, and the transfer function from voltage to rod displacement is

$$\frac{\delta_{\mathrm{r}}}{U} = \frac{C}{ms^2 + es + gC + k} \tag{2}$$

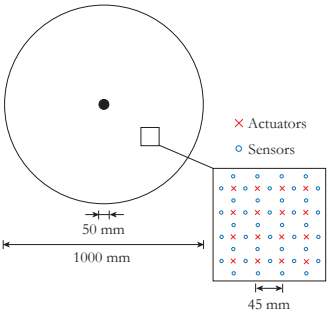

Fig. 3. The topology of the actuator and sensor positions for the 1 m case study.

where g is the proportional gain of the local feedback loop from the LVDT and C is a design dependent constant. The natural frequency, ω_a, and the damping, ζ_a, of the second-order system in Eq. 2 is:

$$\begin{aligned} \omega_\mathrm{a} &= \sqrt{\tfrac{gC+k}{m}} \\ \zeta_\mathrm{a} &= \tfrac{e}{2\sqrt{m(gC+k)}} \end{aligned}$$

Choosing appropriate scaling we can let $C = 1$. A state-space realization of Eq. 2 is given by

$$\begin{aligned} \mathbf{A}_\mathrm{a} &= \begin{bmatrix} -2\zeta_\mathrm{a}\omega_\mathrm{a} & -\omega_\mathrm{a}^2 \\ 1 & 0 \end{bmatrix} \qquad \mathbf{B}_\mathrm{a} = \begin{bmatrix} \omega_\mathrm{a}^2 \\ 0 \end{bmatrix} \\ \mathbf{C}_\mathrm{a} &= \begin{bmatrix} 0 & 1 \end{bmatrix} \qquad \mathbf{D}_\mathrm{a} = 0 \end{aligned}$$

The sensors on the back of the mirror, shown in Fig. 1, encompass electret microphones inside bellows. Such a sensor can be viewed as a pressure sensor with a flat region of the frequency response between the low-pass cutoff, ω_lp and the high-pass cutoff, ω_hp. The transfer function is given by

$$H_\mathrm{sen}(s) = \frac{s}{s+\omega_\mathrm{hp}} \cdot \frac{\omega_\mathrm{lp}}{s+\omega_\mathrm{lp}}$$

We here neglect scaling factors. The equation can be converted to state-space form:

$$\begin{aligned} \mathbf{A}_\mathrm{s} &= \begin{bmatrix} 0 & -\omega_\mathrm{hp}\omega_\mathrm{lp} \\ 1 & -\omega_\mathrm{hp} - \omega_\mathrm{lp} \end{bmatrix} \qquad \mathbf{B}_\mathrm{s} = \begin{bmatrix} 0 \\ \omega_\mathrm{lp} \end{bmatrix} \\ \mathbf{C}_\mathrm{s} &= \begin{bmatrix} 0 & 1 \end{bmatrix} \qquad \mathbf{D}_\mathrm{s} = 0 \end{aligned}$$

The corner frequencies are 20 Hz and 5 kHz for our design [5].

The electret microphones can detect a pressure change, Δp, of around 0.2 Pa. The corresponding volume change is computed from

$$\Delta v = \frac{v\Delta p}{1.4p}$$

obtained by differentiation of the state equation for an adiabatic ideal gas, where p is the ambient pressure. Assuming no dynamics in the bellows between the corner frequencies, the volume change is proportional to

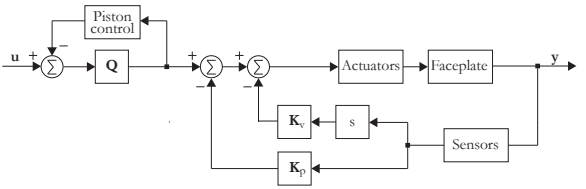

Fig. 4. Block diagram of the deformable mirror system. The actuator, faceplate and sensor modules represent the state-space models derived in Sec. 2.1-2.2.

the deflection of the mirror. With the dimensions chosen, the electret microphones can sense a deflection of about 10 nm.

2.C. Faceplate Control

The deformable mirror system is shown in Fig. 4. The three blocks "Actuators", "Faceplate" and "Sensors" represent the state-space models for these mechanical parts. The gains of the position and rate feedback loops are represented by the diagonal matrices $\mathbf{K}_\mathrm{p}$ and $\mathbf{K}_\mathrm{v}$, respectively. A differentiator is used for the rate feedback, since the electret microphones are position sensors. The piston control is required to reduce excessive stresses at the attachment points of the faceplate.

A force command to one actuator produce a global response, similar to the tip/tilt mode, for the whole mirror. The loop gain of the faceplate is about 30 times higher for low spatial than for high spatial frequencies. The substantial coupling between actuators is reduced by the matrix $\mathbf{Q}$, shown in Fig. 4. It is in principle possible to obtain $\mathbf{Q}$ by inverting the faceplate model, but the system may not be robust if the plant is not modeled with high accuracy [6]. We instead propose a local scheme, using a set of actuator families, each centered on an actuator. A desired displacement command (input to $\mathbf{Q}$ in Fig. 4) at a particular actuator location results in a force distribution applied to all the actuators in that family. The force distribution in each family is determined by minimizing the cost function

$$J = \|\mathbf{K}_\mathrm{a}^{-1}\mathbf{f} - \boldsymbol{\xi}\| \tag{3}$$

where $\mathbf{f}$ is the force vector for the actuator nodes and $\boldsymbol{\xi}$ is a vector defining the desired displacements at the actuator nodes, defined below. A static condensation of the full stiffness matrix is used to form $\mathbf{K}_\mathrm{a}$, which then only retains the out-of-plane translation degrees of freedom for the actuator nodes. The elements of the force vector $\mathbf{f}$, in Eq. 3 are constrained to be

$$\begin{aligned} f_i &= 0 \quad \text{for} \quad i \notin \text{family} \\ f_i &\in \mathbb{R} \quad \text{for} \quad i \in \text{family} \end{aligned}$$

where i is the actuator number. The elements of the displacement vector, $\boldsymbol{\xi}$, for a family centered on the j-th actuator are

$$\begin{aligned} \xi_i &= 0 \quad \text{for} \quad i \neq j \\ \xi_i &= 1 \quad \text{for} \quad i = j \end{aligned}$$

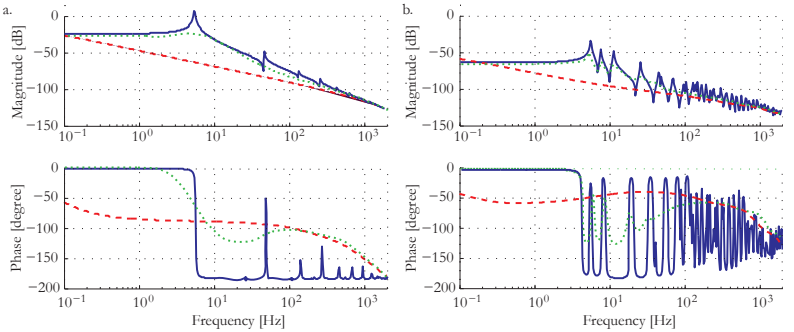

Fig. 5. Transfer functions for (a) Case 1 (global), and (b) Case 2 (local). See text for case descriptions. The solid line shows the faceplate dynamics when $\mathbf{K}_v$ and $\mathbf{K}_p$ are null matrices and $\mathbf{Q}$ an identity matrix. The dashed line illustrates the same situation, however with closed rate feedback, $\mathbf{K}_v$, and ideal sensors, whereas the dotted curve is for non-ideal sensors. The conclusion is that the back-sensors do not need to have bandwidth down to zero frequency.

Using this approach, the computed force vectors for each family are stored as columns in the family matrix $\mathbf{Q}$. Each column corresponds to a command vector for a specific center actuator. We have chosen a family size with two rings of actuators around the centered actuator, in total 21 actuators.

A comparison between use of a single actuator and a family centered on the same actuator can be made by studying the influence functions for the two cases. The influence function for a single actuator is largely dominated by a tip/tilt shape (the lowest frequency, most compliant mode of the faceplate), whereas the influence function for the family essentially is a local deformation at the center actuator of the family.

To further demonstrate the properties of the control system with the family concept, we use the faceplate model introduced in Sec. 2.A as an example. In this study, piston control is not included. To study the dynamical behavior of the system, we compute frequency responses for two cases:

- Case 1: The input command vector, $\mathbf{u}$, of Fig. 4 is a pure tip and its magnitude at a representative location is taken as scalar input, and the output is the displacement measured at the same location. The objective is to study low spatial frequency behavior.

- Case 2: The input command vector, $\mathbf{u}$, has all zeros except at a representative location. The magnitude of the input at that location is then the scalar input, and the output is the displacement at the same location. The objective is to study high spatial frequency behavior.

The frequency response of the mirror alone, i.e. when $\mathbf{K}_\mathrm{v}$ and $\mathbf{K}_\mathrm{p}$ of Fig. 4 are null matrices and $\mathbf{Q}$ an identity matrix, are shown as solid curves in Fig. 5. As expected, the first eigenfrequency at 5.6 Hz corresponds to the tip/tilt mode and is seen both for Case 1 and 2. Closing the rate feedback loops with a diagonal $\mathbf{K}_v$ matrix and ideal sensors gives the dashed lines in Fig. 5. The system is over-damped at lower frequencies for the gain needed to damp eigenfrequencies up to the acoustic frequency. With non-ideal sensors there is hardly any over-damping, since their response drops off below 20 Hz. The transfer function of the system with closed rate feedback and non-ideal sensors is shown as dotted curves in Fig. 5.

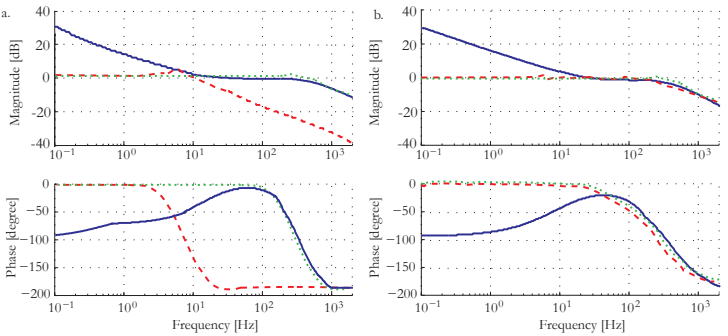

Fig. 6. Frequency responses for (a) Case 1 (global), and (b) Case 2 (local). The dashed curves show the effect of the family matrix. The magnitude difference (seen in Fig. 5) is no longer present. The dotted curves show the dynamical behavior of the faceplate when the position feedback is closed with ideal sensors. The low-order eigenmodes are shifted towards higher frequencies and the dynamical behavior is similar for the two cases. The solid curves show the frequency responses, when non-ideal sensors are used. The controlled deformable mirror has similar dynamic behavior for different spatial frequencies.

Including the family matrix, $\mathbf{Q}$, in the control system has two effects. Besides decoupling adjacent actuators from each other, eigenmodes with eigenfrequencies below 30 Hz are much less excited by input commands when $\mathbf{Q}$ is included. The second effect is important since the low-order eigenfrequencies in Fig. 5b (dotted curve) are not as well damped.

We continue by looking at the features of the position feedback and the family matrix, with the starting point from the dotted curves in Fig. 5. The magnitude difference of about 30 dB between the cases is suppressed by the family matrix, shown as the dashed curves in Fig. 6. Also, the low-frequency eigenmodes still present in the high spatial frequency case are attenuated. However, while the low and high spatial frequencies now have similar static gain, the low spatial frequency resonances are below the desired AO bandwidth. This is corrected by adding stiffness through the position feedback. To illustrate the effect of the position feedback clearly, the dotted curves in Fig. 6 show the closed-loop performance with ideal sensors. The dynamic behavior is now similar for both cases. Finally, the solid curves include the effect of the non-ideal sensors. The roll off behavior of the sensors below 20 Hz give rise to low-frequency asymptotes in the closed-loop response. The solid curves show the dynamical behavior of the deformable mirror system.

One final detail is that piston is unobservable by the wavefront sensor in an adaptive optics system, and some piston control is needed to alleviate unnecessary stress that can slowly build up at the fixed inner rim of the deformable mirror. A better solution than driving the piston to zero is to subtract the mean force of the actuators closest to the rim from the displacement command at every location with some small gain; this additional feedback loop is shown in Fig. 4.

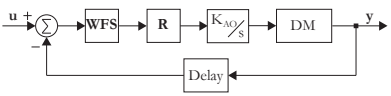

Fig. 7. Block diagram of the adaptive optics loop. The loop is closed with an integral controller.

3. Adaptive Optics Control System

With the control architecture for the inner loop of the deformable mirror described in Sec. 2, we now introduce the outer adaptive optics loop, including wavefront sensing. The dynamic response of the deformable mirror system, shown as the solid lines in Fig. 6, is not the same as that of a typical deformable mirror, but we demonstrate that it is sufficient for the purpose. The feedback control used for the adaptive optics system is shown in Fig. 7, where the plant is the deformable mirror system with the closed position and rate feedback loops as described above and shown in Fig. 4, and the input is the commanded displacement. The adaptive optics loop is closed with integral control, represented by the $\mathbf{K}_{\mathrm{AO}}/\mathrm{s}$ block in Fig. 7.

The WFS-block in Fig. 7 is a matrix representing a Shack-Hartmann wavefront sensor with a square 22x22 lenslet array. The lenslet array is aligned such that the corners of the grid coincide with the actuator locations, see Fig. 8. Since the lenslet array map is larger than the deformable mirror, a mask is used to remove 88 subapertures. The four subapertures in the center are omitted since, a pure piston displacement of the deformable mirror would give a non-zero wavefront sensor reading for the four subapertures in the center due to the inner boundary conditions. The tip and tilt for each remaining subaperture are computed from the wavefront samples at the actuator locations [11]

$$tip = \frac{w(\mathbf{p}_1) + w(\mathbf{p}_2) - w(\mathbf{p}_3) - w(\mathbf{p}_4)}{2}$$
$$tilt = \frac{w(\mathbf{p}_1) + w(\mathbf{p}_3) - w(\mathbf{p}_2) - w(\mathbf{p}_4)}{2}$$

where the two-dimensional vectors $\mathbf{p}_1$, $\mathbf{p}_2$, $\mathbf{p}_3$ and $\mathbf{p}_4$ define the locations of the four corner points of a subaperture and $w(\mathbf{p})$ is the displacement.

The R-block in Fig. 7 is the reconstructor matrix, which is used for computation of DM displacement commands from the tip and tilt values of the WFS-matrix. The reconstructor is assembled using singular value decomposition of the interaction matrix, i.e. the matrix which describes the tip and tilt of the wavefront over the subapertures, when poking each DM displacement individually.

The performance of the adaptive optics loop is limited by the phase lag introduced by wavefront sampling and represented by the delay block in the control loop in Fig. 7. The delay is modeled as a fifth order Padé approximation of e^{-sT}, where T is the delay time. Half the delay is from the wavefront sensor sampling period and half from the zero order hold. The closed-loop performance and the rejection plot of the system in Fig. 7, from ϕ_{in} to ϕ_{res} at a representative location is seen in Fig. 9 for $T = 1\,ms$. The two cases (described in Sec. 2.3) represent the lowest and highest spatial frequencies that the deformable mirror can achieve. The difference between our deformable mirror system and an idealized DM (with a uniform behavior for all spatial frequencies and a flat frequency response) include the small difference between the spatial frequencies, an increase in low-frequency gain and some additional phase lag at higher frequencies. The latter would become a significant factor for desired AO bandwidths above 100 Hz.

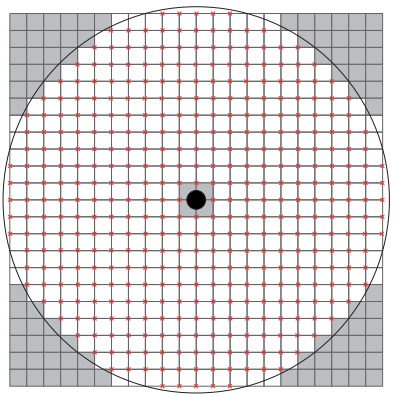

Fig. 8. The lenslet array grid over the deformable mirror. Lenslet which are not completely filled by the light beam, are not taken into account. Actuator locations are marked by crosses.

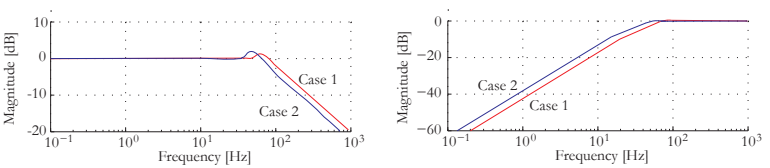

Fig. 9. The closed-loop frequency response (to the left) and the rejection plot (to the right) of the system shown in Fig. 7, from ϕ_{in} to ϕ_{res} for a representative location. The two cases represent the the lowest and highest spatial frequencies that the deformable mirror can achieve.

4. Influence of Atmosphere

Our proposed large deformable mirror concept, described in Sec. 2 and 3, is studied in close-loop adaptive optics operation. As an example for our study, we assume that the deformable mirror already introduced is the secondary in a two-mirror, 30 m telescope with adaptive optics. The observing wavelength is assumed to be 2200 nm. A three layer atmosphere model is used with parameters taken from a study of the atmosphere over the La Palma observatory [10] as given in Table 2. The altitude of the atmospheric layers are not of importance since only objects at zenith are considered and the field is small. There are 20 actuators across the deformable mirror with an actuator pitch of 45 mm, thus the actuator pitch matches the Fried parameter of the first atmospheric layer.

Layer	Fried's parameter	Wind speed
1	1.48	12 m/s
2	4.21	18.6 m/s
3	6.96	8 m/s

Table 2. The parameters of the atmosphere for λ =2200 nm at La Palma [10].

A thin-layer model of the atmosphere is used with near-field propagation. Assuming Kolmogorov turbulence, the two-dimensional power spectrum of the phase is given by [11]

$$P_{\text{atm}}(\vec{f}) = \frac{0.0229}{r_0^{5/3} f^{11/3}} \tag{4}$$

where r_0 is the Fried parameter and f is the magnitude of the spatial frequency vector $\vec{f}$.

We now evaluate the AO performance in both the temporal and the frequency domain.

4.A. Performance for Different Zernike Polynomials

The adaptive optics system is null-seeking and it is the task of the system to suppress input disturbance from the atmosphere to the extent possible. It is useful to expand the atmospheric phase into series of Zernike polynomials. The power spectra for the individual Zernike polynomials, $P(\vec{f})$, can be computed from the power spectrum of the atmospheric turbulence as [12]

$$P(\vec{f}) = |M(\vec{f})|^2 P_{\text{atm}}(\vec{f}) \tag{5}$$

where $M(\vec{f})$ is the Fourier transform of a specific Zernike polynomial. The Fourier transform of the Zernike polynomials is given by [13]

$$|M(\vec{f})| = \sqrt{n+1}\frac{2|J_{n+1}(\pi D_{\text{DM}} f)|}{\pi D_{\text{DM}} f} \times \begin{cases} \sqrt{2}|\cos(m\theta)| & \text{for } m \neq 0 \\ \sqrt{2}|\sin(m\theta)| & \text{for } m \neq 0 \\ 1 & m = 0 \end{cases}$$

where n is the radial degree, m the the azimuthal frequency of the polynomial, D_{DM} the diameter of the deformable mirror and $J_k(x)$ is the Bessel function of the first kind of the order k. Assuming frozen turbulence

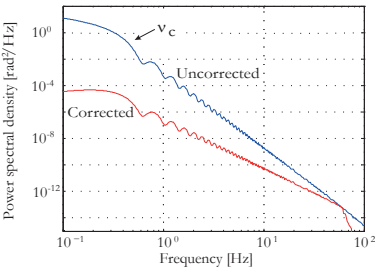

Fig. 10. Temporal power spectra of the uncorrected and the corrected tilt term.

approximation, i.e. the phase screen shape remains unchanged when translated at the wind velocity V, the spatial power spectrum can be related to the temporal power spectrum as [12]

$$W(\nu) = \frac{1}{V}\int_{-\infty}^{+\infty} P\left(\frac{\nu}{V}, f_y\right) \mathrm{d}f_y$$

Here, $\nu = V f_x$ is the temporal frequency. Using Eq. 4 and 5, the temporal power spectrum at the deformable mirror is given by

$$W_{\mathrm{in}}(\nu) = \frac{0.0299}{V_{\mathrm{DM}} r_{0,\mathrm{DM}}^{5/3}} \int_{-\infty}^{+\infty} \left(\left(\frac{\nu}{V_{\mathrm{DM}}}\right)^2 + f_y^2\right)^{-11/6} \left| M\left(\frac{\nu}{V_{\mathrm{DM}}}, f_y\right)\right|^2 \mathrm{d}f_y \tag{6}$$

where the wind speed and Fried's parameter have been scaled to the deformable secondary mirror. For our test case, the diameter of the telescope entrance pupil is 30 m and the diameter of the deformable mirror is 1 m, so the scaling becomes $r_{0,\mathrm{DM}} = \frac{1}{30} r_0$ and $V_{\mathrm{DM}} = \frac{1}{30} V$. Note that only the first layer of the atmosphere in Table 2 is considered here.

The full adaptive optics system, described in Sections 2-3, is null seeking. The disturbance for each Zernike polynomial is added through Eq. 6. The residual power spectrum is

$$W_{\mathrm{out}}(\nu) = |H(\nu)|^2 W_{\mathrm{in}}(\nu)$$

where $H(\nu)$ is the system rejection transfer function, shown in Fig. 9. The power spectra for the uncorrected and the corrected tilt mode of the atmosphere are shown in Fig. 10. The Zernike spectra are characterized by a cutoff frequency [12]

$$\nu_{\mathrm{c}} = 0.3(n+1)\frac{V}{D}$$

where n is the radial order of the Zernike component.

The areas under the power spectra in Fig. 10, give the variance of the phase. The contribution of each Zernike mode then can be computed and the result is shown in Fig. 11a. The root mean square value of the wavefront for the first 25 Zernike modes is normalized with respect to the uncorrected tilt mode. The suppression of the Zernike modes, i.e. the residual divided by the input disturbances, is shown in Fig. 11b.

The root mean square error for Zernike modes with Kolmogorov turbulence is described by Noll [13] as $\sigma^2 = 1.0299(D/r_o)^{5/3}$. The mean-square residuals are suppressed by a factor of about 700 (root mean square reduction of 26). Thus, using Maréchal's approximation, the Strehl ratio is 0.8 for our case.

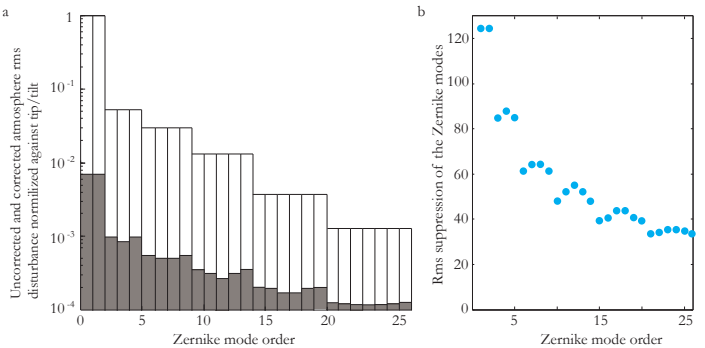

Fig. 11. a) Contribution of each Zernike mode to the uncorrected and corrected atmospheric rms disturbance normalized with respect to the tip/tilt mode before correction; empty bars refer to the uncorrected, whereas filled bars refer to the corrected case. b) Suppression factors for the rms wavefront errors of the lowest 25 Zernike components of the atmospheric phase noise.

4.B. Atmospheric modeling

A time-domain simulation of the full system, shown in Fig. 7, with an atmosphere model as input, ϕ_{in}, is used to demonstrate feasibility. The atmospheric disturbance model used is the three-layered atmosphere given in Table 2. The phase contributions from the different layers are assumed uncorrelated and the net phase is the sum over the three layers, with frozen turbulence assumed. The layers obey Kolmogorov statistics given by Eq. 4.

A phase screen describes the phase difference added to a wavefront, when passing through a thin turbulent layer. Linear propagation through the screen is assumed, i.e. refraction is neglected. A phase screen, $\varphi(\mathbf{r})$, is composed by filtering a random function, $J(\boldsymbol{f})$, with the square root of the power spectrum of the two-dimensional phase, $W_{\text{in}}(\boldsymbol{f})$,

$$\varphi(\mathbf{r}) = \mathcal{F}^{-1}\left(\sqrt{W_{\text{in}}(\boldsymbol{f})}J(\boldsymbol{f})\right) \tag{7}$$

which is a method introduced by McGlamery [15].

A fourth-order Runge-Kutta method is used with fixed integration interval of 50 µs. The sampling periods of the phase screens and the wavefront sensor are 1 ms and 2 ms, respectively. Linear interpolation is used to update the phase screen during a sampling period.

A result from a three second simulation is shown in Fig. 12. The two zooms show, respectively the initial transient response of the mirror, when it is commanded from its rest position, and a 14 ms window illustrating the typical behavior of the mirror during operation. The Strehl ratio is computed using Maréchal's approximation for all nodes across the mirror. If the performance during the start-up transient is not considered, the average Strehl ratio is 0.77. The start-up transient has a duration of 0.1 s due to actuator saturation. Further, the effect of temporal WFS sampling is apparent in the right zoom of Fig. 12.

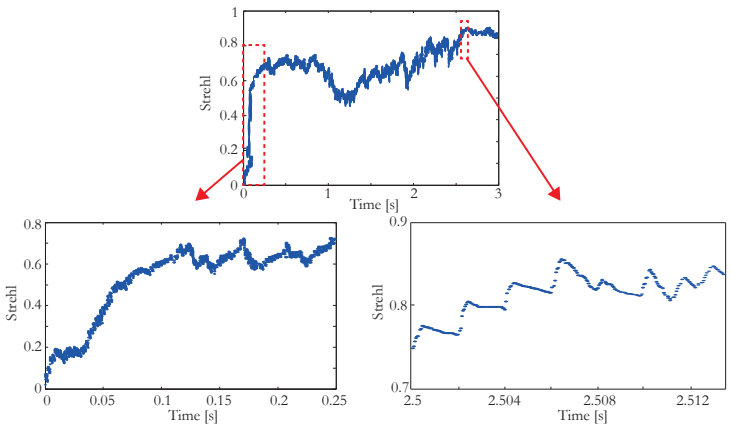

Fig. 12. A three second time-domain simulation, where the Strehl ratio is computed for each time point. The zoom windows show the start-up transient of the system from its rest position and a representative operation time interval, respectively.

5. Conclusions

We have demonstrated feasibility of a low-cost concept for a large deformable mirror for adaptive optics. Use of voice-coil (force) actuators results in a lightly-damped mirror with many structural modes within the AO control bandwidth, resulting in the need for feedback from mechanical sensors to obtain dynamic response sufficient for AO. However, inexpensive mechanical sensors can be used because precision is not required quasi-statically, nor do the sensors need to be collocated with the actuators to provide active damping. The control system includes rate feedback to add damping, and a local family approach to suppress crosstalk between adjacent actuators. The latter ensures that the mirror has similar dynamic behavior for all the spatial frequencies that can be introduced by the actuators. Compared to an idealized DM, our concept will appear similar inside an AO system for desired AO bandwidths of 100 Hz or below. If a higher AO bandwidth is required, the bandwidth of the actuators must be increased.

Performance predication of the low-cost DM system has been simulated within an AO system. Atmospheric turbulence was included both using a Zernike polynomial expansion of the atmosphere and using a time-domain simulation showing the fluctuation of the Strehl ratio over time. The simulation, including a three-layer atmosphere, gave an average Strehl ratio of 0.77. This agrees well with the analytic approach, from which the Strehl ratio is determined to be 0.8.

With low-cost sensors and actuators, the dynamic behavior of the deformable mirror is not the same as that of a typical DM, but we have demonstrated that it provides good performance within an adaptive optics system.

References

1. J. Beckers, “NOAO proposal to NSF for 8 m telescopes,” Appendix N, Tech. Rep., NOAO 1989

2. B. Crepy, S. Chaillot, M. Cola, J. M. Conan, R. Cousty, M. Dimmler, J. L. Dournaux, S. De Zotti, E. Gabriel, R. Gasmi, R. Grasser, N. Hubin, P. Jagourel, L. Jochum, F. Locre, P-Y. Madec, P. Morin, M. Mueller, G. Petit, D. Petitga, J. J. Roland, J. C. Sinquin and E Vernet, "Demonstration prototype and breadboards of the piezo stack M4 adaptive unit of the E-ELT," Proc. SPIE **7736** 2010
3. A. Riccardi, M. Xompero, D. Zanotti, L. Busoni, C. Del Vecchio, P. Salinari, P. Ranfagni, G. Brusa Zappellini, R. Biasi, M. Andrighettoni, D. Gallieni, E. Anaclerio, H. M. Martin and M.S. Miller, "The adaptive secondary mirror for Large Binocular Telescope: results of acceptance laboratory test," Proc. of the SPIE **5169** 2008
4. F. Quiros-Pacheco, L. Busoni, G. Aqapito, S. Esposito, E. Pinna, A. Puqlisi and A. Riccardi "First light AO (FLAO) system for LBT: performance analysis and optimization," J. Proceedings of the SPIE **7736** 2010
5. T. Andersen, O. Garpinger, M. Owner-Petersen, F. Bjoorn, R. Svahn and A. Ardeberg, "Novel concept for large deformable mirrors," Opt. Eng. **45** 2006
6. D.G. MacMynowski, R. Heimsten and T. Andersen, "Distributed Force Control of Deformable Mirrors," European Journal of Control **17** 2011
7. H. M. Martin, G. Brusa Zappellini, B. Cuerden, S. M. Miller, A. Riccardi and B. K. Smith, "Deformable secondary mirror for the LBT adaptive optics system," Proc. SPIE **6272** 2006
8. R. Heimsten, M. Owner-Petersen, T. Ruppel, D.G. MacMynowski and T. Andersen, "Suppressing Low-Order Eigenmodes with Local Control for Deformable Mirrors," Optical Engineering, In Press
9. A. Preumont, *Vibration Control of Active Structures*, Springer 2002
10. C. Muoz-Tuon and J. Vernin, "Private communication."
11. J. W. Hardy, *Adaptive Optics for Astronomical Telescopes*, Oxford University Press 1998
12. JM. Conan, G. Rousset and PY. Madec, "Wave-front temporal spectra in high-resolution imaging through turbulence," J. Opt. Soc. Am. A **12** 1995
13. R. J. Noll, "Zernike polynomials and atmorspheric turbulence," J. Opt. Soc. Am. **66** 1976
14. F. Roddier, M. J. Northcott, J. E. Graves and D. L. McKenna, "One-dimensional spectra of turbulence-induced Zernike aberrations: time-delay and isoplanicity error in partial adaptive compensation," J. Opt. Soc. of Am. **10** 1993
15. B. L. McGlamery, "Computer simulation studies of compensation of turbulence degraded images", Proc. SPIE **76** 1976

Paper IV

Integrated Modeling of a Laboratory Setup for a Large Deformable Mirror

Rikard Heimsten[a], Torben Andersen[a], Mette Owner-Petersen[a] and Douglas G MacMynowski[b]

[a]Lund Observatory, Lund University Box 43 SE-221 00 Lund, Sweden

[b] Control and Dynamical Systems, California Institute of Technology 1200 E. California Blvd., Pasadena, CA 91125, USA

ABSTRACT

We study a concept for a low-cost, large deformable mirror for an Extremely Large Telescope. The use of inexpensive voice-coil actuators leads to a poorly damped faceplate, with many modes within the desired control bandwidth. A control architecture, including rate and position feedback to add damping and stiffness, for the faceplate has been presented in our previous papers. An innovative local control scheme which decouples adjacent actuators and suppresses low-order eigenmodes is a key feature in our controller. Here, we present an integrated model of a partially illuminated large deformable mirror in an experimental laboratory setup with a limited amount of actuators. From the model, conclusions are drawn regarding the number of actuators needed to identify the key features, such as local control performance, dynamic range, and controllability and robustness of the deformable mirror.

Keywords: Adaptive optics, deformable mirror, distributed control, active damping, local control.

1. INTRODUCTION

Adaptive optics is a technology for real-time correction of rapidly changing optical distortions. It is used in astronomical telescopes and laser communication systems to remove the effects of wavefront distortions induced by the atmospheric turbulence, and in retinal imaging system to reduce optical aberrations from the eye. Future adaptive optics systems design for Extremely Large Telescopes will have a pre-focus large deformable mirror as the correcting element. The first large deformable mirror was a 642 mm wide and 2 mm thick continuous face-sheet deformable mirror for the Multi Mirror Telescope (MMT)[1]. New deformable mirrors with diameters of around 1000 mm are built for e.g. the Large Binocular Telescope (LBT)[2] and the Very Large Telescope (VLT)[3]. Thousands of actuators control the form of the deformable mirror. Actuation can be done with either force (voice-coil) or position (typically piezoelectrical) actuators. Force actuation, in comparison to position actuation, is affected by the dynamical behavior of the structure of the deformable mirror, requiring a more complex control system. However, voice-coil actuators allow large strokes and the system can be built at a lower cost.

The present paper is the third paper in a series on a low-cost large deformable mirror concept. In the first paper[4], we presented a control system for a deformable mirror with inexpensive voice-coil actuators (with a limited bandwidth of 2-3 kHz) and collocated back sensors. Controllability can be achieved, since a structure with non-zero damping will have a frequency, at which the half-power bandwidth of the resonant mode will exceed the modal spacing by a sufficient factor. Above this frequency, the transfer function from force to position for the structure is relatively smooth in both magnitude and phase. The region in which this occurs for a 1000 mm wide and 2 mm thick mirror is around 1-2 kHz, depending on the material properties. It is sufficient to add damping up to this point, which makes the use of the inexpensive actuators possible. Electret microphones inside bellows are suggested as position sensors. The drawback is that the frequency response of the microphones rolls off below 20 Hz[5]. In the second paper[6], we added the dynamics of the actuators and the sensors to the model. The use of local control to reduce the global response to a local error, ensures that an actuation does not invoke any of the eigenmodes below 20 Hz (in the region where the microphones perform poorly)[8]. Further, we made a study, which showed that the deformable mirror concept can give good performance when used in adaptive optics to compensate for atmospheric turbulence.

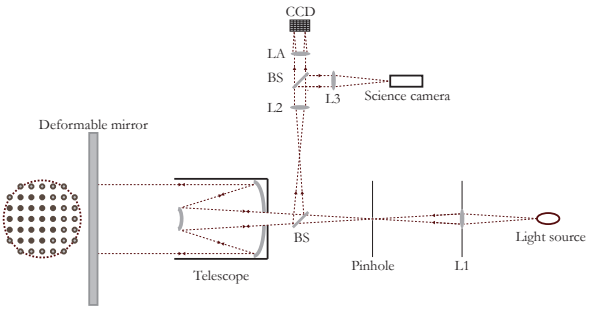

Figure 1. The optical layout of the experiment. The three components L1, L2 and L3 are a lenses, the two BS components are beam splitters and the LA component is a lenslet array.

The structure of this paper is as follows: In Sec. 2, an experimental laboratory setup is presented. The setup is based upon the available components; A Celestron C14 telescope and a SciMeasure's LJ CCD39 detector. These two components limits the possibility to control and image light from a large deformable mirror. Thus, we suggest using a partially illuminated and imaged part of a large deformable mirror as a first experiment, which still enables the possibility to identify key parameters such as controllability and performance of the local controller. In Sec. 3, the plate module is described and the control of the plate is presented, including electrical damping and stiffness feedbacks, and local control to suppress cross-talk between adjacent actuators. In Sec. 4, the full integrated model is described, encompassing the control system, the plate module, the adaptive optics module, and the dynamics of the actuators and sensors. In Sec. 5, we present the results from use of the model related to the possibility to draw conclusions regarding the low-cost deformable mirror concept from the suggested experiment.

2. OPTICAL DESIGN OF THE EXPERIMENT

This chapter presents a proposed optical design for the experiment. The design has taken into account the components available; the Celestron C14 telescope and the SciMeasure's LJ CCD39 detector. The Celestron has a Schmidt-Cassegrain design, with a focal ratio of F/11.2. The format of the detector is 80 x 80 pixels with a pixel width $\Delta_{\text{pix}} = 24\,\mu\text{m}$.

The optical layout of the experiment is shown in Fig. 1. The telescope is used to both illuminate and image light from a part of the deformable mirror. Actuators, in total 45, are placed in a Cartesian topology with an actuator pitch, $d_{\text{act}} = 50\,\text{mm}$, at the back of the illuminated part of the deformable mirror.

The entrance pupil of the telescope is imaged onto the lenslet array by a collimating lens, which is placed behind the focus point of the telescope at a distance that matches the focal length of the lens. The focal length should be chosen according to

$$f_{\text{L2}} = \frac{D_{\text{LA}}}{D_{\text{tel}}} f_{\text{tel}}$$

when there is one subimage per actuator and N_{pix} is the number of pixels per subimage. The next component, after the collimator, in the optical train is a beam splitter which divides the light to the science camera arm and the wavefront sensing arm. The diameter and the focal length of the lenslets in the lenslet array should be chosen according to

$$D_{\text{LL}} = \sqrt{N_{\text{pix}}}\Delta_{\text{pix}}$$
$$f_{\text{LL}} \approx \frac{2\Delta_{\text{pix}} D_{\text{LL}}}{\lambda}$$

Parameter	Definition	Value
d_{dm}	Deformable mirror diameter	1 m
d_{act}	Actuator pitch	50 mm
D_{tel}	Telescope entrance aperture	356 mm
f_{tel}	Focal length of telescope	3987 mm
Δ_{pix}	Pixel width	24 μm
N_{pix}	Number of pixels per subaperture	100
f_{L2}	Focal length of lens L2	21 mm
D_{LL}	Pitch of one lenslet	240 μm (250 μm)
f_{LL}	Focal length of the lenslets	15 mm (18 mm)
δ_{stroke}	Stroke difference between adjacent actuators	1.6 μm
D_{PH}	Diameter of the pinhole	14 μm

Table 1. Nomenclature and parameter values for the setup. The values in parenthesis for D_{LL} and f_{LL} are for a standard lenslet array from Adaptive Optics Associates.

where the diffraction limited spot in the focal plan of the lenslets covers four pixels. The focal length of the lenslets also affects the maximum allowed stroke difference between two adjacent actuators. The maximum gradient of the wavefront measured over a lenslet, which can be detected, is given by $\alpha_{\mathrm{LL}}(x) = \sqrt{N_{\mathrm{pix}}}\Delta_{\mathrm{pix}}/f_{\mathrm{LL}}$. The magnitude shift of the gradient between the lenslet array and the telescope is given by $\alpha_{\mathrm{LA}} = \alpha_{tel} f_{\mathrm{tel}}/f_{\mathrm{L2}}$. Thus, the maximum allowed stroke difference can be approximated as

$$\delta_{\mathrm{stroke}} = \frac{d_{\mathrm{act}}\sqrt{N_{\mathrm{pix}}}\Delta_{\mathrm{pix}} f_{\mathrm{L2}}}{2 f_{\mathrm{LL}} f_{\mathrm{tel}}}$$

The size of the pinhole must be chosen, so that the secondary mirror in the telescope is illuminated. Using the formula for circular aperture diffraction, and having the first minimum at the edge of the secondary mirror gives $D_{\mathrm{PH}} = 2.44 f_{\mathrm{tel}}\lambda/D_{\mathrm{tel}}$. The size of the pinhole also affects the radiance requirement for the light source. The radiant flux at the lenslet array is approximately

$$\Phi_{\mathrm{LA}} \approx 0.5^3 R_{\mathrm{tel}}^2 R_{\mathrm{DM}} \frac{A_{\mathrm{PH}}}{A_{\mathrm{LA}}} \Phi_{\mathrm{PH}}$$

where R is the reflectance and A the area of the indexed components and Φ_{PH} the radiant flux at the pinhole. The number of photons per pixel, during a sampling period τ, is approximately given by

$$N_{\mathrm{ppp}} = \Phi_{\mathrm{LA}} \tau \frac{\lambda}{hc} A_{\mathrm{LL}} \frac{1}{4}$$

where the term 1/4 originates from the choice of spot size on the CCD. We choose a signal to noise ratio of 100, thus N_{ppp} should be 10000 (Poisson noise considered to be the dominant noise source). The required radiant flux at the pinhole is approximately 0.03 W/m^2, which does not put any major constrains on the light source.

The data for the suggested experiment is gathered in Table 1.

3. DEFORMABLE MIRROR

An aluminium plate is used as a continuous faceplate mirror. Low-cost force actuators are attached to the back of the plate with suction cups in a Cartesian topology. Pressure sensors are placed between the actuators to ensure stability. The plate is fixed at three points, along the edge, forming a uniform triangle.

The illuminated part is a small fraction of the total area of the aluminium plate. There are two reasons for choosing a larger plate than what is strictly needed for the experiment. First, larger continuous faceplates places less constraints on the required actuator bandwidth. At sufficiently high frequencies, a single resonance or anti-resonance peak is no longer possible to discern[4]. This behavior occurs because many different modes overlap above a given frequency, thus there is no need for actuators to add damping. The second reason is, that a large plate is more representative of a large deformable mirror, giving the experiment more credibility.

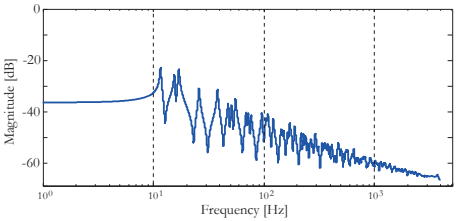

Figure 2. The transfer function of the aluminum plate at a representative position from force to position.

3.1 Control

Use of low-cost force actuators in combination with a thin plate leads to a lightly damped system with structural resonance frequencies within the desired control bandwidth. A control system for such a system has been developed and presented[4,6]. The control scheme relies on feedback signals from the pressure sensors.

Rate feedback adds significant damping, making the position control design more straightforward. This is guaranteed to be robustly stable, for an infinite bandwidth. However, the bandwidth of the rate control is limited by the finite bandwidth of the actuators and sensors. For a structure with non-zero damping, there will be a frequency, the "acoustic limit", at which the half-power bandwidth of the resonant mode will exceed the modal spacing by a sufficient factor[4]. The transfer function is relatively smooth in magnitude and phase above the acoustic limit, seen in Fig. 2 around 1 kHz. Thus, it is sufficient to add damping up to the acoustic limit, which makes use of the low-cost actuators and sensors possible.

The task of the position feedback is to add electronic stiffness. The plant (encompassing the actuators and the plate) is ill-conditioned, because the loop gain for low spatial frequencies is magnitudes higher than for high spatial frequencies. An actuator command gives a global response opposite to the intended local correction. The ill-conditioned plant is partially corrected with the position feedback and partially through a local control concept[6]. The gain of the proportional position feedback should be set such that the loop adds stiffness to the high-spatial frequencies and not the low-spatial frequencies.

The local control is defined in Fig. 3 as the **Q**-matrix, which converts a deflection command at a single location into a set of actuator commands. The static response of the plate to an actuator command is $\mathbf{x} = \mathbf{Cf}$, where $\mathbf{C}$ is a modified compliance matrix, in which all degrees of freedom except the out-of-plane translation have been removed. Define the state $\boldsymbol{\xi}$ to be a unit displacement at one actuator location, and we chose the actuator response pattern, which minimizes the cost function

$$J = \|\mathbf{Cf} - \boldsymbol{\xi}\| \tag{1}$$

subjected to the additional constraint that elements of $\mathbf{f}$ corresponding to nodes outside an "actuator family", near the command location must be zero. In other words, we chose a local set of forces to minimize the error over the entire mirror when matching a desired displacement vector. The computed force vectors for each actuator family are stored as columns in the family matrix $\mathbf{Q}$. The size of the actuator families is here chosen to be 21 actuators except at the edge. The layout of a family can be seen in Fig. 1, where the filled actuators represent one family.

4. SETUP OF MODEL

The architecture of the full model is shown in the block diagram of Fig. 4, further described in Sec. 4.1-4.3. The rate feedback loop uses a differentiator to generate a velocity signal. The adaptive optics loop is closed with an integrator controller. The three gains $\mathbf{K}_i$, $\mathbf{K}_p$, and $\mathbf{K}_v$ are all diagonal matrices, representing single-input-single-output feedback loops. The family matrix $\mathbf{Q}$ converts single displacement commands to sets of force commands.

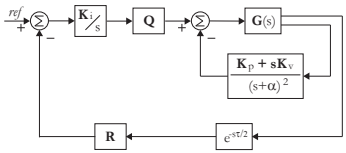

Figure 3. Block diagram of the control system. $\mathbf{G}(s)$ is the open-loop system of the plate. Rate feedback, $\mathbf{K}_\mathrm{v}$, adds damping and position feedback, $\mathbf{K}_\mathrm{p}$, adds stiffness, both are limited by actuator and sensor dynamics represented by the poles at $s = -\alpha$. The outer position control loop represents the adaptive optics feedback, it includes a delay block with a delay of $\tau/2$ where τ is the sampling frequency, a reconstructor, $\mathbf{R}$, an integrator gain, $\mathbf{K}_\mathrm{i}$, and the family matrix, $\mathbf{Q}$.

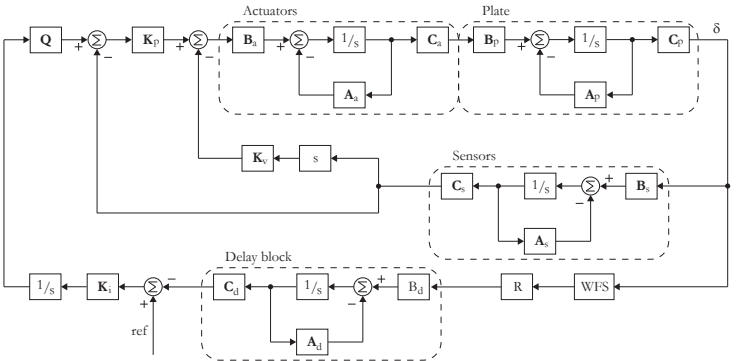

Figure 4. Block diagram of the integrated model.

4.1 Plate module

The structural model of the plate is built in MATLAB using a set of differential equations. The eigenvalues and eigenvectors of the structural modes are developed in the finite element analysis software tool Comsol Multiphysics, and are then imported into MATLAB.

The finite element model (FEM) has about 10200 nodes, each with six degrees of freedom. The two in-plane translations and the out-of-plane rotation of the rigid body are removed by static condensation, retaining piston, z, and the two in-plane rotations, ϕ and θ. Thus, the state vector for each node is described by $\mathbf{y}_i = [\phi_i \ \theta_i \ z_i]^T$, and the overall state vector is $\mathbf{x} = [\mathbf{y}_1 \ ... \ \mathbf{y}_N]^T$ satisfying

$$\mathbf{M}\ddot{\mathbf{x}} + \mathbf{D}\mathbf{E}\dot{\mathbf{x}} + \mathbf{K}\mathbf{x} = \mathbf{f} \tag{2}$$

The mass and stiffness matrices, $\mathbf{M}$ and $\mathbf{K}$ are given by the FEM, $\mathbf{E}$ is the damping matrix, and $\mathbf{f}$ is the force vector. The equation of motion, Eq. 2, can be rewritten as[7]

$$\ddot{\mathbf{q}} + 2\mathbf{Z}\mathbf{\Omega}\dot{\mathbf{q}} + \mathbf{\Omega}^2\mathbf{q} = \mathbf{\Psi}^T\mathbf{f} \tag{3}$$

where $\mathbf{\Psi}$ is the mass normalized eigenvector matrix, $\mathbf{\Omega}$ the diagonal matrix holding the eigenfrequencies and $\mathbf{Z}$

the modal damping (set to a modest 1% here). The state-space model is given by

$$\begin{aligned}
\mathbf{A}_\mathrm{p} &= \begin{bmatrix} -2\mathbf{Z\Omega} & -\mathbf{\Omega}^2 \\ \mathbf{I} & 0 \end{bmatrix} \qquad \mathbf{B}_\mathrm{p} = \begin{bmatrix} \mathbf{\Psi}^T \\ 0 \end{bmatrix} \\
\mathbf{C}_\mathrm{p} &= \begin{bmatrix} 0 & \mathbf{\Psi} \end{bmatrix} \qquad \mathbf{D}_\mathrm{p} = 0 \\
\mathbf{x} &= \begin{Bmatrix} \dot{\mathbf{q}} \\ \mathbf{q} \end{Bmatrix}
\end{aligned}$$

4.2 Actuator and sensor module

The mechanical behavior of the force actuators can be described by the equation of motion using the mass, m, of the moving rod, the stiffness, k, the damping, e, which are the coefficients of the suction cup (attaching the force actuators to the back of the plate), and the force coefficient of the voice coil. The natural frequency of the actuators is inside the bandwidth of the control system, potentially leading to stability problems. This is solved by an internal position loop with feedback from a linear variable differential transform (LVDT) to the voice coil that increases the natural frequency of the actuator. The natural frequency and the damping of the system with the internal feedback becomes

$$\begin{aligned}
\omega_\mathrm{a} &= \sqrt{\tfrac{gC+k}{m}} \\
\zeta_\mathrm{a} &= \tfrac{d}{2\sqrt{m(gC+k)}}
\end{aligned}$$

where g is the gain if the internal feedback loop and C is the force constant of the voice coil. The state-space realization of the actuators is given by

$$\begin{aligned}
\mathbf{A}_\mathrm{a} &= \begin{bmatrix} -2\zeta_\mathrm{a}\omega_\mathrm{a} & -\omega_\mathrm{a}^2 \\ 1 & 0 \end{bmatrix} \qquad \mathbf{B}_\mathrm{a} = \begin{bmatrix} \omega_\mathrm{a}^2 \\ 0 \end{bmatrix} \\
\mathbf{C}_\mathrm{a} &= \begin{bmatrix} 0 & 1 \end{bmatrix} \qquad \mathbf{D}_\mathrm{a} = 0 \\
\mathbf{x} &= \begin{Bmatrix} \dot{\delta} \\ \delta \end{Bmatrix}
\end{aligned}$$

where δ is the piston for the node corresponding to the actuator position.

The sensors on the back of the mirror have electret microphones inside bellows. Such a sensor can be viewed as a pressure sensor, having a flat region of the frequency response between the high-pass cutoff frequency, ω_hp, and the low-pass cutoff, ω_lp. The transfer function is given by

$$H_\mathrm{sen}(s) = \frac{s}{s+\omega_\mathrm{hp}} \cdot \frac{\omega_\mathrm{lp}}{s+\omega_\mathrm{lp}}$$

with the corresponding state space realization

$$\begin{aligned}
\mathbf{A}_\mathrm{s} &= \begin{bmatrix} 0 & -\omega_\mathrm{hp}\omega_\mathrm{lp} \\ 1 & -\omega_\mathrm{hp}-\omega_\mathrm{lp} \end{bmatrix} \qquad \mathbf{B}_\mathrm{s} = \begin{bmatrix} 0 \\ \omega_\mathrm{lp} \end{bmatrix} \\
\mathbf{C}_\mathrm{s} &= \begin{bmatrix} 0 & 1 \end{bmatrix} \qquad \mathbf{D}_\mathrm{s} = 0
\end{aligned}$$

The corner frequencies are 20 Hz and 5 kHz for our design.[5]

4.3 Adaptive optics module

The adaptive optics module encompasses a simple Shack-Hartmann wavefront sensor, a reconstructor, an integrator controller and a delay block.

The Shack-Hartmann wavefront sensor part is modeled by a matrix for computation of the tip and tilt over each subaperture. Each row of the matrix has four elements which are non-zero, computing either tip or tilt

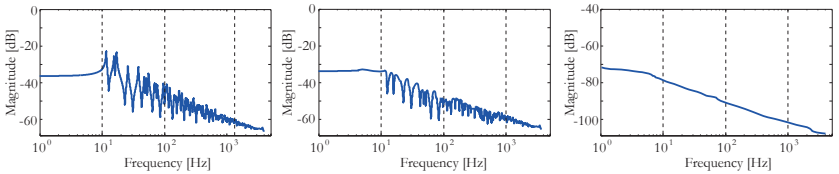

Figure 5. Bode diagrams from force to position at a representative actuator. The diagrams show the cases from left to right; the dynamic behavior of the faceplate, the dynamic behavior when the rate feedback for the representative actuator is closed, and the dynamic behavior when the rate feedback is closed for all actuators

from the piston value at the corners of the subaperture.[9] Aligning the lenslet array such that the corners of the grid coincide with the actuator locations, makes it possible to compute the tip and tilt from $\boldsymbol{\delta}$.

The reconstructor matrix for correction and is constructed by a singular value decomposition of the interaction matrix, i.e. the matrix which describes the tip and tilt of the subapertures when poking each actuator individually.

The performance of the adaptive optics loop is limited by the phase lag introduced by the delay block, representing the effects related to wavefront sampling, data acquisition and computation time. The delay is modeled as state-space model of a fifth order Padé approximation of $e^{-s\frac{\tau}{2}}$, where τ is the sampling period of the adaptive optics loop.

5. RESULTS

5.1 Effect of omitting actuators in laboratory experiment

The optical setup presented in Fig.1, has a faceplate which is only illuminated on about 13% of its total area. It is the same part which the wavefront sensor covers. A fully populated faceplate, with an actuator pitch of 50 mm and a Cartesian topology, would encompass 353 actuators. However, the illuminated part covers 45 actuator locations. Thus, the task is to create a concept where the 45 controlled actuators perceive their environment as if all actuators would be in operation.

The stiffness constant of each actuator is $5\,x\,10^5\,\mathrm{Nm}^{-1}$. The same stiffness can be achieved in a thin rod of aluminum glued to the back of the mirror. From simple solid mechanics, the diameter, d_r and length, l_r, of the rod are related by

$$k = E\frac{\pi d_\mathrm{r}^2}{4l_\mathrm{r}} \quad \Rightarrow \quad \frac{l_\mathrm{r}}{d_\mathrm{r}^2} \approx 10^5\,\mathrm{m}^{-1}$$

An aluminum rod, with the dimensions determined by the above equation, can be viewed as a zero-seeking actuator in our setup. However, the aluminum rod cannot mimic the rate feedback loop. The dynamical behavior of the rate feedback loop for a fully populated faceplate (353 actuators included) is seen in Fig. 5, where three Bode diagrams from force to position are shown for a representative actuator location. From left to right the diagrams show respectively, the dynamic behavior of the faceplate, the dynamic behavior when the rate feedback for the representative actuator is closed, and the dynamic behavior when the rate feedback is closed for all actuators. Closing one rate feedback loop, with the appropriate gain, adds damping to all the resonances but not the anti-resonances, which however are effectively suppressed when the rate feedback is closed for all the actuators.

An important feature, for our partially illuminated experiment, is the shift in magnitude between closing one and all rate feedback loops, seen in Fig. 5. That is, the gain needed to close one rate feedback loop sufficiently has a significant global over-damping of 40 dB. Thus, it should be sufficient to close the rate feedback for 45 actuators, as long as the anti-resonances are effectively damped.

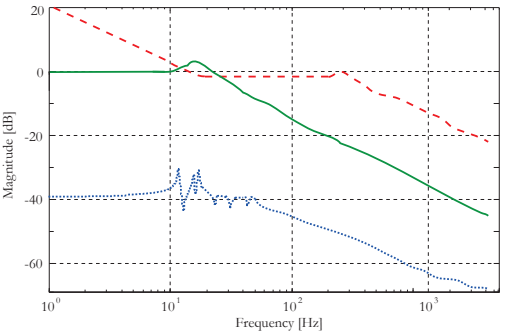

Figure 6. Transfer function from force to position for a representative actuator. The dotted curve represents the case when only the rate loop is closed. The dashed curve represents the case when the position loop is closed, including a family around the actuator. The full curve is for the case when the adaptive optics loop is closed.

5.2 Simulations with the setup model

The reasoning above is confirmed by simulations with the model described in Sec. 4. The active actuators of the faceplate are chosen to be centered on the part of the mirror that is illuminated. The remaining 308 actuator locations only have added stiffness from the metal rods. The average transfer function for the nine centered actuator families, from force to position of the center actuator, is shown in Fig. 6. The input command vector has all zeros except at the actuator location. The magnitude of the input at that location is then the scalar input, and the output is the displacement at the same location. The objective is to study high spatial frequency behavior. The dotted line represents the case where only the rate feedback loops are closed. The resonance and anti-resonance peaks at low frequencies are are seen because the sensors roll-off below 20 Hz. A couple of anti-resonance peaks can be distinguished above 20 Hz because there are not enough actuators to add sufficient damping. The peaks between 10-40 Hz are suppressed by the family matrix, since these eigenmodes are not excited by the actuators.[8]

The dashed curve in Fig. 6 represents the case when rate and position feedback loops are closed. Here, the family matrix is also included. The asymptote below 20 Hz is due to sensor roll-off. A small deviation between 0 dB and the curve is seen between 20 and 300 Hz. This behavior is explained by the fact that the back sensors are not collocated with the actuators. The maximum of an influence functions of an actuator is not fully detected by the sensors, instead about 60% of its displacement is measured. This is the dynamic behavior of the deformable mirror, i.e. the plant seen by the wavefront sensor loop.

The dynamic behavior of the adaptive optics system including the wavefront sensor, for the center actuators of the nine actuator families, is seen as the full line in Fig. 6. The bandwidth of the loop, starting to roll-off at 20 Hz, is limited by the sampling frequency of the wavefront sensor.

6. CONCLUSION

The experimental setup presented in Sec. 2 is highly useful, even though the components only allows for a partially illuminated large deformable mirror. The inexpensive actuator and sensor concept can be experimentally tested with the suggested control system. Further, the robustness of the deformable mirror concept can be studied.

The suggested number of active actuators, 45, allows nine full actuator families to be included. These families can be used to experimentally test the dynamic properties we have reported. The suppression of low-order eigenmodes through the use of actuator families is a key feature of our concept. Our simulation shows that this feature can be fully demonstrated with the laboratory experiment proposed. In fact, it is likely that the family principle is applicable also for other deformable mirror concepts. Local control, using a small number

of actuators to restrict global response to a local error, has proven to work also with another set of boundary conditions than reported before.

REFERENCES

[1] F. Wildi, G. Brusa, M. Lloyd-Hart, L. Close and A. Riccardi, "First light of the 6.5-m MMT adaptive optics system," Proc. SPIE **5169** (2003)

[2] F. Quiros-Pacheco, L. Busoni, G. Aqapito, S. Esposito, E. Pinna, A. Puqlisis and A. Riccardi, "First Light AO (FLAO) system for LBT: performance analysis and optimization," Proc. SPIE **7736** (2010)

[3] R. Arsenault, R. Biasi, D. Gallieni, A. Riccardi, P. Lazzarini, N. Hubin, E. Fedrigo, R. Donaldson, S. Oberti, S. Stroebele, R. Conzelmann and M. Duchateau, "A deformable secondary mirror for the VLT," Proc. SPIE **6272** (2004)

[4] D. MacMynowski, R. Heimsten and T. Andersen, "Distributed Force Control of Deformable Mirrors," European Journal of Control **17** (2011)

[5] T. Andersen, O. Garpinger, M. Owner-Petersen, F. Bjoorn, R. Svahn and A. Ardeberg, *Novel concept for large deformable mirrors* Optical Engineering **45** (2006)

[6] R. Heimsten, D. MacMynowski and T. Andersen "Feasibility Study of a Low-Cost, Large Deformable Mirror," Optics Express (2011)

[7] T. Andersen and A. Enmark *Integrated Modeling of Telescopes* Springer-Verlag New York Inc. (2011)

[8] R. Heimsten, M. Owner-Petersen, T. Ruppel, D.G. MacMynowski and T. Andersen, "Suppressing Low-Order Eigenmodes with Local Control for Deformable Mirrors," Optical Engineering, Accepted

[9] J. W. Hardy *Adaptive Optics for Astronomical Telescopes* **ISBN 0-19-509019-5** (1998)